Thesis presented to obtain the grade of

DOCTOR FROM ECOLE POLYTECHNIQUE

Speciality : Plasma Physics

by

Yannick Glinec

Propagation of an ultra-intense laser pulse in an under-dense plasma : production of quasi-monoenergetic electron beams and development of applications.

defended on September, 22nd 2006 in front of the following committee :

Mr. Patrick Mora	Chairman
Mr. Victor Malka	Thesis supervisor
Mr. Philippe Martin	Referee
Mr. Vladimir Tikhonchuk	Referee
Mme. Sylvie Jacquemot	
Mr. Henri Videau	

This document is a translation of the french version of the PhD thesis published at Ecole Polytechnique. This is an interactive document which should evolve in time. Depending on the improvements done to the document, the relevant figure in the version number will be modified : first digit increases for major modification, second digit for minor corrections (typesetting errors, layout, ...).

List of changes made to the document

Date	Version	List of modifications
2006-10-30		Beginning of translation
2006	1.0	Initial release, translation from the french version

Contents

Acknowledgments **9**

Introduction **11**

1 Theory and evolution of electron acceleration using laser-plasma interaction **15**
1.1 Propagation of an electromagnetic wave 15
1.1.1 Maxwell equations 15
1.1.2 Laser parameters 16
1.1.3 Gaussian beams 16
1.2 Plasma waves 18
1.2.1 Plasma parameters 18
1.2.2 Fluid equations 19
1.2.3 Unidimensional model of the acceleration of electrons in a plasma wave 19
1.3 Non-linear effects 23
1.3.1 Ponderomotive force 23
1.3.2 Laser self-focusing 24
1.3.3 Wave breaking 25
1.4 Acceleration mechanisms 26
1.4.1 Linear regime 27
1.4.2 Non-linear regime 28
1.5 Future of the laser-based acceleration 32
1.5.1 Extension of the bubble regime to higher energies, scaling laws . 32
1.5.2 Injection and linear acceleration 37
1.5.3 Alternative techniques 38

2 Quasi monoenergetic spectrum and optimization **41**
2.1 Description of the experiment 41
2.1.1 Characteristics of the laser in “salle jaune” at LOA 41
2.1.2 Experimental setup 42
2.2 Quasi monoenergetic spectra 44
2.2.1 Improvement of the quality of the electron beam 44
2.2.2 Experimental spectra 45
2.2.3 Comparison to 3D PIC simulations 46
2.2.4 Absolute calibration of the scintillating screen and discussion about the charge 48

2.3 “quasi monoenergetic” regime in a narrow range of parameters 51
2.3.1 Influence of the electron density 51
2.3.2 Influence of the pulse duration 52
2.3.3 Influence of laser energy 54
2.3.4 Influence of the aperture of the focusing optics 55
2.4 Stability 56
2.4.1 Beam pointing stability 57
2.4.2 Spectral stability 58

3 Structures of the electron beam and propagation of the laser 59
3.1 Oscillations in the spectrum 59
3.1.1 Experimental results 59
3.1.2 Propagation of an asymmetric laser pulse 62
3.2 Transition radiation 64
3.2.1 Angular and spatial distribution of the OTR 65
3.2.2 Experimental setup 69
3.2.3 Imaging diagnostic 69
3.2.4 Spectral analysis 72
3.2.5 Oscillations in the OTR spectrum 74
3.2.6 Measurements in the terahertz range 76
3.3 Laser pulse properties 79
3.3.1 Origin of temporal shortening 79
3.3.2 Laser spectrum broadening 80
3.3.3 Temporal shortening of the laser pulse 80
3.3.4 Transmitted laser intensity 85
3.3.5 Thomson scattering 86
3.3.6 Interferometry 88

4 Applications of laser-based electron beams 91
4.1 Application to radiography 91
4.1.1 High resolution radiography 92
4.1.2 Retrieval of the internal profile of the object 93
4.1.3 Estimation of the γ-ray source size 95
4.2 Application to radiotherapy 97
4.2.1 Simulation parameters 98
4.2.2 Direct irradiation 99
4.2.3 Converging electron beam 103
4.2.4 Discussion 104
4.3 Application to femtolysis 106
4.4 Application to the generation of X-ray radiation (betatron mechanism) . . 109

Conclusion and perspectives 113

A Betatron oscillation model 117
A.1 Analytical equations 117
A.2 Optimisation of parameters 119

B Description of the electron spectrometer **121**
B.1 Experimental setup 121
B.2 Analytic trajectory 122
B.2.1 For a rectangular magnet 122
B.2.2 For a circular magnet 123
B.2.3 Adjustment to the magnetic field measured experimentally 123
B.2.4 Dispersion power 124
B.3 Development of new spectrometers 127

C Determination of the amplitude of the electron spectrum **129**
C.1 Simulation of the energy deposition in the scintillator 129
C.2 Calibration of the scintillator at Elyse 131
C.3 Absolute calibration 134
C.3.1 Conversion in photons in the scintillator 134
C.3.2 Collection by optics 134
C.3.3 Yield of the camera 134
C.4 Use of an integrating current transformer 135

Acknowledgments

I've spend three exciting years at Laboratoire d'Optique Appliquée in Palaiseau. This laboratory belongs to three different administrations : ENSTA, École Polytechnique and CNRS (UMR 7639). I would like to thank first my PhD supervisor, Victor Malka, visionary and realistic leader, hyperactive but still always available for his students. I remember having chosen this PhD subject after an interview at the laboratory in 2003. At that time, when most student wanted to start working in the field of cold atoms, i.e. the study of Bose-Einstein condensates, plasma physics was suffering of a lack of clarity. The list of instabilities and the restricted applicability of analytical equations to perturbative assumptions where responsible for my limited understanding of this physics. On the opposite, the understanding of the physics of condensates obtained at very low temperature was provocative and attractive. Nevertheless, comments from Victor convinced me : the use of an ultra-short laser pulse limited the instability growth and allowed a better energy transfer to kinetic energy of accelerated electrons. The world record of the electron energy was thus obtained in this research group with laser-plasma interaction during the pioneer work carried out during Sven Fritzler's PhD thesis.

At the time, Jerome Faure also became a permanent researcher in this group. During these three years, we have worked together in many experiments during which Jerome taught me everything with a lot of care and patience. I've personally really enjoyed the relevance of his thoughts and his temper. Thanks to him, I couldn't have wished a better formation than the one I was given.

The group "Particle Sources by Laser", in which I've been working, contains two research themes : electron acceleration and proton acceleration by laser. This second half of the group, working on the generation of a proton source, is composed of Alain Guemnie Tafo, Mauro Manclossi, Frederike Ewald and Joao Jorge Santos. Recently, Agustin Lifschitz has joined the team for a theoretical and simulation support. I would like to thank the whole team for their kind attention to me.

I would like also to point at the impressive work of the laser team working in the laser room ("Salle Jaune") : Jean-Philippe Rousseau, Frédéric Burgy, Brigitte Mercier and more recently Amar Tafzi who has just joined this team. I would like to underline their exceptional availability and their patience in front of an aggressive team of never-satisfied-experimentalists.

I also remember the support from Danièle Hulin during my initial application in the laboratory. And I would like also to thank Olivier Albert for his gentleness and his pedagogy during my training course in the laboratory as a future engineer because, following this training course, I've decided to continue with a PhD thesis. I would like to thank the administration of the laboratory, the director of which is currently Gérard Mourou, the work of the secretaries, the technical staff (the workshop, the maintenance, the multimedia

staff ...) and more generally all the teams working in the laboratory.

But outside the daily work in the lab, the unconditional support of my relatives from Britanny, from Paris and my family are essential support to fulfill these three years of studies. The biggest thank goes for Lina who remained incredibly calm and stoic even when I was bad-tempered.

Finally, I also remember all the collaborators I've been working with :

- The team from CEA DAM Île-de-France : Erik Lefebvre, Loic Le Dain, Stéphane Darbon, Bénédicte Guilpart.
- The team from Imperial College working at the Rutherford Appleton Laboratory : I quote in particular Stuart Mangles and Alec Thomas from this team, who I had the opportunity to meet several times.
- Alexander Pukhov from the Virtual Laser Plasma Laboratory (VLPL) in Germany.
- The laser and plasma group (GoLP) in Portugal : Luis O. Silva and Jorge Vieira.
- The German group from DKFZ : Hanitra Szymanowski, Thomas Fuchs and Uwe Oelfke.
- The laboratory Solides Irradiés at École Polytechnique : Stéphane Esnouf and Guillaume Petite.
- Guilhem Gallot from laboratory Optique et Biosciences at École Polytechnique.
- The team at Élyse in Orsay : Mehran Mostafavi, Vincent de Waele, Hugues Monard and J.P. Larbre.

Thank you for you help, your advice and all the good time spent together.

Finally, I would like to thank the thesis committee : Patrick Mora (chairman), Sylvie Jacquemot, Henri Videau, Victor Malka and my two referees : Vladimir Tickhonchuk and Philippe Martin. Their advice and their support helped to finalize this thesis.

In summary, I've been very happy to work in such good conditions, on a very exciting scientific field.

Introduction

Context

People know laser mainly through their daily applications. They can be found in compact-disc players, in the supermarket when reading the bar code or even during fireworks show. More specifically, they can be found in the industry to cut or weld metals or in hospitals for eye surgery. In the research field, the LASER tool (acronym for Light Amplification by the Stimulated Emission of Radiation) is used in a variety of configurations in many scientific fields. In plasma physics, this tool is used to generate very intense and ultra-short laser pulses in order to study the behaviour of ionized media.

Electron acceleration using laser-plasma interaction is a field of research, the rocketing evolution of which testifies the control of powerful laser systems and a better understanding of the underlying physical processes involved in this interaction. This discipline belongs to the study of laser-mater interaction. Ultra-short powerful laser systems have been used in the development of fields such as the harmonic generation, the production of hard X-rays, particle sources, ... These studies have lead to many applications in trans-disciplinary fields : analysis of materials, development of X-UV lasers, surface treatment, chemistry and biology are some examples.

Conventional accelerators allow the generation of electron beams with controlled and excellent properties. However, the accelerating electric field in radio-frequency structures is limited to value of the order of 50 MV/m (i.e. 5×10^7 V/m), in order to avoid the breaking of the wall of the accelerating structure. Consequently, in order to reach higher energy for particle physics, scientists have built always larger infrastructures. The former electron accelerator at CERN (LEP) allowed the production of 50 GeV electrons collected in a huge storage ring of 27 km in circumference. The size of the building (which also determines the cost) has become a real limit. Moreover, this accelerating technique is not adapted for industrial of medical applications. For instance, the obstruction of such accelerators in a treatment room limits the final energy to 20 MeV, which is misfit for the treatment of tumours located deeper than 10 cm.

The appearance of new accelerating techniques to produce high energy electrons arouses an important interest.The accelerating electric field in a plasma wave is now of the order of TV/m (i.e. 10^{12} V/m), which allows a significant shrinking of the accelerating distance. Plasmas are ionised media which can sustain very high electric fields, contrary to standard cavities which are limited by the ionisation of the walls. This technique uses the very high electric field generated by a plasma wave. There exist two methods to drive the plasma wave : either using an electron beam emerging from a conventional accelerator, or using very intense laser pulses. The first technique, which allowed the observation of energy

gains of 2.7 GeV for electrons from SLAC initially at 30 GeV, in only 10 cm of plasma (Hogan et al., 2005), won't be discussed in this document.

These promising results obtained on the electron energy during the acceleration in plasma waves should not hide the difficulties faced in such media. Currently, even if the properties of the electron beam are excellent according to many criteria (energy, charge, divergence, duration), the control of such properties is still limited. This introduces the work done during my PhD, aiming at a better understanding of the physical mechanisms involved and at the development of adapted applications.

Goals of the thesis

This thesis is an experimental study of the electron acceleration to high energy using intense laser pulses. Experiments presented here have been performed at Laboratoire d'Optique Appliquée in Palaiseau. The title of the PhD dissertation "Production of quasi-monoenergetic electron beam and development of applications" suggests two guidelines : on the one hand the improvement of the properties of the electron beam and on the other hand the study of applications which emphasize these properties. The general structure of the document follows these two axes.

Outline

The first chapter contains a general description of the accelerations mechanisms in laser-plasma electron acceleration. These techniques have evolved with the laser technology. The generation of shorter laser pulses lead to always higher electron energies.

The experimental results are distributed in chapters 2 and 3. The first one describes the characterization of the electron beam properties and shows unique properties : a quasi-monoenergetic spectrum, a high charge and a low divergence; These exceptional properties have been observed in a restricted range of parameters, the influence of which is presented in detail. Numerical simulations are carried out to help the understanding of the acceleration scenario and statistics of the electron beam are described.

The following chapter describes the observation of fine structures in the electron beam : (i) some electron spectra show oscillations. These are attributed to betatron oscillations, for which an analytical model is described taking into account the longitudinal acceleration. (ii) The measurement of the transition radiation in the visible range confirms that the electron beam has some structures at the laser frequency, that disappears with propagation distance. This is reproduced in simulations detailed in this document. Using the same technique closer to the electron source, spectral interferences have been recorded in the OTR signal, which can be explained by successive electron bunches passing through the interface. This measurement gives access to the delay between electron bunches at the interface. (iii) The measurement in the THz domain confirms that this electron beam has structures shorter than 100 fs. In the same chapter, I also show the properties of the laser : the laser pulse duration, measured with a single-shot autocorrelator, is shortened during the interaction. The transmitted laser energy and the energy dumped into the plasma waves can be estimated using an imaging diagnostic. The Thomson scattering diagnostic is used to visualize the laser propagation where the scattering is

important and an interferometry diagnostic gives the free electron density in the plasma.

The last chapter gathers all applications of the electron beam developed in the laboratory during this thesis. These applications have been selected to emphasize the unique properties of this electron source. I show the results of a γ-ray radiography experiment, some simulations of the dose deposited for radiotherapy treatment, but also the experimental study of water radiolysis in femto-chemistry and the generation of hard X-rays. The radiography shows that the γ-ray source size is smaller than the one obtained with equivalent conventional accelerators. Simulations for radiotherapy show the competitive properties of electron beams in terms of dose deposition, penetration depth and transverse penumbra. Water radiolysis emphasizes the brevity of the electron bunch in order to probe short-lived events. Finally, the generation of intense X-rays requires all the good properties of this electron beam.

This dissertation is followed by three appendices : the analytical method which describes betatron oscillations of electrons in an ionic channel including simultaneous acceleration, the detailed description of the electron spectrometer which has been used to design new spectrometers for future experiments and finally the absolute calibration of the electron spectrometer, which allows to avoid the use of an integrating current transformer.

Chapter 1

Theory and evolution of electron acceleration using laser-plasma interaction

Laser-plasma-based electron acceleration starts in 1979 when plasma waves are proposed to accelerate particles (Tajima and Dawson, 1979). Since this moment, fast and important improvement have been achieved, giving birth to several acceleration mechanisms. This evolution is reproduced in this chapter. First, the physical quantities used in the following are introduced and the example of acceleration in a linear 1D case is presented. This is followed by the list of some non-linear phenomena which are used to describe the history of laser-based electron acceleration. Finally, in order to reach even higher energies, the last models of acceleration are presented.

First, the next two ssections introduce the equations and physical quantities used to describe the interaction. These formulas are given is the international unit system (SI).

1.1 Propagation of an electromagnetic wave

1.1.1 Maxwell equations

An electromagnetic wave is a vibration that propagates in space and which contains both an electric and a magnetic component. A laser pulse is an electromagnetic wave. The propagation of an electromagnetic wave in a medium is described by the Maxwell equations :

$$\begin{cases} \vec{\nabla}.\vec{E} = \dfrac{\rho}{\varepsilon_0} & \vec{\nabla}.\vec{B} = 0 \\ \vec{\nabla}\wedge\vec{E} = -\dfrac{\partial\vec{B}}{\partial t} & \vec{\nabla}\wedge\vec{B} = \dfrac{1}{c^2}\dfrac{\partial\vec{E}}{\partial t} + \mu_0\vec{j} \end{cases} \tag{1.1}$$

where $\vec{E}$ and $\vec{B}$ are the electric and magnetic fields respectively, ρ and $\vec{j}$ describe the medium and are the local density and the current density respectively. ε_0 and μ_0 are the permittivity and permeability of vacuum. c is the celerity of light. The operator $\vec{\nabla}$ corresponds to the spatial partial derivative vector

$$\vec{\nabla} = \left(\frac{\partial}{\partial x}, \frac{\partial}{\partial y}, \frac{\partial}{\partial z}\right) \tag{1.2}$$

From this set of equations, one obtains the equation of propagation of the electric field. In vacuum ($\rho = 0$ and $\vec{j} = \vec{0}$), this is written :

$$\nabla^2 \vec{E}(\vec{x},t) - \frac{1}{c^2}\frac{\partial^2 \vec{E}}{\partial t^2}(\vec{x},t) = \vec{0} \tag{1.3}$$

In the frequency domain (for the temporal variable), it becomes :

$$\nabla^2 \vec{E}(\vec{x},\omega) + \frac{\omega^2}{c^2}\vec{E}(\vec{x},\omega) = \vec{0} \tag{1.4}$$

In a more general case of a propagation in an isotropic medium, one introduces the refractive index η in the equation of propagation, which contains the response of the medium

$$\nabla^2 \vec{E}(\vec{x},\omega) + \frac{\omega^2}{c^2}\eta^2(\omega)\vec{E}(\vec{x},\omega) = \vec{0} \tag{1.5}$$

1.1.2 Laser parameters

In general, one uses potentials to describe these fields. There exist a vector potential $\vec{A}$ and a scalar potential Φ that verify :

$$\begin{cases} \vec{E} = -\vec{\nabla}\Phi - \dfrac{\partial \vec{A}}{\partial t} \\ \\ \vec{B} = \vec{\nabla} \wedge \vec{A} \end{cases} \tag{1.6}$$

These potentials are not described uniquely. It is possible to find other solutions with a gauge transformation. We usually work in Coulomb gauge $\vec{\nabla}.\vec{A} = 0$.

In the following, we will use the normalized vector potential $\vec{a}$, defined by :

$$\vec{a} = \frac{e\vec{A}}{m_e c} \tag{1.7}$$

where e is the electron charge and m_e its mass.

One also introduces the intensity I (which is in fact an illumination), which is the average of the Poynting vector over an optical cycle :

$$I = c^2 \varepsilon_0 \left\langle \vec{E} \wedge \vec{B} \right\rangle_t \tag{1.8}$$

where brackets design the temporal average on one optical cycle.

1.1.3 Gaussian beams

Short laser pulses delivered by laser systems have a broad spectrum which contains many modes locked in phase. This spectrum is usually described simply by a gaussian envelope, thus also leading to an gaussian temporal envelope, which is close to reality. In the same way, the spatial profile of the laser pulse at the focal plane is also represented by a gaussian function. The electric field has the following form for a linearly polarized pulse :

$$\vec{E}(r,z,t) = \frac{E}{2} f(r,z) g(t,z) \exp\left[-i(k_0 z - \omega_0 t)\right] \vec{e_x} + \vec{cc} \tag{1.9}$$

Equation 1.9 contains a carrying envelope with wave number k_0 and frequency ω_0 and spatial and temporal information contained in $f(r,z)$ and $g(t)$ respectively. The following gaussian expressions (Eq. 1.10) verify the equation of propagation of the electric field in vacuum in the paraxial approximation. These expressions reproduce accurately the electric field of the laser when the focusing optics have small aperture.

$$\begin{aligned} g(t,z) &= \exp\left[-2\ln 2\,\left(\frac{t-z/c}{\tau_0}\right)^2\right] \\ f(r,z) &= \frac{\mathrm{w}_0}{\mathrm{w}(z)}\exp\left[-\frac{r^2}{\mathrm{w}^2(z)} - i\frac{k_0 r^2}{2R(z)}\right]\exp i\phi(z) \end{aligned} \tag{1.10}$$

where τ_0 is the pulse duration at full width at half maximum (FWHM), w_0 is the waist of the focal spot (the radius at $1/e$ of the electric field in the focal plane $z=0$). $\phi(z)$ is the Gouy phase. Functions $\mathrm{w}(z)$ and $R(z)$ represent respectively the radius at $1/e$ of the electric field and the radius of curvature of the wave front. These functions take the following form :

$$\mathrm{w}(z) = \mathrm{w}_0\sqrt{1+\frac{z^2}{Z_r^2}} \tag{1.11}$$

$$R(z) = z\left(1+\frac{Z_r^2}{z^2}\right) \tag{1.12}$$

$Z_r = \pi \mathrm{w}_0^2/\lambda_0$ is the Rayleigh length. This physical parameter represents the length where the laser intensity on axis has dropped by a factor 2 compared to the intensity in the focal plane ($z=0$).

Starting from this expression of the electric field, the following relation exists between the maximal intensity I_0 and the power P :

$$I_0 = \frac{2P}{\pi \mathrm{w}_0^2} \tag{1.13}$$

with $P = 2\sqrt{\dfrac{\ln 2}{\pi}}\,\dfrac{U}{\tau_0} \sim \dfrac{U}{\tau_0}$, where U is the energy contained in the pulse.

Then, the following relation lies the maximal intensity I_0 and the maximum of the normalized vector potential a_0

$$a_0 = \left(\frac{e^2}{2\pi^2\varepsilon_0 m_e^2 c^5}\lambda_0^2 I_0\right)^{1/2} \tag{1.14}$$

The physical quantities will be usefull in the following to describe the experiments done.

Numerical application

The laser at Laboratoire d'Optique Appliquée delivers an energy of $U = 1$ J on target in $\tau_0 = 30$ fs, which corresponds to an effective power of $P = 33$ TW. The wavelength λ_0 is 820 nm. An off-axis parabolic mirror with focal length $f = 1$ m focuses the beam down to the diffraction limit $\mathrm{w}_0 \sim \alpha\lambda_0 f/d = 18$ μm, where $d = 55$ mm is the diameter of the beam before focusing. For an homogeneous circular beam in

near field, the constant α equals 1.22. One estimates around 50% of the energy is contained in the focal spot. One deduces a maximal intensity $I_0 = 3 \times 10^{18}$ W/cm^2, which leads to $a_0 = 1.3$.

When a_0 exceeds unity, the oscillations of an electron in the laser field become relativistic. In our experimental conditions, the motion of the electrons is relativistic.

1.2 Plasma waves

A plasma is a state of matter made of free electrons, totally or partially ionized ions and neutral molecules, the whole medium being globally neutral (as many positive as negative charges). Plasmas are present in our daily life (plasma screens, plasma lamps for instance). More generally, they form a large part of the universe : interstellar plasmas, stars (such as our sun), ...

1.2.1 Plasma parameters

Let's assume an initially uniform, non-collisional plasma in which a slab of electron is displaced from the equilibrium position. The restoring force which applies on this electron slab, drives them towards the equilibrium position. For the time scale corresponding to the electron motion, one neglects the motion of the ions because of the inertia. This gives in the end oscillations around the equilibrium position at a frequency called the electron plasma frequency ω_{pe}

$$\omega_{pe} = \sqrt{\frac{n_e e^2}{m_e \varepsilon_0}} \tag{1.15}$$

where n_e is the unperturbed electron density.

This frequency has to be compared to the laser frequency : if $\omega_{pe} < \omega_0$ then the characteristic time scale of the plasma is longer than the optical period of the incoming radiation. The medium can't stop the propagation of the electromagnetic wave. The medium is said to be transparent or under-dense. On the opposite, when $\omega_{pe} > \omega_0$ then the characteristic time scale of the electrons is fast enough to adapt to the incoming wave and to reflect totally of partially the radiation. The medium is said to be overdense.

These two domains are separated at frequency ω_0, which corresponds to the critical density $n_c = \omega_0^2 m_e \varepsilon_0 / e^2$.

Numerical application
For an wavelength $\lambda_0 = 820$ nm, one obtains $n_c = 1.7 \times 10^{21}$ cm^{-3}. in our experimental conditions with gas jets, the electrons density ranges in $n_e \in [10^{17}; 10^{20}]$ cm^{-3}. We work in an underdense plasma and the laser pulse propagates.

In the 3D case, if one assumes that plasmas are perfect gases, an homogeneous plasma has an electron velocity distribution $f_e(v_e)$ which obeys the Maxwell-Boltzmann relation at thermodynamic equilibrium.:

$$f_e(v_e) = n_e \left(\frac{m_e}{2\pi k_B T_e} \right)^{3/2} \exp\left(-\frac{1}{2} \frac{m_e v_e^2}{k_B T_e} \right) \tag{1.16}$$

where k_B is the Boltzmann's constant, T_e is the temperature of the electron gas. The average thermal velocity of the electrons for this distribution is $v_{te} = \sqrt{k_B T_e / m_e}$

1.2.2 Fluid equations

Let $f_e(\vec{x},\vec{v},t)$ be the distribution function of the electrons in the phase space. This means that the number of electrons between positions $\vec{x}$ and $\vec{x}+d\vec{x}$ with a speed between $\vec{v}$ and $\vec{v}+d\vec{v}$ at time t is given by $f_e(\vec{x},\vec{v},t)\|d\vec{x}\|\,\|d\vec{v}\|$. The Vlasov equation describes the evolution of the distribution function in the electric $\vec{E}$ and magnetic $\vec{B}$ field of the wave in the non-collisional regime :

$$\frac{\partial f_e}{\partial t} + \vec{v}.\vec{\nabla} f_e - \frac{e}{m_e}\left(\vec{E} + \vec{v}\wedge\vec{B}\right).\frac{\partial f_e}{\partial \vec{v}} = 0 \tag{1.17}$$

In general, we use more explicit expressions of the Vlasov equation. These are fluid equations obtained from the momenta of Eq. 1.17 by integrating over velocities ($\int d^3\vec{v}$), and assuming the the local field equals the average field.

$$\begin{cases} \dfrac{\partial n_e}{\partial t} + \vec{\nabla}.(n_e\vec{v_e}) = 0 \\ \dfrac{\partial \vec{v_e}}{\partial t} + (\vec{v_e}.\vec{\nabla})\vec{v_e} = -\dfrac{e}{m_e}\left(\vec{E} + \vec{v_e}\wedge\vec{B}\right) - \dfrac{1}{n_e m_e}\vec{\nabla}.\overrightarrow{P_e} \end{cases} \tag{1.18}$$

The macroscopic quantities are

- the density $n_e(\vec{x},t) = \int f_e(\vec{x},\vec{v},t)\, d^3\vec{v}$
- the velocity $\vec{v_e}(\vec{x},t) = \dfrac{1}{n_e(\vec{x},t)}\int f_e(\vec{x},\vec{v},t)\,\vec{v}\, d^3\vec{v}$
- the pressure $\overrightarrow{P_e}(\vec{x},t) = m_e \int f_e(\vec{x},\vec{v},t)\,(\vec{v}-\vec{v_e})(\vec{v}-\vec{v_e})^t\, d^3\vec{v}.$

where $\vec{v}^t$ represents the transposed of vector $\vec{v}$.

These two equations 1.18 represent respectively the conservation of mass and the equation of motion. They describe the response of the plasma to an electromagnetic wave.

1.2.3 Unidimensional model of the acceleration of electrons in a plasma wave

One studies here the theory of trapping of electrons in a unidimensional relativistic plasma wave (Mora and Amiranoff, 1989). I detail the calculations because I think relevant to understand the acceleration mechanism in a simplified case.

Electric field of the plasma wave

One considers now a periodic sinusoidal perturbation of the electron plasma density in a uniform ion layer. Mechanisms responsible for the excitation of the plasma wave will be described in the following section. The density perturbation δn is written :

$$\delta n = \delta n_e \sin(k_p z - \omega_p t) \tag{1.19}$$

where ω_p and k_p are the angular frequency and the wave number of the plasma wave.

This density perturbation leads to a perturbation of the electric field $\delta\vec{E}$ via the Poisson equation 1.1

$$\vec{\nabla}.\delta\vec{E} = -\frac{\delta n\, e}{\varepsilon_0} \tag{1.20}$$

This gives

$$\delta\vec{E}(z,t) = \frac{\delta n_e\, e}{k_p \varepsilon_0}\cos(k_p z - \omega_p t)\vec{e}_z \tag{1.21}$$

Because we want to describe the electron acceleration to relativistic energies by a plasma wave, we consider now a plasma wave with a phase velocity is close to the speed of light $v_p = \omega_p/k_p \sim c$. Let $E_0 = m_e c\omega_{pe}/e$. The electric field becomes :

$$\delta\vec{E}(z,t) = E_0\frac{\delta n_e}{n_e}\cos(k_p z - \omega_p t)\vec{e}_z \tag{1.22}$$

One notice that the electric field is dephased by $-\pi/4$ with respect to the electron density.

Lorentz's transform

Let's now describe what happens to an electron placed in this electric field. The goal is to obtain the required conditions for trapping to occur. The following variables are introduced to describe the electron in the laboratory frame : z the position, t the associated time, β the velocity normalized to c, $\gamma = 1/\sqrt{1-\beta^2}$ the associated Lorentz's factor. In the frame of the plasma wave, let z', t' ,β' and γ' represent the equivalent quantities.

The frame linked to the plasma wave is in uniform constant translation at speed $v_p = \beta_p c$. One writes γ_p the Lorentz's factor associated to this velocity. The Lorentz's transform allows to switch from the laboratory frame to the wave frame :

$$\begin{cases} z' = \gamma_p(z - v_p t) \\ t' = \gamma_p(t - \dfrac{v_p}{c}x) \\ \gamma' = \gamma\gamma_p(1 - \vec{\beta}.\vec{\beta}_p) \end{cases} \tag{1.23}$$

In this new frame, without magnetic field, the electric field remains unchanged $\delta\vec{E}'$

$$\delta\vec{E}'(z') = \delta\vec{E}(z,t) = E_0\frac{\delta n_e}{n_e}\cos(k_p z'/\gamma_p)\vec{e}_z \tag{1.24}$$

Consequently, in terms of potential, the electric field is derived from potential Φ' defined by

$$\vec{F} = -e\delta\vec{E}' \equiv -\vec{\nabla}'\Phi' \tag{1.25}$$

This leads to

$$\Phi'(z') = mc^2\gamma_p\frac{\delta n_e}{n_e}\sin(k_p z'/\gamma_p) \equiv mc^2\phi'(z') \tag{1.26}$$

Finally, one writes the total energy conservation for the particle in this frame compared to the initial energy at the injection time (labelled with subscript 0) :

$$\gamma'(z') + \phi'(z') = \gamma'_0(z'_0) + \phi'_0(z'_0) \tag{1.27}$$

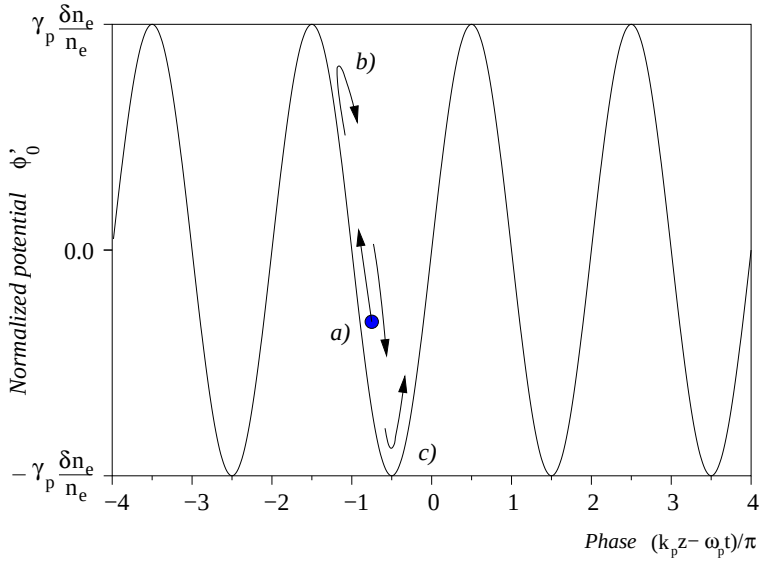

Figure 1.1: Trajectory of an electron injected in the potential of the plasma wave in the frame of the wave. The letters correspond to the instant when : a) the electron is injected in the wave, b) the electron travels at the speed of the plasma wave, c) the electron has the maximal velocity and enters the decelerating part of the wave.

Equation 1.27 gives the relation between the electron energy and its position in the plasma wave. Figure 1.1 illustrates the motion of an electron injected in this potential. Finally, we perform the reverse Lorentz's transform to give this energy in the laboratory frame.

For $\beta' > 0$, the scalar product in eq. 1.23 is positive

$$\gamma = \gamma'\gamma_p + \sqrt{\gamma'^2 - 1}\sqrt{\gamma_p^2 - 1} \tag{1.28}$$

For $\beta' < 0$, scalar product in eq.. 1.23 is negative

$$\gamma = \gamma'\gamma_p - \sqrt{\gamma'^2 - 1}\sqrt{\gamma_p^2 - 1} \tag{1.29}$$

Electron trajectories

Figure 1.2 represents an example of electron trajectory in a plasma wave. In this phase space, the closed orbits correspond to trapped particles. Open orbits represent untrapped

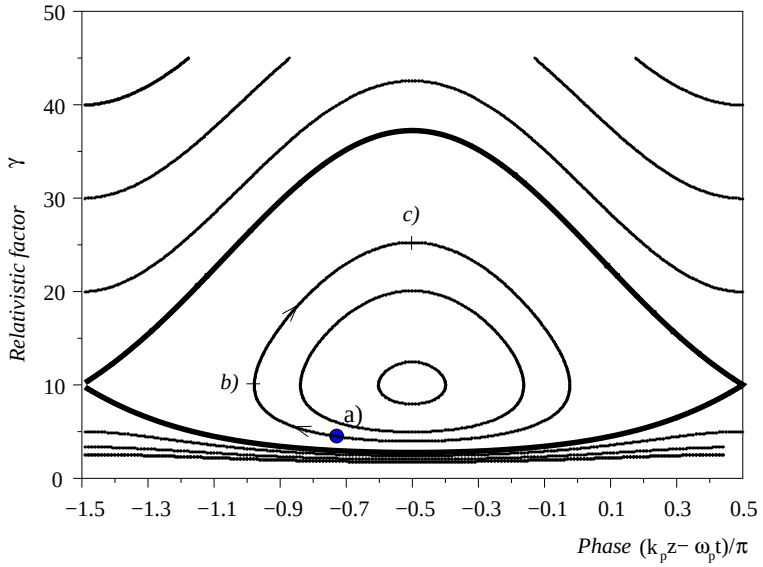

Figure 1.2: Electron trajectory in a plasma wave in the phase space $(k_p z - \omega_p t, \gamma)$ for $\gamma_p = 10$ and $\delta n_e/n_e = 0.05$. The thick line represents the separatrix. Closed orbits are trapped trajectories and open orbits are untrapped trajectories. The letters match the instants defined in caption of Fig. 1.1.

electrons, either because the initial velocity is too low, or to high. The curve which separates these two regions is called the separatrix.

This separatrix gives the minimum and maximum energies for trapped particles. This is comparable to the hydrodynamic case, where a surfer has to crawl to gain velocity and to catch the wave. In terms of relativistic factor, γ has to belong to the interval $[\gamma_{min}; \gamma_{max}]$ with :

$$\begin{cases} \gamma_{min} = \gamma_p(1+2\gamma_p\delta) - \sqrt{\gamma_p^2-1}\sqrt{(1+2\gamma_p\delta)^2-1} \\ \gamma_{max} = \gamma_p(1+2\gamma_p\delta) + \sqrt{\gamma_p^2-1}\sqrt{(1+2\gamma_p\delta)^2-1} \end{cases} \tag{1.30}$$

where $\delta = \delta n_e/n_e$ is the relative amplitude of the density perturbation.

One deduces that the maximum energy gain ΔW_{max} for a trapped particle is reached for a closed orbit with maximum amplitude. This corresponds to the injection at γ_{min} on the separatrix and its extraction at γ_{max}. The maximum energy gain is then written

$$\Delta W_{max} = (\gamma_{max} - \gamma_{min})mc^2 \tag{1.31}$$

For an electron density much lower than the critical density $n_e \ll n_c$, one has $\gamma_p = \omega_0/\omega_p \gg 1$ and

$$\Delta W_{max} = 4\gamma_p^2 \frac{\delta n_e}{n_e} mc^2 \tag{1.32}$$

For electron travelling along the separatrix, the time necessary to reach maximal energy is infinite because there exist a stationnary point at energy γ_p. On other closed orbits, the electron successively gains and looses energy during its rotation of the phase space. In order to design an experiment, one needs an estimation of the distance an electron travels before reaching maximal energy gain. This length, which is called the dephasing length

L_{deph}, corresponds to a phase rotation of $\lambda_p/2$ in the phase space. In order to have a simple analytical estimation, one needs to assume that the energy gain is small compared to the initial energy of the particle and that the plasma wave is relativistic $\gamma_p \gg 1$, then the dephasing length is written

$$L_{deph} \sim \gamma_p^2 \lambda_p \tag{1.33}$$

This concept of dephasing length in a 1D case can be refined in a bi-dimensional case. Indeed, if one also takes into account the transverse effects of the plasma wave, this one is focusing or defocusing for the electrons along their acceleration (Mora, 1992). Because these transverse effects are shifted by $\lambda_p/4$ with respect to the pair acceleration/deceleration, the distance over which the plasma wave is both focusing and accelerating is restricted to a rotation of $\lambda_p/4$ in phase space, which decreases by a factor 2 the dephasing length from eq. 1.33.

$$L_{deph}^{\mathrm{2D}} \sim \gamma_p^2 \lambda_p/2 \tag{1.34}$$

In these formulas, one has considered a unique test electron, which has no influence on the plasma wave. In reality, the massive trapping of particles modifies electric fields and distorts the plasma wave. This is called space-charge effect (Coulomb repulsion force). Finally, this linear theory is difficult to apply to highly non-linear regimes which are explored experimentally. Some non-linear effects concerning short pulses are described in the next section. Nonetheless, these formulas are usefull to scale the experiments.

1.3 Non-linear effects

1.3.1 Ponderomotive force

Let's take a non-relativistic electron for a short while. In a laser field with a weak intensity, the average position of an electron is constant. If one only keeps linear terms in fluid equation 1.18, there remains (Kruer, 1988):

$$\frac{\partial \vec{v_e}^{(l)}}{\partial t} = -\frac{e}{m_e}\vec{E} \tag{1.35}$$

The electron directly varies with the electric field. Let's consider now a laser pulse slightly more intense, so that the electron velocity becomes slightly non linear $\vec{v_e} = \vec{v_e}^{(l)} + \vec{v_e}^{(nl)}$ with $\|\vec{v_e}^{(nl)}\| \ll \|\vec{v_e}^{(l)}\|$. The second order terms satisfy the following equation

$$\frac{\partial \vec{v_e}^{(nl)}}{\partial t} = -(\vec{v_e}^{(l)}.\vec{\nabla})\vec{v_e}^{(l)} - \frac{e}{m_e}(\vec{v_e}^{(l)} \wedge \vec{B}) \tag{1.36}$$

By keeping the low frequency component of the equation of motion, i.e. by averaging over an optical cycle, one obtains

$$m_e \frac{\partial \left\langle \vec{v_e}^{(nl)} \right\rangle_t}{\partial t} = -\frac{\vec{\nabla} I}{2cn_c} \equiv \vec{F_p} \tag{1.37}$$

$\vec{F_p}$ is called the ponderomotive force. This force repels charged particles from regions where the laser intensity gradient is large (whatever the sign of the charge). This ponderomotive force derives from a ponderomotive potential which is written as follow

$$\phi_p = \frac{I}{2cn_c} = \frac{e^2E^2}{4m_e\omega_0^2} \tag{1.38}$$

Numerical application
For an intensity $I_0 = 1\times10^{19}$ W/cm^2 and a wavelength 1 μm, one obtains a ponderomotive potential of $\phi_p = 1$ MeV.

Therefore, it is not possible to use the ponderomotive force as an accelerating mechanism to high energies. Nevertheless, it has an important role in the interaction because it drives a strong amplitude plasma wave. Work on the ponderomotive force in the relativistic regime and for a relativistic velocity of the plasma wave has also been reported (Mora and Antonsen, 1996, 1997; Quesnel and Mora, 1998).

1.3.2 Laser self-focusing

For a laser intensity above 10^{19} W/cm^2, the motion of an electron in an intense laser field becomes relativistic. In this case, local properties of the medium vary as function of the laser intensity. In particular, the refractive index in the equation of propagation (eq. 1.5) depends on laser intensity $\eta(I) = \eta_0 + \eta_2 I$. The plasma medium acts as a focusing lens for the electromagnetic field of the laser. If one considers only the relativistic contribution, the critical power for self-focusing P_c for a linearly polarized laser pulse is written (Sprangle et al., 1987) :

$$P_c = \frac{8\pi\varepsilon_0 m_e^2 c^5}{e^2}\frac{n_c}{n_e} \tag{1.39}$$

Numerical application
For an electron density $n_e = 10^{19}$ cm^{-3}, for a laser wavelength $\lambda_0 = 1\mu$m, one obtains a critical power $P_c = 2$ TW.

This formula doesn't account for other phenomena which also modify the refractive index : the plasma wave, the ponderomotive effect on the electrons, the ion channel created by a long prepulse. For instance, the plasma wave tends to defocus the laser pulse, which might prevent the pulse from self-focusing at P_c (Ting et al., 1990). Then, because of an electron density bump at the front of the plasma wave, the laser field in the first plasma bucket can't self-focus (Sprangle et al., 1992). Consequently, the laser pulse tends to erodes by the front. In particular, this theory predicts that it's not possible for a laser pulse shorter than the plasma wavelength to remain self-focused.

In reality, current experiments use very intense laser pulses $a_0 \gg 1$ and density perturbations are not linear anymore. Then, consequences on the self-focusing of very short laser pulses are less obvious.

1.3.3 Wave breaking

Up to now, we have considered only linear plasma waves. Under such assumptions, the maximal amplitude of the electric field is $E_{max} = E_0$ for a density perturbation equal to 1 (see Eq. 1.24). E_0 is called the non-relativistic wave breaking limit for cold plasmas. It reaches 300 GV/m for a density 10^{19} cm^{-3}. Please note the four order of magnitude when compared to conventional accelerators. In reality, for high plasma wave amplitudes, the density variation is no longer sinusoidal. The electric field can exceed E_0 (Dawson, 1959) (see Fig. 1.3).

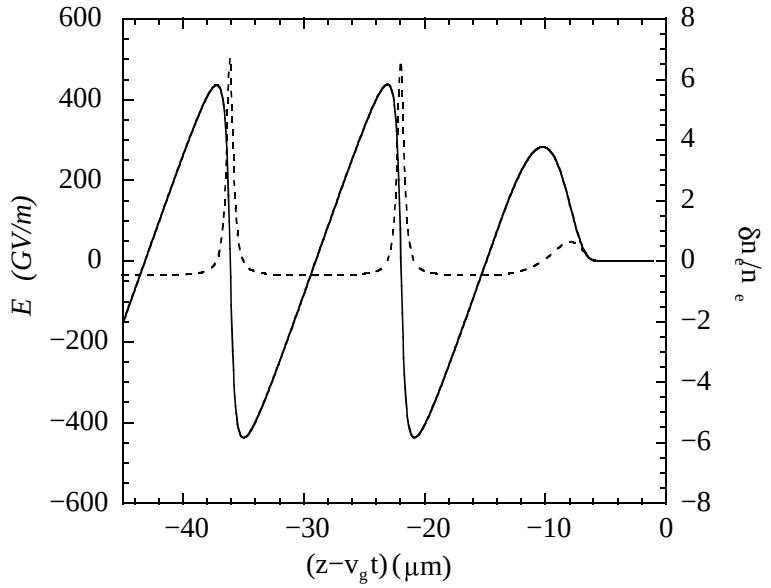

Figure 1.3: Example of electric field (solid line) and electron density (dashed line) for a non-linear plasma wave.

But the maximum electric field a plasma wave can sustain is limited by wave breaking. Wave breaking occurs when electrons which form the plasma wave are trapped in the wave itself and accelerated. This leads to a loss of structure of the electrons which create the electric field of the wave and therefore to the damping of its amplitude. Once again, the hydrodynamic analogy reveals to be useful to describe this process : when a wave reaches the coast, its profile steepens until foam appears on its peak and it breaks. The white foam which travels quickly on the wave corresponds to water molecules which initially took part to the collective motion of the wave and became trapped in the structure. The wave amplitude drops quickly then.

For a relativistic plasma wave, the electric field when wavebreaking occurs is (Arkhiezer and Polovin, 1956) :

$$E_{def} = \sqrt{2(\gamma_p - 1)}E_0 \tag{1.40}$$

This formula is obtained in the case of cold plasmas (where the tensor of pressure is neglected in 1.18). Thermal effects tends to trigger wave breaking before the cold limit (Rosenzweig, 1988; Katsouleas and Mori, 1988).

1.4 Acceleration mechanisms

At first glance, the electricmagnetic field doesn't seem a good solution to accelerate electrons : the electric field is mainly transverse to the propagation of the wave and its direction alternates every half period of the oscillation. Acceleration mechanisms presented here require an intermediary : the plasma wave. This one is excited by the laser pulse and allows to create a longitudinal electrostatic field favourable to the acceleration of electrons. The general diagram is represented on Fig. 1.4.

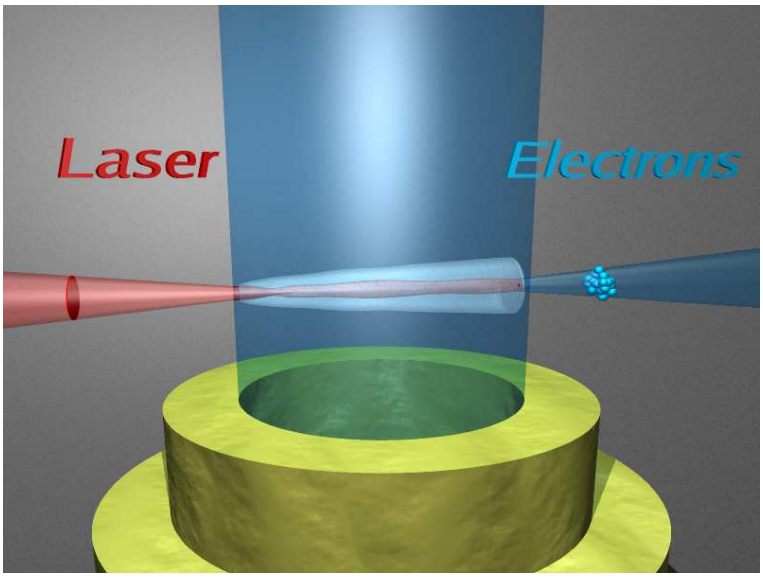

Figure 1.4: (Color) Principle of laser-plasma acceleration : from the interaction of an intense laser pulse with a gas jet, one obtains an electron beam at the output.

In section 1.2.3, a simple model of the electron acceleration in a plasma wave has been presented. Now, the link between the electricmagnetic field of the laser and the plasma wave has to be described. Several mechanisms have been developed to excite a large-amplitude plasma wave. These acceleration mechanisms have evolved as the laser pulse duration shortened and maximal intensity increased. Initially, the acceleration was well described by linear formulas. Then, as the intensity increased, non-linear mechanisms have appeared (Raman instability (Drake et al., 1974), relativistic self-focusing (Mori et al., 1988), relativistic self-modulation (McKinstrie and Bingham, 1992)) which allowed to reach even higher electric fields and particle beams with unique properties. A major improvement, which is one of the major feature of this thesis, is the measurement of electron beams with a quasi-monoenergetic spectrum. New theories have appeared to explain how to control the properties of this peak in the electron spectrum. These new theories will be introduced in section 1.5.

As explained in the introduction, it is also possible to drive a plasma wave with an electron beam coming from an accelerator. Electrons placed at the front of the bunch excite a plasma wave, in which electrons located at the back of the bunch can gain energy. At SLAC for instance, a gain of 2.7 GeV has been measured after 10 cm of plasma for electrons intially at 30 GeV (Hogan et al., 2005). This approach won't be described in this document.

1.4.1 Linear regime

Laser wakefield

Acceleration in a laser wakefield has been introduced by Tajima and Dawson (Tajima and Dawson, 1979). The perturbed electron density driven by the laser pulse is favourable to the acceleration of particles. The electron density profile obtained behind a gaussian laser pulse has been reported for $a_0 \ll 1$ (Gorbunov and Kirsanov, 1987). For a linearly polarized laser pulse with full width at half maximum (FWHM) $\sqrt{2\ln 2}L$ (in intensity), the normalized vector potential is written :

$$a^2(z,t) = a_0^2 \exp\left[-\left(\frac{k_0 z - \omega_0 t}{k_p L}\right)^2\right] \tag{1.41}$$

In this case, the associated electric field is

$$\vec{E}(z,t) = E_0 \frac{\sqrt{\pi} a_0^2}{4} k_p L \exp(-k_p^2 L^2/4)\cos(k_0 z - \omega_0 t)\vec{e}_z \tag{1.42}$$

Equation 1.42 explicitly shows the dependence of the amplitude of the wave with the length of the exciting pulse. In particular, the maximal value for the amplitude is obtained for a length $L = \sqrt{2}/k_p$ (see Fig. 1.5).

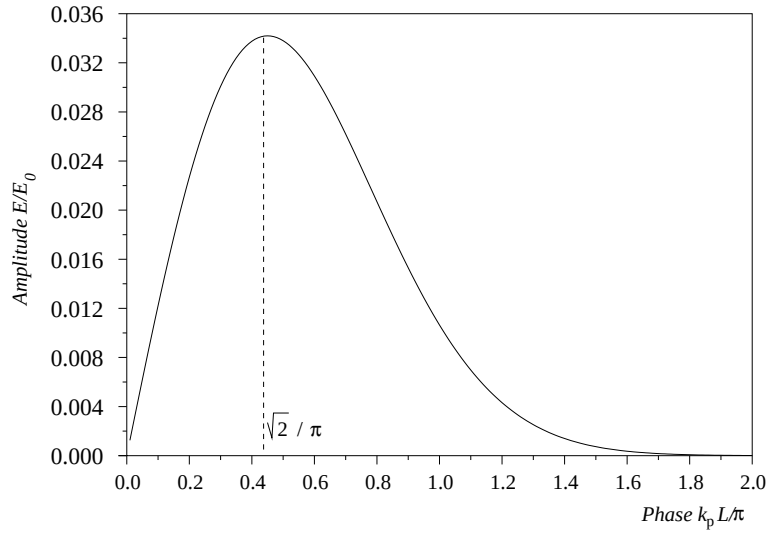

Figure 1.5: Amplitude of the electric field as function of the length of a gaussian laser pulse for a normalized vector potential $a_0 = 0.3$.

Numerical application
For an electron density $n_e = 10^{19}$ cm^{-3}, the optimal pulse duration equals $L = 2.4$ μm (equivalent to a pulse duration $\tau = 8$ fs). For $a_0 = 0.3$, the maximal electric field is $E = 10$ GV/m.

Beating wave

Initially, laser pulse durations were long compared to the plasma period. In order to have an efficient coupling between the laser pulse and the plasma wave, new techniques had to be developed to generate an electromagnetic wave at the plasma frequency. This requires two copropagating laser pulses with frequency ω_1 and ω_2 having a difference corresponding to the plasma frequency $\omega_2 - \omega_1 = \omega_p$.The overlapping of these two pulses then generates a beating wave at ω_p which drives resonantly the plasma wave. In this regime, the amplitude of the plasma wave reaches approximately 30% of the initial density, which limits the accelerating field to a few GV/m.

In 1993, Clayton *et al.* (Clayton et al., 1994) have obtained a final energy of 9.1 MeV for electrons injected initially at 2.1 MeV. Other experiments in this regime have also been carried out at UCLA (Everett et al., 1994) (gain of 30 MeV), at École Polytechnique (Amiranoff et al., 1995) and at Osaka (Kitagawa et al., 1992) for instance.

Physical processes which limit this technique are the motion of the ions, which has to be taken into account for such long pulses, the relativistic dephasing of the plasma wave for higher laser intensity and the growth of instabilities.

1.4.2 Non-linear regime

Self modulated wakefield

Thanks to the development of laser systems with a high power and a short pulse duration (500 fs), which could deliver a large energy (100 J), non linear effects in plasma could be studied. The cumulative effects of the self-focusing and the self-modulation of the laser envelope by the initial perturbation of the electron density generates a train of laser pulses which becomes resonant with the plasma wave. These effects are described on Fig. 1.6. The self-modulated laser wakefield regime has been investigated theoretically (Sprangle et al., 1992; Antonsen and Mora, 1992; Andreev et al., 1992). Their work show that when the laser pulse duration exceeds the plasma period and when the power exceeds the critical power for self-focusing, a unique laser pulse becomes modulated at the plasma wavelength during its propagation. This mechanism, called Raman scattering and which describes the decomposition of an electromagnetic wave into a plasma wave an a frequency shifted electromagnetic wave, gives finally modulations similar to those produced with two laser pulses by the beating wave technique and allows the acceleration of electrons (Joshi et al., 1981).

During experiments carried out in England in 1994 (Modena et al., 1995), the amplitude of the plasma waves reached the wavebreaking limit, where electrons initially belonging to the plasma wave are self-trapped and accelerated to high energies (see Sec. 1.3.3).The fact that the external injection of electrons in the wave is no longer necessary is a major improvement. They have measured an electron spectrum extending up to 44 MeV. This regime has also been reached for instance in the United States at CUOS (Umstadter et al., 1996), at NRL (Moore et al., 2004). However, because of the heating of the plasma by these relatively “long” pulses, the wave breaking occurred well before reaching the cold wave breaking limit, which limited the maximum electric field to a few 100 GV/m. The maximum amplitude of the plasma wave has also been measured to be in the range 20-60 % (Clayton et al., 1998).

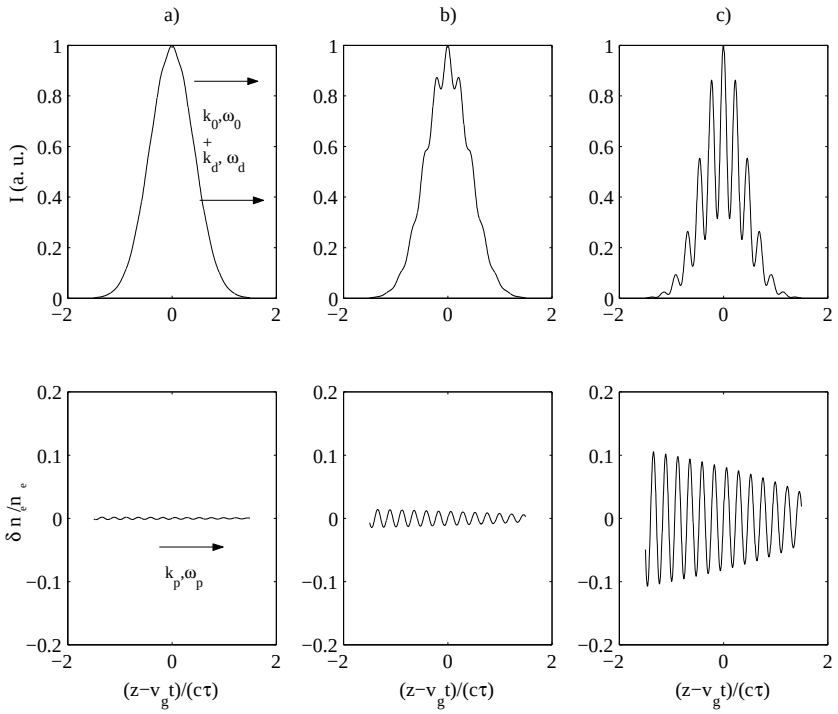

Figure 1.6: Self-modulation of the laser envelope and coupling with the plasma wave amplitude. Initially, the laser propagates on a plasma density perturbation (a). This modulates the laser envelope, which increases the coupling with the plasma wave, the amplitude of which increases (b). Finally, the self-modulation mechanism generates a train of laser pulses spaced by a plasma wavelength, which resonantly excites a large amplitude plasma wave (c).

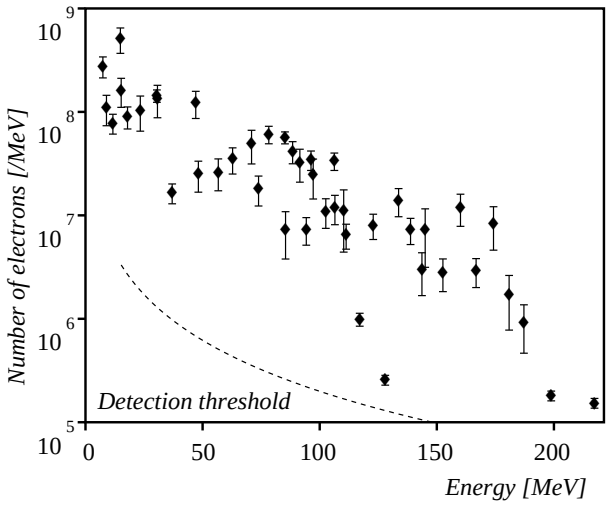

Figure 1.7: Typical electron spectrum obtained at $n_e = 7.5 \times 10^{18}$ cm^{-3} with a 1J-30fs laser pulse focused down to a waist of $w_0 = 18\mu$m.

Forced wakefield

These unique properties of laser-plasma interaction at very high intensity, previously explored only on very large infrastructures, became accessible for smaller systems, fitted to university laboratories. These laser systems, also based on chirped pulse amplification (Strickland and Mourou, 1985) and using here Titanium Sapphire crystals, fit in a room of several tens of meters square and deliver on-target energy of 2-3 J in 30 fs. This corresponds to 100 TW-class laser systems which can deliver an intensity of a few 10^{19} W/cm^2 after focusing. Many publications have shown that these facilities which deliver a modest energy and operate at a high repetition rate, can produce energetic electron beams with a quality higher than larger facilities. For instance, using the laser from "Salle Jaune" at LOA, electrons have been accelerated to 200 MeV in 3 mm of plasma (Malka et al., 2002). The mechanism involved is called forced laser wakefield to distinguish it from the self-modulated regime.

Indeed, thanks to short laser pulses, the heating of the plasma in the forced laser wakefield is significantly lower than in the self-modulated wakefield. This allows to reach much higher plasma wave amplitudes and also higher electron energies. Thanks to a limited interaction between the laser and the accelerated electrons, the quality of the electron beam is also improved. The measurement of the normalized transverse emittance has given values comparable to those obtained with conventional accelerators with an equivalent energy (normalized rms emittance $\varepsilon_n = 3\pi$ mm.mrad for electrons at 55 ± 2 MeV) (Fritzler et al., 2004).

Electron beams with maxwellian spectral distributions (exponential decay, see Fig. 1.7), generated by ultra-short laser pulses, have been produced in many laboratories in the world : at LBNL (Leemans et al., 2004), at NERL (Hosokai et al., 2003), and in Europe at LOA (Malka et al., 2001) or at MPQ in Germany (Gahn et al., 1999) for instance.

Bubble regime

More recently, theoretical work based on 3D PIC simulations have shown the existence of a robust acceleration mechanism called the bubble regime (Pukhov and Meyer-ter Vehn, 2002). In this regime, the dimensions of the focused laser are shorter than the plasma wavelength in longitudinal and also transverse directions. Thus, the laser pulse looks like a ball of light with a radius smaller than 10 μm. If the laser energy contained in this volume is high enough, the ponderomotive force of the laser expels efficiently electrons from the plasma radially, which forms a cavity free from electrons behind the laser, surrounded by a dense region of electrons. Behind the bubble, electronic trajectories intersect each other. A few electrons are injected in the cavity and accelerated along the laser axis, thus creating an electron beam with radial and longitudinal dimensions smaller than those of the laser (see Fig. 1.8).

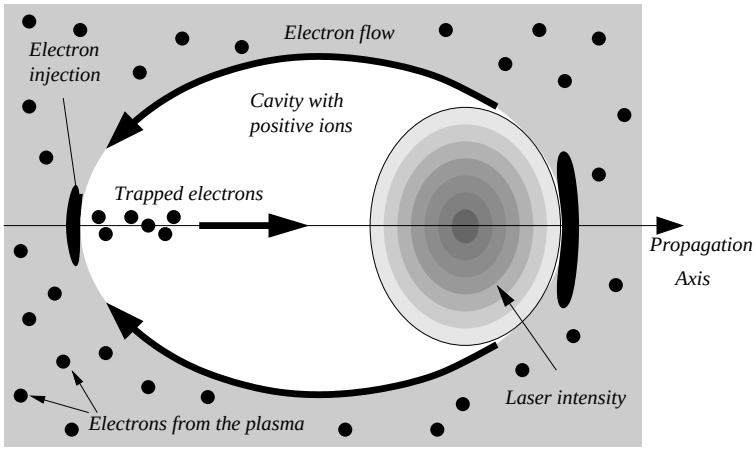

Figure 1.8: Acceleration principle in the bubble regime.

The signature of this regime is a quasi monoenergetic electron distribution. This contrasts with previous results reported on electron acceleration using laser-plasma interaction. This properties comes from the combination of several factors :

- The electron injection is different from that in the self-modulated or forced regimes. Injection doesn't occur because of the breaking of the accelerating structure. It is localized at the back of the cavity, which gives similar initial properties in the phase space to injected electrons.
- The acceleration takes place in a stable structure during propagation, as long as the laser intensity is strong enough.
- Electrons are trapped behind the laser, which suppresses interaction with the electric field of the laser.
- Trapping stops automatically when the charge contained in the cavity compensates the ionic charge.
- The rotation in the phase-space also leads to a shortening of the spectral width of the electron beam (Tsung et al., 2004).

Several laboratories have obtained quasi monoenergetic spectra : in France (Faure et al., 2004) with a laser pulse shorter than the plasma period, but also with pulses longer than the plasma period in England (Mangles et al., 2004), in the United States (Geddes et al., 2004), then in Japan (Miura et al., 2005) and in Germany (Hidding et al., 2006). The interest of such a beam in important for applications : it is now possible to transport and to refocus this beam by magnetic fields. With a maxwellian-like spectrum, it would have been necessary to select an energy range for the transport, which would have decreased significantly the electron flux.

1.5 Future of the laser-based acceleration

The building of even more powerfull laser facilities (Petawatt class, i.e. 10^{15} W), allows the prediction to even higher energies. The next step is to reach in routine the symbolic threshold of 1 GeV with these systems. The following theories show that it's also possible to reach 1 GeV with current 100 TW-class laser systems. In order to scale correctly the next experiments, theoretical studies are carried out for the acceleration to 1 GeV, either by extrapolating the bubble regime to higher energies, or using linear plasma waves which can be controlled more easily. The first one generates the electron beam in a single stage whereas the second one requires also the injection of electron with good initial properties. One says it is a two-stage acceleration process. It might also be possible to study stacks of linear stages (multi-stage approach) but problems of transport of the beam between stages also appear. This multi-stage approach won't be discussed in the following.

1.5.1 Extension of the bubble regime to higher energies, scaling laws

Fields in a relativistic spherical cavity

Fields in a spherical relativistic cavity have been reported analytically (Pukhov et al., 2004; Lu et al., 2006a). In order to simplify equations, ions are considered immobile on these time scales. However, for very high values of the vector potential, this assumption is no longer valid (Rosenzweig et al., 2005). The origin of the frame is placed at the center of the spherical cavity. Under the quasistatic assumption[1], electric and magnetic fields in the cavity have the following expression :

$$\left\{ \vec{E}_{cav}(x,y,z,t) = E_0 \frac{\omega_{pe}}{c} \begin{pmatrix} (x-v_p t)/2 \\ y/4 \\ z/4 \end{pmatrix} \quad \vec{B}_{cav}(x,y,z,t) = E_0 \frac{\omega_{pe}}{c} \begin{pmatrix} 0 \\ z/4 \\ -y/4 \end{pmatrix} \right. \tag{1.43}$$

This dependency of the fields matches pretty well PIC simulations in this regime (Fig. 1.9) (Pukhov et al., 2004). Slight mismatch with the formulas comes from an imperfect spherical structure in the simulations.

Similarity theory

Up to now, analytical equations have been obtained only with perturbative models or 1D non-linear regime. But a fully relativistic 3D theory was still missing to describe correctly

[1] equations depend only on $\xi = x - v_p t$ instead of x and t separately

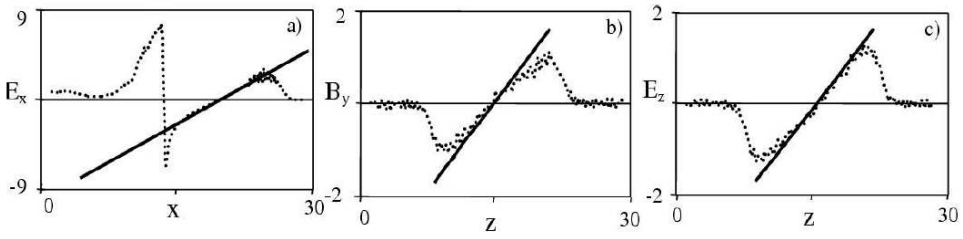

Figure 1.9: Comparison of the fields from the 3D PIC simulations (dashed line) with analytical formulas from Eq. 1.43 (solid lines). Axes have been normalized.

the interaction. Work has been done to obtain scaling laws to predict the properties of the electron beam (Gordienko and Pukhov, 2005; Lu et al., 2006b). The main results are reproduced here.

The first theory describes the similarity of the equations in an ultra-relativistic regime (Gordienko and Pukhov, 2005). After a strong assumption, these authors give the equations of motion with only three independent parmeters : the waist of the laser w_0, the pulse duration τ (FWHM) and the similarity parameter $S = n_e/(a_0 n_c)$. In other words, this similarity theory states that for given w_0 and τ, the laser pulse propagation and the electron beam properties depend on the variable S. If S is constant, one says that the propagation is similar : physical quantities can be scaled so that the simulation looks the same. This is shown on Fig. 1.10. Ions are also considered immobile here. Authors have also recently described similarity parameters for ions, which won't be discussed here.

In this regime (see Sec. 1.4.2), the electron spectrum is quasi monoenergetic and the properties of the electron beam can be described with this theory.

Assumptions In order to clarify the validity of the equation, here is a list of the assumptions required.

1. Ultra-relativistic limit : $a_0 \gg 1$. This assumption is used to normalize the velocity of all the electrons to c. Consequently, all electrons are relativistic, even those which are not trapped (and which form the accelerating structure). The authors try to detail the consequences and the conditions of validity of such an assumption (Pukhov and Gordienko, 2006).

2. Very under-dense plasma : $S \ll 1$.

3. The waist of the focal spot w_0 is adapted to the cavity : $k_p w_0 \sim \sqrt{a_0}$. This criterion corresponds to optimal conditions for the bubble regime, according to the authors.

4. The longitudinal length of the laser is smaller than its transverse dimensions : $c\tau_0 \leq w_0$.

5. The laser pulse duration is much longer than an optical cycle : $\omega_0 \tau_0 \gg 1$. This is required to define the envelope of the laser.

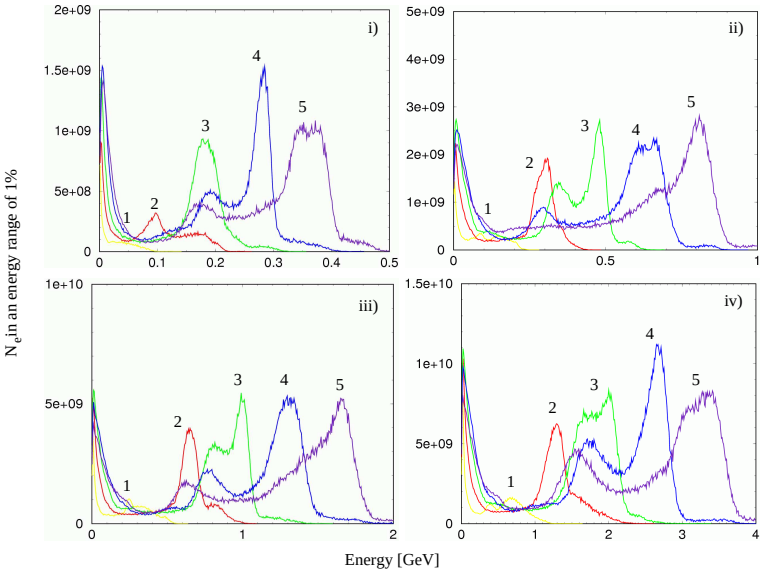

Figure 1.10: (Color) Principle of similarity. Simulations are shown for a constant parameter $S = 10^{-3}$. Curves with the same color correspond to similar times during the simulation. After a scaling of the axis, curves all look similar. These PIC simulations don't use the ultra-relativistic assumption from the theory. Parameters : i) $a_0 = 10$, $n_e = 0.01 n_c$, ii) $a_0 = 20$, $n_e = 0.02 n_c$, iii) $a_0 = 30$, $n_e = 0.03 n_c$, iv) $a_0 = 40$, $n_e = 0.04 n_c$

One notices that these constraints imply relations between different parameters of the interaction. Usually, it's not possible to modify only one parameters while keeping the other constants.

Scaling laws In these conditions, this theory predicts the properties of the quasi-monoenergetic electron beam obtained :

- The maximum energy of the quasi-monoenergetic peak E_{mono}

$$E_{mono} \sim 0.65 m_e c^2 \sqrt{\frac{P}{P_{rel}}} \frac{c\tau_0}{\lambda_0} \tag{1.44}$$

  where P is the power of the pulse, $P_{rel} = 4\pi\varepsilon_0 m_e^2 c^5 / e^2 \sim 8.5$ GW is the unit of relativistic power

- The number of electron in the quasi-monoenergetic peak is

$$N_{mono} \sim \frac{1.8}{k_0 r_e} \sqrt{\frac{P}{P_{rel}}} \tag{1.45}$$

  where $r_e = e^2/(4\pi\varepsilon_0 m c^2)$ is the classical radius of an electron.

- The acceleration length L_{acc}

$$L_{acc} \sim 0.7 Z_R \frac{c\tau_0}{\lambda_0} \tag{1.46}$$

  where $Z_R = \pi w_0^2/\lambda_0$ is the Rayleigh length.

- The conversion efficiency of laser energy to electron kinetic energy in the quasi-monoenergetic peak is

$$\eta \sim 20\% \tag{1.47}$$

The figures which appear in each formula have been obtained from 3D PIC simulations.

Numerical application
In order to reproduce the conditions presented in section 1.5.1, one chooses $a_0 = 10$ (assumption. 1), $c\tau_0 = 3.3$ μm (assumption. 5), $n_e = 10^{19}$ cm^{-3} (assumption. 2). Consequently, constraints give the waist of the beam (assumption. 3) $w_0 = \sqrt{a_0}k_p = 5.3$ μm which is higher than $c\tau$ (assumption 4). Using equations 1.13 and 1.14, one obtains the laser power $P = 75$ TW. The energy contained in this pulse is $U = P\tau_0 \sim 0.8$ J.
Consequently, predictions give an energy $E_{mono} = 126$ MeV, a charge of 1.3 nC for an acceleration length of $L_{acc} = 0.3$ mm.

With an equivalent energy, we have obtained experimentally a quasi-monoenergetic spectrum with an equivalent energy and charge. However, the acceleration length was 3 mm and the waist of the focal spot was 18μm. This theory implies some constraints which don't allow to explore all sets of parameters.

Existence According to the authors, the optimal conditions for this theory of similarity corresponds to the bubble regime for which assumptions 1, 3 and 4 give conditions on the electrons density which has to be in the range $n_1 < n_e < n_2$ (Pukhov and Gordienko, 2006).

$$n_1 \sim n_c \frac{P_{rel}}{P}, \quad n_2 \sim n_c \sqrt{\frac{P}{P_{rel}}} \frac{1}{(\omega_0\tau)^3} \tag{1.48}$$

This in turns requires the laser power to be above a given threshold

$$P > P_{rel}(\omega_0\tau)^2 \tag{1.49}$$

The cross-hatched area gives the domain of validity on Fig. 1.11. The point represents the experimental conditions at LOA, which is not in this area. Consequently, these formulas can't be used to estimate the results from our experiments.

Blow-out theory

This second theory relies on the calculation of the properties of the electron beam directly from the estimation of usual physical quantities (radius of the cavity, group velocity of the laser, dephasing length, ...) (Lu et al., 2006b). Before giving the scaling laws for the electron beam, here is the list of the assumptions.

Assumptions

1. Quasistatic assumption : the laser envelope evolves slowly during the interaction time with an electron. According to the authors, this is one of the main restriction to their theory towards ultra-relativistic intensities. The ponderomotive force applied to the electrons has to give a longitudinal velocity lower than the group velocity of the laser $a_0 < 2\sqrt{n_c/n_e}$. This implies that the electron density decreases as a_0 increases.

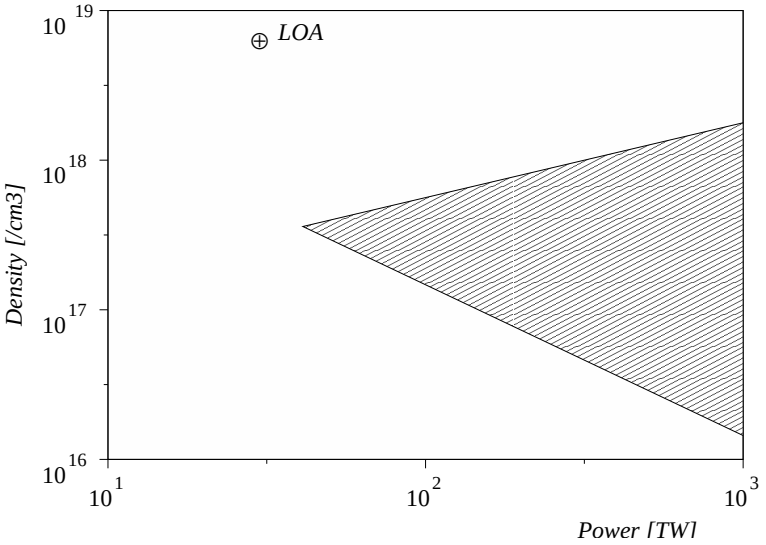

Figure 1.11: Electron density range corresponding to assumptions for the theory of similarity (Eq. 1.48) as function of laser power P. The point represents the experimental conditions at LOA. This graph corresponds to $\tau = 30$ fs.

2. Relativistic regime : $a_0 > 4$.

3. Very under-dense plasma : $\omega_p^2 \ll \omega_0^2$.

4. The waist of the focal spot w_0 is adapted to the cavity : $k_p R \sim k_p w_0 = 2\sqrt{a_0}$. The factor 2 is obtained from numerical simulations and corresponds to the minimization of the oscillations of the laser envelope during the propagation.

5. The depletion length is larger than the dephasing length which is equal to the interaction length : $L_{dp} > L_{deph}^{(3D)}$. The consequence is a minimum pulse duration $c\tau > 2R/3$.

Results The authors state that the velocity of erosion of the laser, based on 1D models (Ting et al., 1990; Bulanov et al., 1992; Decker et al., 1996), reproduce quite well the observations in 3D PIC simulations. The depletion length is then written

$$L_{dp} \sim \frac{\omega_0^2}{\omega_p^2} c\tau \tag{1.50}$$

Because of this depletion, the group velocity of the laser is smaller than the linear group velocity. Electrons injected at the back of the cavity reach its center after a dephasing length :

$$L_{deph}^{(3D)} \sim \frac{2}{3}\frac{\omega_0^2}{\omega_p^2} R \tag{1.51}$$

where R is the radius of the cavity

The properties of the electron beam are the following :

- The energy gain at the dephasing length is

$$E_{mono} \sim mc^2 \left(\frac{P}{P_{rel}}\right)^{1/3} \left(\frac{n_c}{n_e}\right)^{2/3} \tag{1.52}$$

  where P is the laser power and $P_{rel} = 4\pi\varepsilon_0 m_e^2 c^5/e^2 \sim 8.5$ GW is the unit of relativistic power.

- The maximum number of particles at this energy is obtained by equating the fields in the cavity :

$$N \sim \frac{8/15}{k_0 r_e}\sqrt{\frac{P}{P_{rel}}} \tag{1.53}$$

  where $r_e = e^2/(4\pi\varepsilon_0 mc^2)$ is the classical radius of an electron.

- The acceleration length is chosen to be equal to the dephasing length in order to have the narrowest spectral width

$$L_{acc} \sim \frac{4}{3}\frac{\omega_0^2}{\omega_p^2}\frac{\sqrt{a_0}}{k_p} \tag{1.54}$$

- for a pulse duration $c\tau = w_0$, the energy yield from laser energy to electron kinetic energy evolves as

$$\eta \sim \frac{1}{a_0} \tag{1.55}$$

These formulas differ from the ones described in the similarity theory. The authors explain that the acceleration length is different. In these formulas, the acceleration length L_{acc} is linked to the dephasing of the electrons in the structure. In the similarity theory, the acceleration length is limited by the breaking of the plasma wave, in order to guarantee a quasi-monoenergetic peak. This also limits the maximum energy of the electrons and these formulas follow different scaling laws.

Numerical application
For a laser pulse with $a_0 = 10$, $c\tau_0 = 3.3$ μm in an electron density $n_e = 10^{19}$ cm^{-3}, the assumptions are all verified, and in particular the quasistatic assumption (assumption. 1) and the depletion length is equal to the dephasing length (assumption. 5). Consequently, predictions give an energy $E_{mono} = 324$ MeV, a charge of 0.4 nC for an acceleration length $L_{acc} = 1.2$ mm.

1.5.2 Injection and linear acceleration

Current acceleration techniques rely on highly non-linear mechanisms. Consequently, fluctuations on the parameters of interaction can have a dramatic impact on the stability of the electron beam. Linear methods for laser plasma acceleration allow a better control of the electron beam properties at the output. Theoretical studies and simulations have been carried out in linear structure to reach 1 GeV (Andreev and Kutnetsov, 2000; Gorbunov et al., 2005; Lifschitz et al., 2006). This accelerator requires two stages : the injection of a short electron bunch, produced by current laser-based acceleration techniques, and an

acceleration stage in a linear plasma structure created by a petawatt laser. Powerful laser pulses are focused in a large focal spot $w_0 \sim 100\ \mu$m, which allows to neglect self-focusing effects (even if the ratio P/P_c doesn't evolve).

Under these conditions, it it possible to control the final energy and the spectral width of the electron bunch. Analytic formulas can be obtained under some assumptions : the acceleration length is considered to be very small compared to the dephasing length and the properties of the laser don't evolve, which allows to neglect the phase evolution in the plasma wave (constant electric field). Moreover, Coulomb repulsions in the electron bunch and the influence of accelerated electrons on the plasma wave are neglected. Under these assumptions, the final properties in energyE_{mono} and in dispersion δE for an electron beam injected at energy E_i with a dispersion δE_i after an accelerating distance between $z = -Z_r$ and $z = Z_r$ are (Lifschitz et al., 2005) :

$$E_{mono} = E_i + \frac{1}{2}\hat{\delta}(k_p w_0)^2 \gamma_p \tag{1.56}$$

$$\delta E = \delta E_i + \frac{1}{2}\hat{\delta}\left(1 - \cos(2\pi L_b/\lambda_p)\right)(k_p w_0)^2 \gamma_p \tag{1.57}$$

with $\hat{\delta} = 0.79\sqrt{\pi} a_0^2 \frac{L_0}{4} \exp -L_0^2/4$ and $L_0 = \omega_p \tau_0/\sqrt{4\ln 2}$, where L_b is the initial bunch length and τ_0 the laser pulse duration.

Numerical application

One considers a petawatt-class laser $P = 1$ PW, a pulse with a waist $w_0 = 100\mu$m and a duration $\tau_0 = 30\,fs$ which propagates in an electron density $n_e = 10^{17}$ cm^{-3} and an electron bunch of length $L_b = 5\mu$m. Under these conditions, the normalized vector potential is $a_0 = 1.76$, which satisfies approximately the numerical conditions to neglect self-focusing for a large laser waist (Gorbunov et al., 2005).
The final energy is then 910 ± 50 MeV for an electron beam initially at 170 ± 25 MeV (this corresponds to the quasi-monoenergetic electron beam obtained experimentally and described in the next chapter).

Thanks to a large waist, the maximum acceleration length corresponds to twice the Rayleigh length $2Z_r = 8$ cm. Similar results on the electron beam can be obtained when using a channel for a lower laser energy, corresponding to 100 TW-class laser systems (Malka et al., 2005a). Using a channel to guide the laser pulse, it is possible to have higher energy gains and to control precisely the final energy by the interaction length (see Fig. 1.12).

Simulations have also been performed to illustrate the control of the spectral width. With an energy of 10 J in a an electron density of 3×10^{16} cm^{-3} on-axis, a spectral width of 2 % at 1.2 GeV has been obtained in the simulation (Malka et al., 2005c) (see figure 1.13).

1.5.3 Alternative techniques

It has also been suggested to inject low energy electron in front of the laser pulse (Khachatryan et al., 2004). Hydrodynamic simulations show that the laser pulse overruns the injected electrons, which are trapped in the first arch of the accelerating structure created

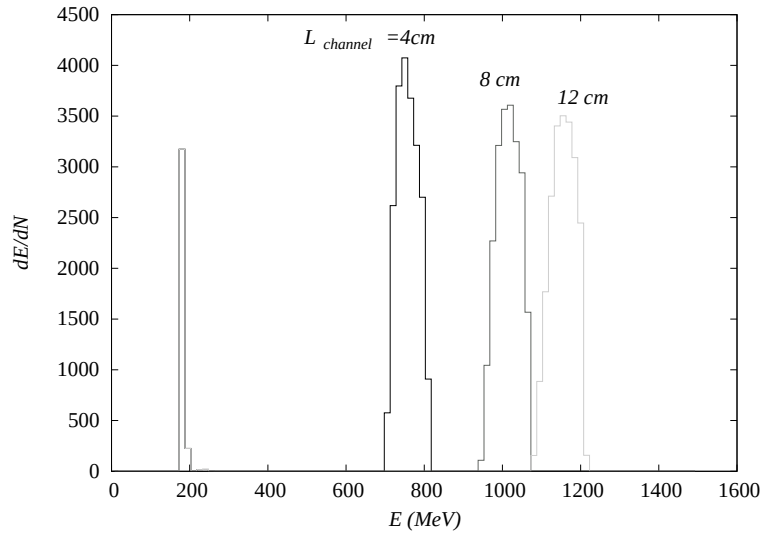

Figure 1.12: Electron spectra obtained using a guided laser pulse in the second stage, for acceleration length of 4, 8 and 12 cm. Parameters of the injected electrons : bunch duration 30 fs, energy 170 ± 20 MeV, divergence 10 mrad and charge 0.5 nC. Parameters for the channel : on-axis electron density $n_0 = 8.6 \times 10^{16}$ cm^{-3}, radius $r_0 = 40$ μm, parabolic profile with a density $3n_0$ at r_0. Parameters for the laser : duration 78 fs, power 140 TW, energy 11 J, intensity 4.2×10^{18} W/cm^2, waist 46 μm.

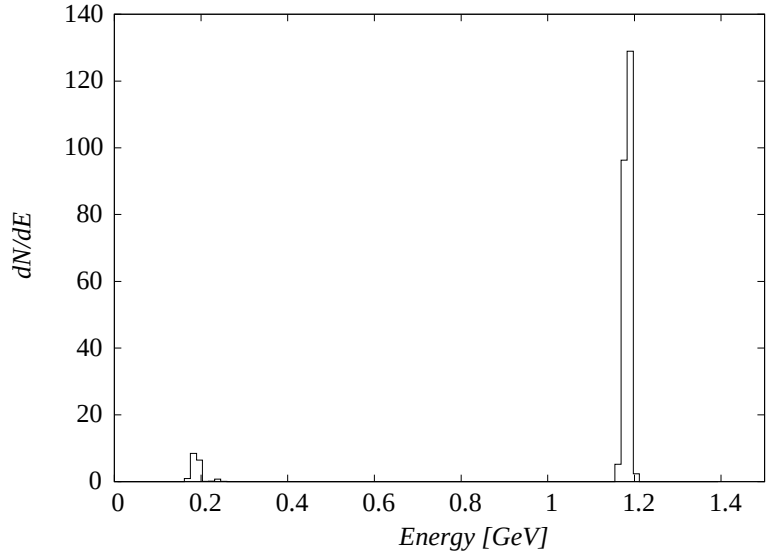

Figure 1.13: Electron spectrum using a guided laser pulse in the second stage for an acceleration length of 19 cm. Parameters of injected electrons : bunch duration 30 fs, energy 170 ± 20 MeV, divergence 10 mrad and charge 0.5 nC. Parameters for the channel : on-axis electron density $n_0 = 3.0 \times 10^{16}$ cm^{-3}, radius $r_0 = 70\mu$m, parabolic profile with a density $3n_0$ at r_0. Parameters for the laser : energy 10 J, power 160 TW, normalized amplitude $a_0 = 1$.

behind the laser. However, as in the previous case, the charge in the accelerated bunch is limited to guarantee the validity of the assumptions. But here, Coulomb repulsions, which are neglected for such low energy electrons, might have catastrophic consequences on the quality of the electron beam. Then, the transverse electric field of the laser might also significantly degrade the emittance of the electron bunch when it is being overrun.

There exist other methods emphasizing the control of the injection when using two counter propagating laser pulses. A first beam, the characteristics of which can't trigger the wave breaking, drives a plasma wave. The injection is controlled by a second counter-propagating pulse with lower intensity. The beating of the two pulses triggers the injection of a small amount of electrons in the accelerating structure (Esarey et al., 1997; Sheng et al., 2004; Fubiani et al., 2004).

The guiding of the laser pulse over longer distances allows also to reach higher energies (Tsung et al., 2004). Using capillary discharges, the team from LBNL has obtained electrons with energy higher than 1 GeV, but detailled results are not known yet.

The development of the acceleration towards higher energies is one of the possibilities of this source. It is also planned to inject an electron beam from a laser-plasma accelerator in these structures. Actually, accelerating cavities in the plasma waves are very short (approximately 10 μm at an electron density of 10^{19} cm^{-3}) and photocathodes used on conventional accelerators are not adapted. The quasi-monoenergetic electron beam presented in the next chapter is a good candidate for the injection : it is short an consequently can be injected so that all electrons can see a similar electric field. Synchronization of the injection with the following accelerating stages is ideal because everything can be driven by the same initial laser pulse splitted in several arms. However, the stability has to be improved before this source can be used as an injector. These issues of the control and the stability of the properties of the electron beam are the center of current development of the laser-plasma electron accelerator. This requires stable laser systems and less extreme operating conditions compared to the specifications of the laser facility.

Chapter 2

Quasi monoenergetic spectrum and optimization

This section presents experimental results based on the characterization of the interaction. For a better clarity, the experimental setup is presented first, followed by examples of the quasi-monoenergetic electron beam obtained and finally the optimization performed to obtain these results.

2.1 Description of the experiment

This section describes the laser system used during the experiments and the experimental setup used for the characterization of the electron beam. Complementary and more detailled explanations on the electron spectrometer are given in Appendix B and C.

2.1.1 Characteristics of the laser in "salle jaune" at LOA

The laser in "salle jaune" (Pittman et al., 2002) at Laboratoire d'Optique Appliquée operated in chirped pulse amplification mode (Strickland and Mourou, 1985) with a Ti:Sapphire crystal in the infrared. It delivers 30 TW laser pulses in 30 fs at a repetition rate of 10 Hz.

The laser system contains a self-modelocked Ti:Sa oscillator, which delivers a train of pulses of 300 mW and 18 fs at a repetition rate of 88 MHz. These pulses are stretched in an aberration-free stretcher and injected in a Dazzler (acousto-optical filter). This device allows an active control of the spectrum and spectral phase of the pulse. A Pockels cell is then used to select pulses at a repetition rate of 10 Hz. The opening gate gives control of the ASE (amplified spontaneous emission) level, which defines the pulse contrast. The 1nJ pulses selected are then amplified in three multi-pass stages, after which the energy reaches sequentially 2 mJ, 200 mJ and 2.5 J. Between amplification stages, spatial filters enhance the fundamental spatial mode which limits hot spots in the beam profile to values below the damage threshold in crystals. The crystal in the third stage is also cryo-cooled, which reduces thermal effects. After entering a secondary vacuum level, pulses are recompressed on a pair of gratings (double pass) and send to the interaction chamber. The compressor efficiency is 55 %, which gives pulses of 30 fs (FWHM) containing an energy of about 1.3 J on target. The pulse contrast on the nanosecond scale is better than 10^6.

In experiments described hereafter, the focused pulse reaches a peak intensity of $I = 3 \times 10^{18}$ W/cm^2 which corresponds to an ASE level below the direct ionization threshold (of the order of 10^{14} W/cm^2). Thus, the laser propagates in a initially homogeneous medium, which is important for the propagation of the laser.

2.1.2 Experimental setup

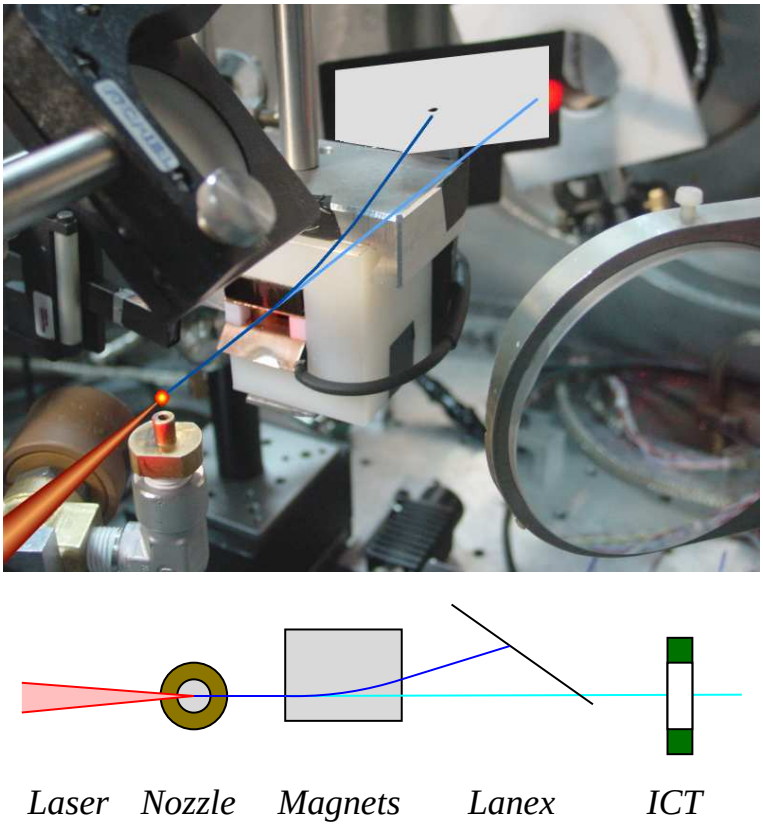

Figure 2.1: (Color) Experimental setup. The laser is focused onto the edge of the gas jet. Trajectories of accelerated electrons are bent by the magnetic field of a permanent magnet and crosses a scintillator screen. The emitted light is then imaged onto a CCD camera. The integrating current transformer (ICT) has also been used to estimate the charge.

The experimental setup is shown on figure 2.1. The laser is focused with a parabolic mirror with focal length of 1 m onto the steep gradient at the front of a supersonic helium gas jet with diameter 3 mm. This light gas is fully ionized by the pedestal of the laser pulse. The atomic density profile of the gas jet, measured by interferometry, corresponds to a uniform density at the center and steep gradients (Semushin and Malka, 2001). These interaction conditions are used as a reference in the following.

The electron density is controlled by the pressure from the gas bottle, which allows to scan densities in the range $n_e \in [10^{17}; 10^{19}]$ cm^{-3}, i.e. plasma wavelength $2\pi c/\omega_{pe}$ between 11 and 110 μm. These valueshave to be compared to focused laser dimensions : the laser waist at the interaction point is diffraction limited $w_0 = 18$ μm and its duration

corresponds to a length $c\tau$ of 9 μm. The physics involved is therefore the forced laser wakefield or the bubble regime (Sec. 1.4.2).

Behind the interaction point, we place an electron spectrometer. During my first experiments, we used an imaging spectrometer composed of an electromagnet and 4 silicon diodes (Fig. 2.2). This detector was heavy and cumbersome, thus difficult to align along the laser axis. This combination of an imaging spectrometer an diodes gave a high resolution and a good sensitivity to electrons. The energy intercepted by each diode could be varied by modifying the intensity flowing in the electromagnet. However, each shot gave only 4 points, which required the accumulation of many shots with different magnetic fields to reproduce the full spectrum. This measurement was adapted to electron spectra with reproducible properties.

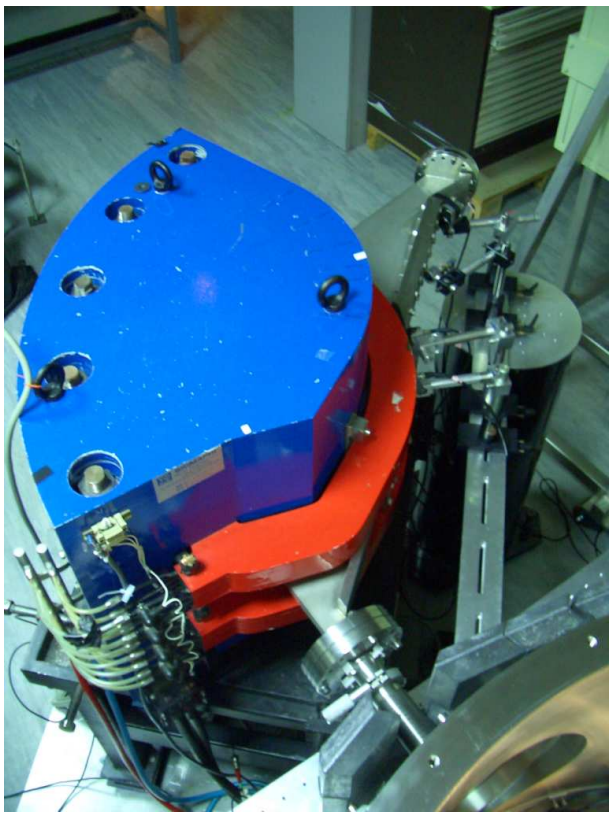

Figure 2.2: (Color) imaging spectrometer composed of an adjustable magnetic field and 4 silicon diodes.

Recently, we have observed a significant improvement of the properties of the electron beam. By decreasing the pressure, an electron beam with a low divergence could be obtained (10 mrad). At such pressures, the signal on the diodes fluctuated by several orders of magnitude at high energy. We were thinking that we missed interesting features with only 4 diodes. A new single shot electron spectrometer has been developed and set-up on the experiments. This is a light and compact system (see Fig 2.1) which gives the whole spectral information for every shot.

This spectrometer is composed of a permanent magnetic field $B_m = 0.45$ T at the center, which bends the electron trajectory according to their energy, and a scintillator, the

relaxation transition of which is excited by the electron flow, which is imaged onto a CCD camera with a high bits depth (16 bits). We also use an interference filter just in front of the objective to select the central wavelength in the emission spectrum of the phosphor screen. The spectrum amplitude is calibrated either with an integrating current transformer (ICT), placed behind the scintillator, or using an absolute calibration presented in Appendix C (Glinec et al., 2006a). In optimal conditions, the divergence of the electron beam is very low (see next section) and no collimator is used with this spectrometer.

We also usually use a shadowgraphy diagnostic (side view) and a Thomson scattering diagnostic (top view) to look at the interaction and place precisely the laser axis at 1 mm above the center of the nozzle.

2.2 Quasi monoenergetic spectra

2.2.1 Improvement of the quality of the electron beam

First, we have measured the electron beam profile as function of the parameters of interaction. The magnets were removed and the scintillating screen was placed perpendicular to the laser axis. Fig. 2.3 shows the evolution of the spatial quality of the electron beam with the electron density. The diameter of the circle corresponds to a divergence of 14°. At high electron density, the signal is nearly homogeneous. As the density is decreased, structures appear in the beam. The signal fluctuates from shot to shot. In these conditions, the plasma wavelength ($\lambda_p = 11$ μm for 10^{19} cm^{-3}) is similar to the laser pulse length ($c\tau_0 = 10$ μm full width at half maximum (FWHM), but reaches 15 μm at $1/e^2$ of the laser envelope intensity). The regime involved is the SMLFA or the FLWA, for which the acceleration takes place due to the breaking of the accelerating structure, leading to random structures. Moreover, the simultaneous interaction with the electric field of the laser worthens the electron beam quality.

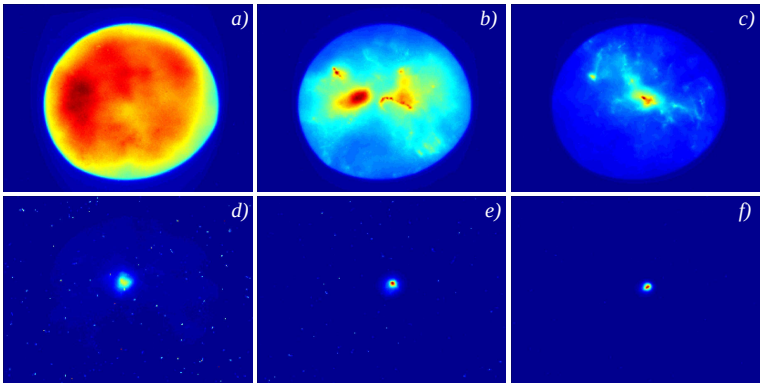

Figure 2.3: (Color) Transverse profile of the electron beam as function of the electron density : a) $n_e = 50 \times 10^{18}$ cm^{-3}; b) 30×10^{18} cm^{-3}; c) 20×10^{18} cm^{-3}; d) 10×10^{18} cm^{-3}; e) 7.5×10^{18} cm^{-3}; f) 6.0×10^{18} cm^{-3}.

When the electron density reaches $n_e = 10^{19}$ cm^{-3}, there remains only one fine structure, testifying a transition. This is due to a reduced interaction with the laser field and probably to a more robust accelerating structure. The divergence of this real electron

beam is estimated to 6 mrad (FWHM) for Fig. 2.3f. For even lower electron densities (below 6.0×10^{18} cm^{-3}), the electron beam observed is still very collimated but the signal intensity drops quickly.

The quality of the interaction seems to be excellent at low electron density in terms of divergence and stability. The single shot electron spectrometer was then installed to check also the quality of the electron spectrum.

2.2.2 Experimental spectra

This single shot electron spectrometer allows to see the fundamental difference between the two spectra shown in Fig. 2.4. The laser axis is shown in a dashed line. The electrons trajectory is bent to the right by the magnetic field and their impact distance to the laser axis depends on their energy. The more energetic, the closer. Some reference energies have been represented along the horizontal axis (20, 50, 100 and 200 MeV). The vertical axis corresponds to the natural divergence of the electron beam. No collimator is used and the resolution is limited by the divergence of the beam. In particular, the signal on Fig. 2.4a is too divergent to give any information on the electron energy. However, the signal seems to spread over a large energy range, contrary to the signal presented on Fig. 2.4b. Here, a narrow electron signal is recorded at high energy. This quasi-monoenergetic electron beam is a real improvement of the quality of this electron source.

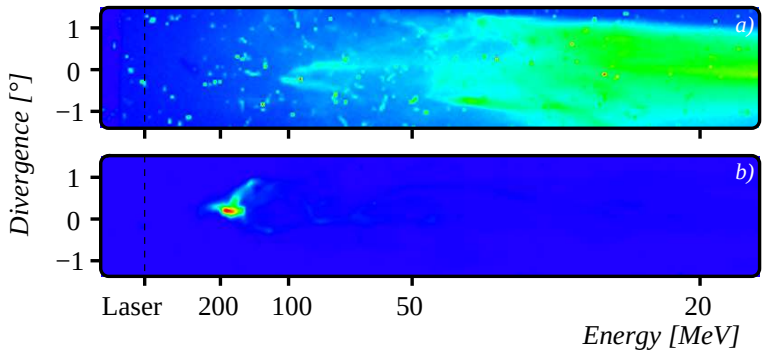

Figure 2.4: (Color) Example of spectra obtained for an electronic density : a) 1.5×10^{19} cm^{-3}, b) 6.0×10^{18} cm^{-3}. Images have been normalized independently.

This spectrum, obtained at an electron density 6.0×10^{18} cm^{-3}, is represented on a linear scale after taking into account the energy dispersion along the screen and the stopping power in the scintillating screen in Fig. 2.5. The electron peak appears at 170 ± 20 MeV and contains a large charge (estimated to 0.5 ± 0.2 nC in the peak). The spectral width is comparable to the spectrometer resolution at this energy (represented by the horizontal line). The second curve comes from a Particle In Cell (PIC) simulation which is presented in the following.

Null tests have been performed to check the origin of the signal : without magnet, the signal is centered on the laser axis, which means these are charged particles. When inserting a 2 mm-thick lead plate just in front of the scintillating screen, one obtains a scattered signal, corresponding to electrons with energy above 3 MeV scattered during propagation.

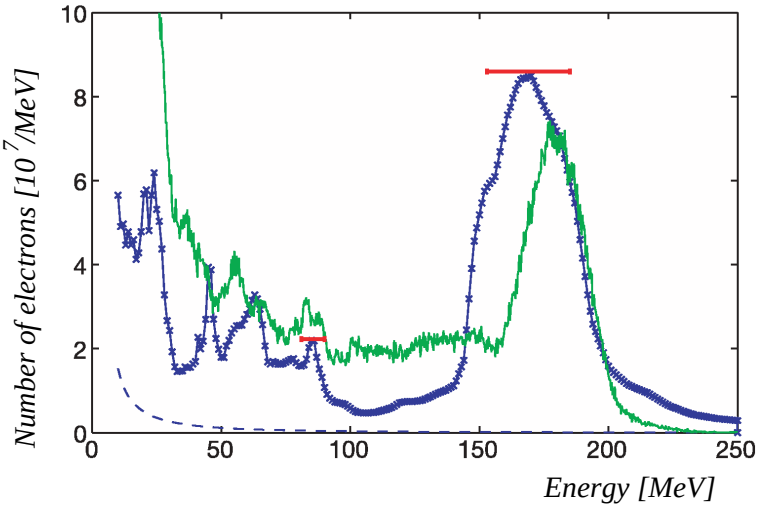

Figure 2.5: (Color) Superposition of the experimental spectrum (blue crosses), obtained from Fig. 2.4b, and the corresponding PIC simulation (green line) after 2 mm of propagation. The dashed curve is the detection limit. The horizontal lines give the resolution of the spectrometer.

Quasi-monoenergetic spectra were obtained also by other groups and these major results were published in the same issue of the *Nature* paper (Mangles et al., 2004; Geddes et al., 2004; Faure et al., 2004). Since then, many other laboratories working in the field of particle acceleration using laser-plasma interaction have also obtained quasi-monoenergetic structures (Miura et al., 2005; Hidding et al., 2006; Hsieh et al., 2006; Hosokai *et al.*, 2006; Hafz et al., 2006; Mangles *et al.*, 2006).

These properties are fundamental in order to develop applications of laser-based electron acceleration. Actually, it's impossible to transport and focus properly an electron beam with a wide spectrum, due to chromaticism of magnetic optics. A reduction of the spectral width (using a monochromator) also lead to a decrease of the flux. Here ,the electron beam naturally contains a high charge in a restricted spectral range and its divergence is low. Moreover, due to the acceleration process involved, the electron bunch duration at the output of the plasma is expected to be short (shorter than the plasma wavelength) and should remain short upon propagation (stretching of 50 fs/m due to velocity dispersion for this electron beam).

The expression "quasi monoenergetic" is used in this document to distinguish these spectral properties from laser-plasma interaction from electron beams obtained on conventional accelerators where "monoenergetic" refers to a relative spectral width $\delta E/E$ of the order of 1 percent or below. Here, the spectral width is limited by the resolution of the spectrometer and equals $\delta E/E \sim 20$ %.

2.2.3 Comparison to 3D PIC simulations

For a better understanding of the physics involved in this experiment, 3D PIC simulations have been carried out at Virtual Laser Plasma Laboratory (Pukhov, 1999) for the same interaction conditions. The electron spectrum obtained is merged to the experimental one

in Fig. 2.5. One can see a quasi monoenergetic spectrum at 175 ± 25 MeV containing a similar charge. The electron beam divergence agrees also with the experiments (10 mrad). However, the two spectra are not obtained in exactly the same conditions : the curve from the simulation corresponds to a propagation distance over 2 mm in the plasma.

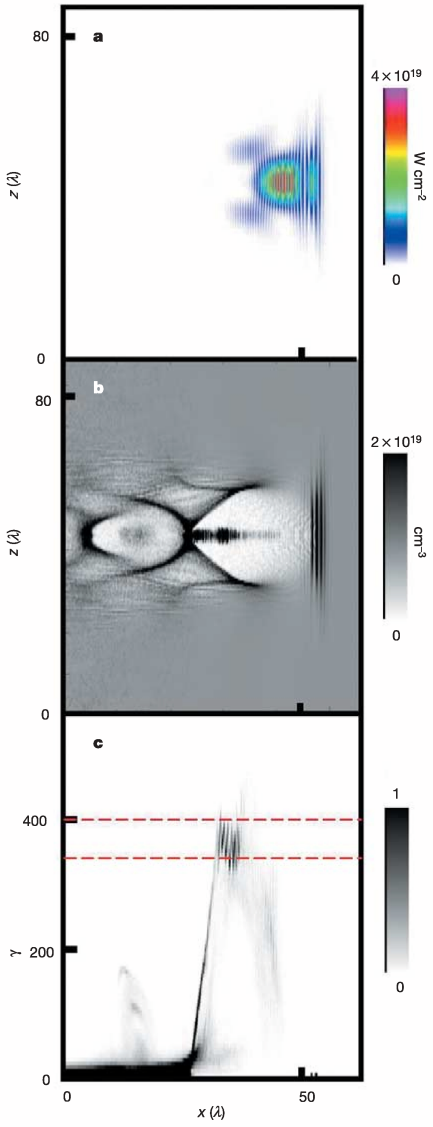

Figure 2.6: (Color) Snapshot of the 3D PIC simulation. (a) laser intensity profile and (b) electron density in the plane perpendicular to the polarization of the laser and containing the laser axis. The laser beam propagates from left to right and has propagated over 2 mm in the plasma at this time. (c) Phase space of the accelerated electrons.

Fig. 2.6 shows the laser intensity profile, the electron density profile in the plane perpendicular to the polarization of the laser and containing the propagation axis, and the phase space of the accelerated electrons. One clearly sees an ionic cavity created by the laser pulse into the electron density profile. The acceleration process can be summarized as follows : the ponderomotive force of the laser (ie the radiation pressure) expels the

electrons from large intensity gradients. This leads to an electron density bump at front of the pulse and an ionic cavity behind the pulse. Some of the electrons which flow around the cavity and intersect themselves at its back are trapped in the accelerating structure, which forms the cylinder of electrons on the laser axis. The phase space in Fig. 2.6c shows the electron energy as function of its position along the laser axis. The most energetic electrons have dephased with respect to the plasma wave and they have reached the center of the cavity. The laser field is located at the front on the cavity, which reduces the interaction of the electrons with the defocusing laser field.

One also notes that the laser intensity at this time in the simulation is 10 times higher than the intensity in vacuum. This is due to self-focusing which takes place during the first part of the simulation, during which the transverse size of the laser becomes resonant with the plasma wavelength $\lambda_p = 14$ μm. In the meantime, the laser pulse duration is shortened by the plasma wave. The laser pulse looks like a ball of light which excites a high amplitude plasma wave, thus creating a cavity in its wake. The cavity elongates as electrons are injected in this cavity, and the injection stops when the charge in the cavity compensates the ionic charge. Despite injection at various times, the rotation of the electrons in phase space leads to a shortening of the spectral bandwidth after a dephasing length, which leads to a quasi-monoenergetic electron beam.

2.2.4 Absolute calibration of the scintillating screen and discussion about the charge

The measurement of charge using an ICT raises several issues and an independent calibration technique is required. I worked on the absolute calibration of the detection system to provide the direct relation between the number of electrons and the number of counts (Glinec et al., 2006a). This technique also provides with a local information for each pixel, contrary to the ICT which gives a global estimation of charge over an area difficult to estimate. In principle all electron should be flowing in the core of the ICT. In our experiment, some electrons travel inside the coil or in the vicinity of the ICT and their influence is not known. I have considered two extreme cases, where inner and outer diameter (respectively 55 mm and 100 mm) are used to determine the spectral amplitude. Consequently, the intercepted spectral distribution corresponds to electrons with energy above 115 MeV and 55 MeV respectively. Because, the normalization corresponds to different sizes of the electron distribution, the uncertainty on the effective diameter of the device leads to a large errorbar in the amplitude.

Fig. 2.7 shows the evolution of the charge for the same series of shot either using the ICT or the absolute calibration. One notices that the two curves don't match and that the ICT always overestimates the value from the absolute calibration. The absolute calibration gives a charge of about 63 pC for Fig. 2.4.

Moreover, at low electron density the variation of the signal is about 2 decades for the absolute calibration and only one decade for the ICT, revealing probably a better sensitivity of the absolute calibration. This electronic device is probably sensitive to the huge electro-magnetic field from the laser at the interaction point and therefore was placed as far as possible from the interaction point (~ 50 cm). In order to block low energy electrons, lead shielding was placed around the magnet, because low energy electrons may be integrated by the ICT even if we don't see them in the scintillator. Without gas (only

laser), the signal from the ICT dropped to the noise level. Unfortunately despite this carefull attention to the ICT, it seems that it still gives a biased estimation of the charge. This conclusion on the inadequacy of the ICT for our experiments may be relevant for many other labs using the same detection system.

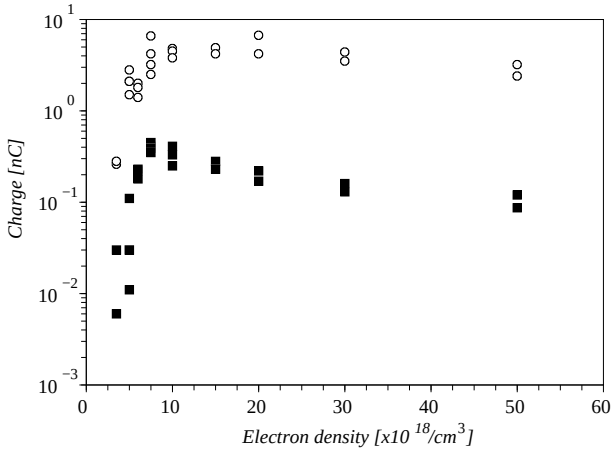

Figure 2.7: Evolution of the charge as function of the electron density using either the ICT (circles) or the number of counts on the CCD (filled diamonds). Both diagnostics shows that the charge is maximum for the optimal electron density where the electron beam quality is the best.

This absolute calibration seems to be the most accurate but one should keep in mind the assumptions implied. Electrons beams from laser-plasma interaction are much shorter than those from conventional structures. This calibration assumes that the calibration of the scintillator screen (Lanex Kodak Fine) performed on a conventional radiofrequency accelerator (at ELYSE) in the range 3-9 MeV can be extended to our experimental conditions. However, for such dense energy deposition, higher atomic levels might be excited and relaxation trajectories might differ from the usual irradiation conditions, which would affect the light yield. Finally, we have never observed any direct evidence of saturation of the scintillator.

Fig. 2.8 shows other examples of quasi-monoenergetic spectra for various experimental configurations. The amplitude is determined using the absolute calibration. Spectrum labelled a) contains a charge of about 9 pC ($120 < E < 160$ MeV) and 250 pC ($E > 55$ MeV) for image b). This second image shows that this calibration still gives quasi monoenergetic spectra containing a few hundreds of picocoulombs as previously published (Faure et al., 2004). Even if the raw signal shown in inset is very narrow, the peak is significantly broadened during the deconvolution due to a lack of resolution towards high electron energy. Using a more dispersive magnet will improve the resolution at high energy. However, image a) gives a spectral width of 6% (FWHM). One also notices the low amount of low energy electrons for this shot.

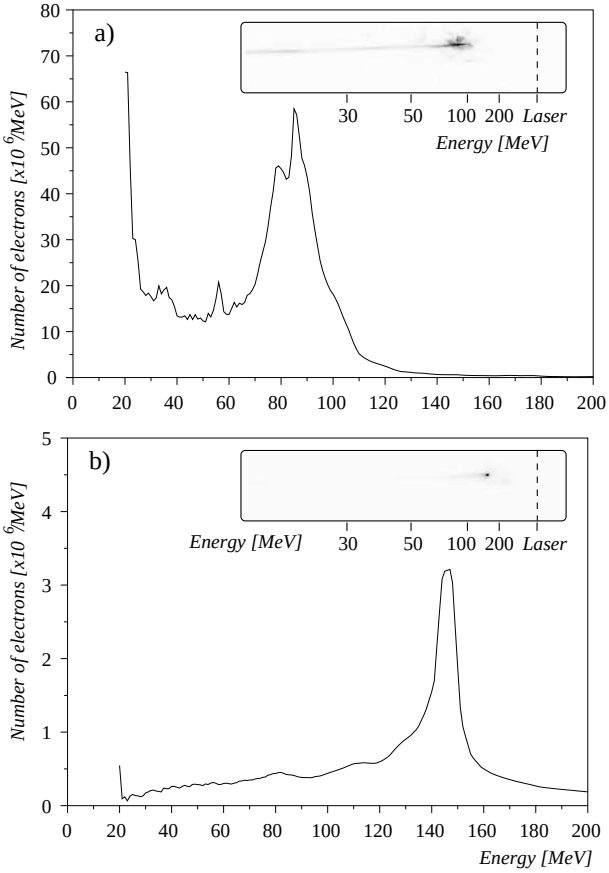

Figure 2.8: Spectra obtained after deconvolution of the images shown in inset. The amplitude is determined using the absolute calibration..

2.3 "quasi monoenergetic" regime in a narrow range of parameters

Obtaining such a quasi-monoenergetic spectra was not an easy task and the parameter range where it was observed is very narrow with our present laser system (Glinec et al., 2005). Here, I list the influence of each parameter of the interaction on the measured spectra. The following figures require a choice to be made among the large number of images available. For objectivity, all images in a series and corresponding to the same parameters were observed. Usually we take 3 pictures for each position. The image which represents the most the two others was kept. Such a choice is sometimes difficult, especially when fluctuations are large from shot to shot. I have never intended to choose images to show a particular trend. The trends appeared when assembling the images.

Then, the intensity of the images were normalized separately. CCD camera used are very sensitive (65536 levels) and graphical representation is usually limited to 256 levels. Consequently, without separate normalization, many pictures would be uniform or saturated, which would reduce the interest of the analysis.

When no precision is given, experimental parameters remain unchanged (energy, pulse duration, focal length, electron density, interaction length). But series shown are not obtained during the same experiment. Due to a high sensitivity of the electron beam quality on the experimental setup, it's not impossible to have a slight mismatch between different series. However, all images for a figure belong to the same series.

2.3.1 Influence of the electron density

As observed on the spatial quality of the electron beam, the electron density is an important parameter of the interaction. Fig. 2.9 shows the evolution of spectra with gas density. The image analyzed previously is located in second position. At lower density, the spectrum remains quasi-monoenergetic but the charge contained in the peak has dropped by a factor 10. This rapid drop of the charge is also represented on Fig2.7 where the signal from the ICT and the scintillator are plotted.

At higher electron density $n_e = 7.5 - 10 \times 10^{18}$ cm^{-3}, one observes a transition where quasi-monoenergetic components merge with a maxwellian tail of low energy electrons. This transition happens when the plasma wavelength (10-12 μm) reaches the pulse length (9 μm). This density range can be considered in our experiments as the transition between the bubble regime and force or self-modulated laser wakefield (see Sec 1.4). The images on the right correspond to even higher electron density and they show only a maxwellian tail. This is a typical signature of the electron beam produced when the accelerating structure breaks. Electrons are accelerated at random energies and the divergence increases. The comparison of this figure with Fig. 2.3 shows that structures don't appear exactly in the same range of densities. These two figures originate from different experiments and the experimental conditions vary slightly between experiments.

One notes that the electron density where the spectral transition appears (i.e. $n_e = 6.0 \times 10^{18}$ cm^{-3}) corresponds also to the maximum charge on Fig. 2.7. In this region, fluctuations are large, because of the sensitivity of non-linear effects to initial parameters. Shot to shot fluctuations of the laser properties (energy, duration) are estimated to 10%, much less than variations observed experimentally.

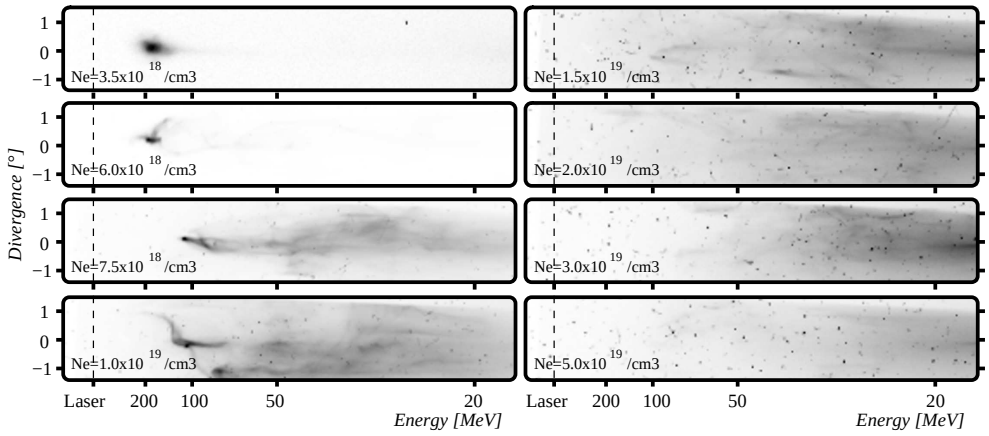

Figure 2.9: Electron spectra as function of the electron density. Transition from a quasi-monoenergetic peak to a maxwellian distribution as the electron density increases. Images are normalized independently.

Equivalent 3D PIC simulations were preformed for different electron densities and they reproduce the experimental trend (Malka et al., 2005b). The results are summarized on Fig. 2.10. A 30-fs long laser pulse containing 1 J is focused in a focal spot of diameter 21 μm (at half-maximum). Simulations were performed for a propagation over 2.5 mm for 3 different electron densities : 3, 6 and 12×10^{18} cm^{-3}. The spectrum at 6×10^{18} cm^{-3} corresponds to the one on fig Fig. 2.5 on a logarithmic scale. At lower density (3×10^{18} cm^{-3}), simulations shows that a quasi-monoenergetic beam forms at lower energy because the accelerating field of the plasma wave is weaker. After 2.5 mm of propagation, they reach 100 MeV, non-optimal energy, limited by the interaction length. On the opposite hand, in the simulation at high electron density (12×10^{18} cm^{-3}), a quasi-monoenergetic beam is formed early during the propagation, after 1 mm. Due to a shorter plasma wavelength, the dephasing length is reached earlier. Then, the spectral peak broadens towards a quasi-thermal maxwellian distribution. At the end of the simulation, the spectrum doesn't show the transient structure anymore.

2.3.2 Influence of the pulse duration

The distance between the gratings of the compressor is varied. This modifies both the laser pulse duration and its intensity. The energy remains constant. Fig. 2.11 shows that the signal quickly degrades and vanishes as we move away from optimal conditions. At 40 fs, the electron beam is more divergent and contains several peaks. It's probable that the accelerated electrons also interact with the laser which degrades the quality of the beam.

The reason why the signal vanishes is not obvious. It might come from a decrease in intensity or a longer pulse duration. The first option decreases the influence of non-linear phenomena such as self-focusing, which might hinders the generation of a strong amplitude plasma wave and might suppress the injection. The pulse duration has to be compared to the plasma period for this electron density, which equals 45 fs at ($n_e = 6.0 \times 10^{18}$ cm^{-3}). Consequently, the laser pulse duration remains similar to this period and the

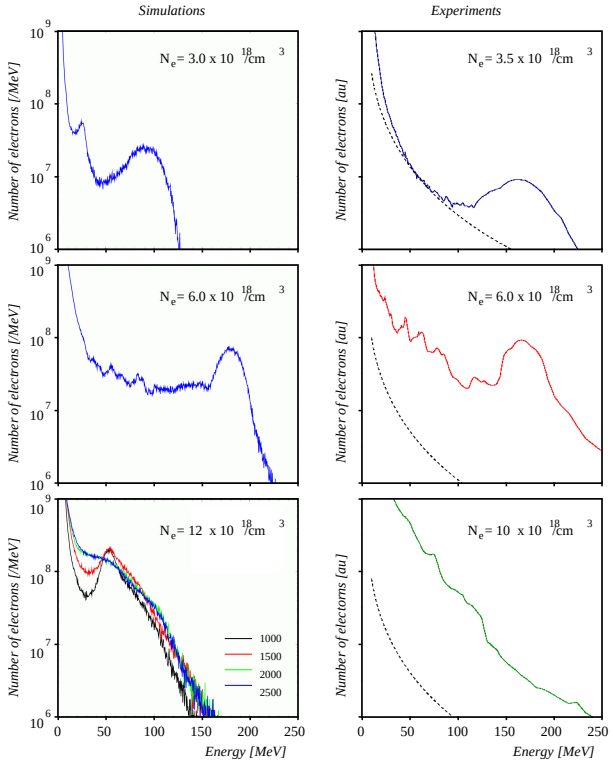

Figure 2.10: (Color) Comparison of electron spectra from experiments and simulations for several electron densities. The dashed line represents the detection limit.

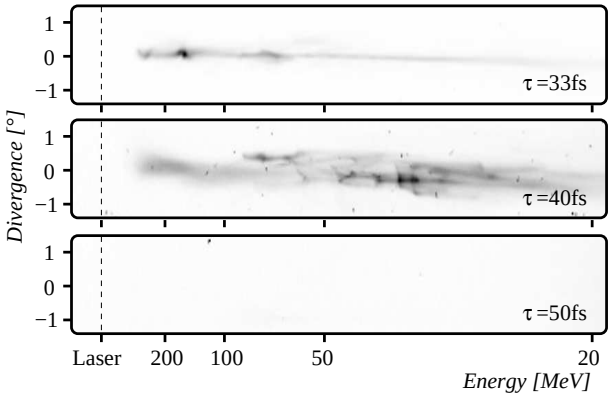

Figure 2.11: Electron spectra as function of the distance between the gratings. This modifies the pulse duration and its intensity. Images have been normalized independently.

main reason for this rapid evolution of the electron spectrum might be the decrease of the laser intensity : it reduces non-linear effects such as self-focusing, which may prevent the generation of a high amplitude plasma wave and may even suppress the injection. In order to confirm this point, the laser energy has been varied, while keeping the pulse duration constant.

2.3.3 Influence of laser energy

The laser energy is varied by shifting the delay between the pump pulse and the infrared pulse or simply by switching off pump lasers. This doesn't modify the laser focal spot because the 3rd stage is cryogenically cooled and the thermal lens remains constant. The pulse duration is now set to its optimal value again. Results are shown as function of laser energy and electron density on Fig. 2.12. The laser energy given on this figure corresponds to the value obtained after the 3rd amplification stage and before the compressor.

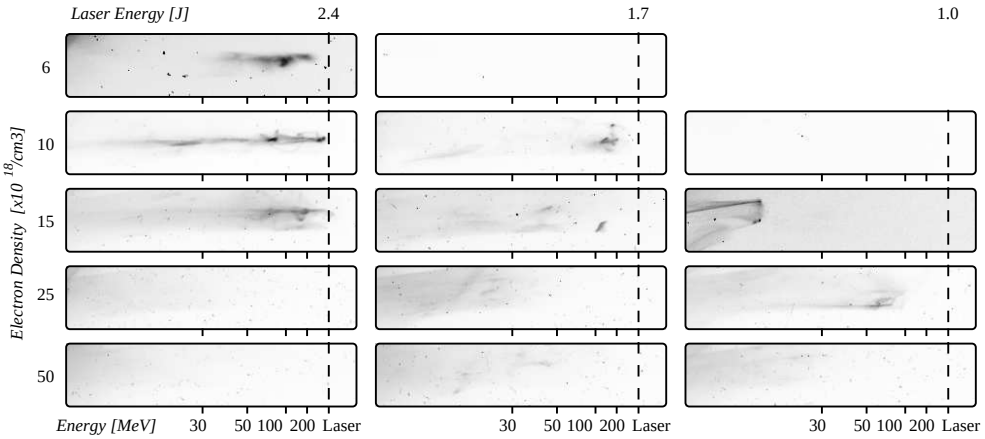

Figure 2.12: Electron spectra as function of laser energy and electron density. Images are normalized separately.

First important remark on this particular series : during this experiment, the fluctuations were larger than usually and sometimes the signal of the electron beam extends even on the opposite side of the laser axis! This axis is determined by the average position of the electron beam when there is no magnetic field. During this experiment, experimental conditions were less optimal than in previous experiments and shot to shot fluctuations were higher than usual. But the global trend explained hereafter still holds.

First, this picture confirms previous results : for a given electron density ($n_e = 6.0 \times 10^{18}$ cm^{-3}), on the first line, the signal vanishes fast as the laser energy is decreased. This testifies the importance of the non-linear effects in this interaction. Then, when decreasing the laser energy, electrons can be obtained again if the electron density is increased. This seizing result is due to the importance of the self-focusing effect in order to enhance laser intensity. The ratio of the laser power to the critical power for self-focusing P/P_c varies as $n_e I_0$ (see eq. 1.39) : when laser intensity decreases, the increase of the electron density allows to compensate and keep the self-focusing effect. However, even if electrons are observed again, their energy is weaker (for a constant electron density).

In the other direction (constant laser energy), the decrease of maximal electron energy as the electron density increases can be attributed to the variation of the dephasing length. As explained in chapter 1, the dephasing length corresponds to the estimation of the length over which electrons are both accelerated and focused. For the bi-dimensional linear theory, this length is

$$L_{deph}^{2D} \sim \gamma_p^2 \lambda_p / 2 \tag{2.1}$$

Numerical application
Hypothesis for this formula are not fulfilled (perturbed bi-dimensional case), but these linear expressions are useful experimentally to scale the experiment. Here is an estimation of the dephasing length. In our experimental conditions, the dephasing length is about $L_{deph}^{2D} \sim 1.9$ mm for an electron density of 6×10^{18} cm^{-3}, which is comparable to the diameter of the gas jet and the Raleigh length of the laser. This length drops to 0.5 mm for densities of 15×10^{18} cm^{-3}. This agrees with the vanishing of transient quasi-monoenergetic structures observed in numerical simulations presented in Sec. 2.3.1 after a short propagation distance.

2.3.4 Influence of the aperture of the focusing optics

According to studies carried out before I started my PhD, it seemed that parabolic mirrors of long focal length gave better results (in terms of spatial quality and energy of the electron beam). With this new spectrometer, it is interesting to check these previous studies. We have therefore used parabolic mirrors of different focal lengths $f = 100$ cm, 50 cm and 30 cm. Corresponding characteristics are shown in Table 2.1. In particular, the waist has to be compared to the plasma wavelength (14 μm).

Focal length [cm]	100	50	30
w_0 [μm]	18	9	6
a_0	1.3	2.6	4.4
Z_r [mm]	1.2	0.3	0.14

Table 2.1: Waist w_0, normalized vector potential a_0 and Rayleigh length Z_r associated to these focusing optics.

Figure 2.13 shows the electron spectra obtained for different parabolic mirrors and for similar electron densities. For each case, the signal has been optimized in focus and in electron density. Images shown on this figure were not obtained the same day because changing a parabolic mirror requires time to realign and optimize the signal. Consequently, the energy axis on the spectra differs for each parabolic mirror because of slight modifications to the setup (position of the spectrometer).

One notices that the maximum electron energy is lower for the 30-cm focal length. Focal lengths of 50 and 100 cm give spectra with similar properties. Clearly, the acceleration is less efficient when focusing hard and the divergence also increases. Precise reasons for this behaviour are currently being investigated. Various possibilities are being studied. First, there should have no preplasma, even when focusing hard, because no signature of a

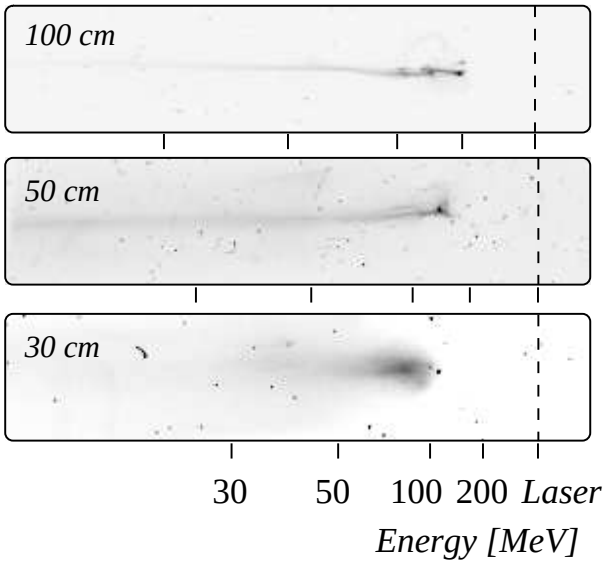

Figure 2.13: Evolution of the electron spectra an function of the focusing optics. Ticks on the energy scale are different for each image. The electron density is 5.0×10^{18} cm^{-3} for the 30 cm parabolic mirror and 6.0×10^{18} cm^{-3} for the two others. images are normalized independently and were not obtained the same day.

preplasma has even been observed on the shadowgraphy diagnostic, even for the 30 cm focal length. Consequently, all shots were done in similar electron density profile. Another possibility is the interaction length. In the linear case, a laser pulse shorter than the plasma wavelength can't remain self-focused because of an electron overdensity at the front of the plasma wave (Sprangle et al., 1990). studies are being carried out to determine if the acceleration could be restricted to a shorter distance for the 30 cm parabolic mirror, for which the acceleration would take place only in the gradient of the gas jet. Non-optimal interaction conditions for this parabola might be the origin of such difference in spectra.

Figure 2.14 shows the evolution of the spatial profile for 100 cm and 30 cm parabola as the electron density is varied. The second line reproduces images from figure 2.3. The electron beam is structured for the two parabola at 20×10^{18} cm^{-3}. Whereas the stability and the spatial quality improve towards lower electron density for the long focal length, the short one doesn't show any improvement.

2.4 Stability

When using the 50 cm focal length parabolic mirror from the previous section, we have studied the stability of the electron beam with and without magnetic field. Variations given here are standard deviations.

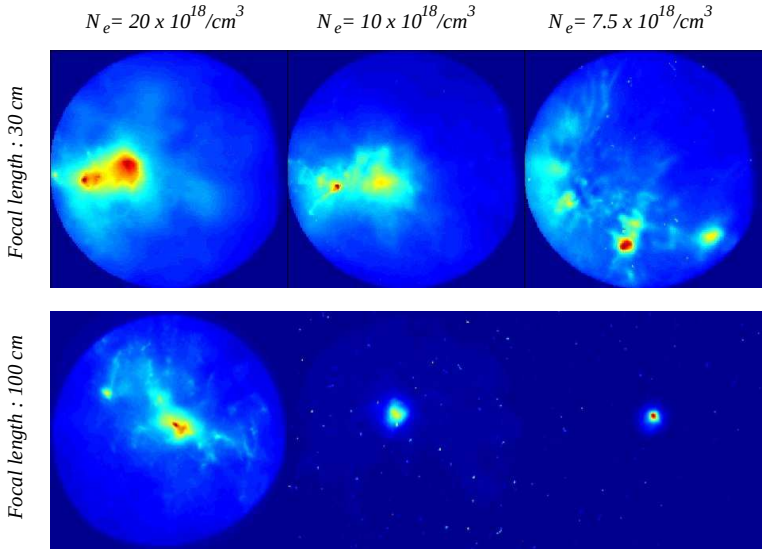

Figure 2.14: (Color) Transverse profile of the electron beam for the 30 cm parabolic mirror (top) and 100 cm parabolic mirror (bottom) as function of the electron density. The scintillator is placed perpendicular to the laser axis and magnets were removed. The color scale for each image is determined separately. These two series of shots were not performed the same day.

2.4.1 Beam pointing stability

For each experiment, a reference position on the scintillator without magnetic field had to be defined. We estimated the average position of the electron beam at low electron density, where the electron beam is more collimated and more stable. The fluctuations around this position allow to obtain the uncertainty on the energy spectrum. Here, the electron density is set to 3.0×10^{18} cm^{-3}.

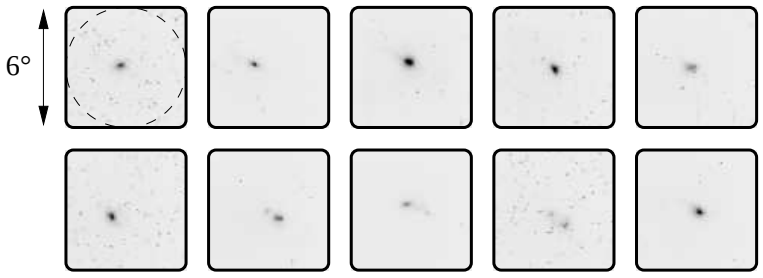

Figure 2.15: Beam pointing fluctuations on the scintillator for 10 successive shots without magnetic field. Images have been normalized to the same gray table.

These 10 images show the fluctuation in a window of 100 mrad. There is usually only a single narrow structure. The divergence of the beam defined as the full angle of the cone with aperture corresponding to the FWHM of the dose profile is 8 ± 3 mrad on average and fluctuates by 6 mrad from shot to shot (RMS). From these images, one can estimate the fluctuations of charge of the whole electron beam. For this low electron density, one obtains an average charge of 300 ± 130 pC (absolute calibration).

2.4.2 Spectral stability

When applying the magnetic field, measurements of the spectral stability was also performed. Fig. 2.16 represents 10 consecutive shots at the same electron density. Errorbars corresponding to the previous uncertainty from beam pointing fluctuations are represented on the first image. Despite a more intense signal located at high energy, these spectra can't be qualified as quasi-monoenergetic. The presence of a weak signal at low energy makes it maxwellian-like after deconvolution.

However, the beam is relatively stable. Sometimes, additional structures appear on the images on the right side of the picture. The charge contained in the intercepted spectral range (above 20 MeV) is also relatively stable 200 ± 80 pC. This value is lower than the charge obtained without magnetic field as expected.

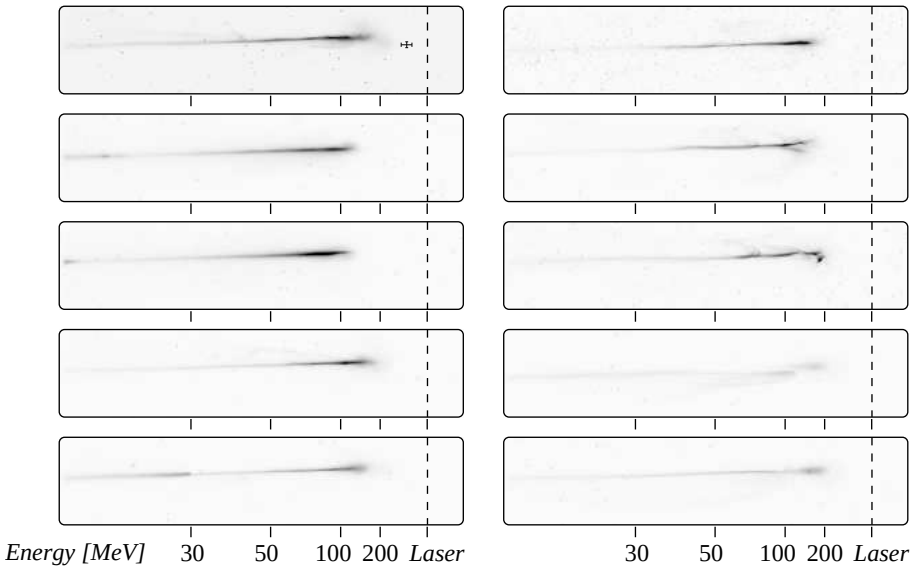

Figure 2.16: Fluctuations in the electron spectra for 10 consecutive shots in the same experimental conditions. Images have been normalized to the same color table.

In this chapter, a significant enhancement of the quality of the electron beam is reported : in optimal configuration, a quasi-monoenergetic electron beam with a low divergence has been measured. This has been achieved using a new kind of electron spectrometer, which gives a broadband single shot spectrum.

The various series presented introduce and illustrate some important parameters of the interaction : the dephasing length, the self-focusing of the laser pulse. It is also shown that quasi monoenergetic electron beams were obtained only in a narrow range of parameters. An increase of the electron density, a lengthening of the laser pulse duration or a decrease in the laser energy make the electron structures vanish. Estimation of the stability of the electron beam were also carried out. This work was performed at the best performances of the laser system, in transition area where fluctuations are still relatively large. Using more powerfull laser systems may allow to stabilize the beam above this threshold. This is also a reason why petawatt laser systems are growing all around the world.

Chapter 3

Structures of the electron beam and propagation of the laser

This section gathers experimental results concerning the fine structures of the electron beam and the laser beam properties after the interaction.

A correlation between the output angle of the electron with its energy has been observed. This was attributed to an off-axis injection of electrons and an oscillating motion around the laser axis upon propagation. The measurement of the transition radiation shows that the electron beam contains fine structures. Concerning the transmitted laser pulse properties, a temporal shortening has been measured. The transmitted laser energy also allows to estimate the energy dumped into the plasma waves. Thomson scattering diagnostic gives information on the propagation of the laser pulse in the plasma and interferometry diagnostic shows the free electron density in the plasma.

3.1 Oscillations in the spectrum

3.1.1 Experimental results

Observed on several electron spectra during the different experimental campaigns, particular correlation between the electron energy and the average electron ordinate have been recorded. These oscillations reveal a correlation between the output angle and the electron energy. A typical example is shown on Fig. 3.1. This image has been obtained at an electron density 6×10^{18} cm^{-3} for the 3 mm-diameter nozzle. What are the physical mechanisms responsible for such oscillations ? Among the different possible origins, one can think of the laser electric field, instabilities or betatron (synchrotron) oscillations of the electron beam centroid.

Following arguments allow a reduction of the physical scenarios : The instability of electron beam hosing (Whittum et al., 1991) refers to the resonant coupling between the electron beam centroid along the propagation axis with the walls of an ionic channel. This instability is damped for beams shorter than the plasma period (Krall and Joyce, 1994). This instability gives modulations at the plasma pulsation ω_{pe}. One should expect larger amplitudes at lower electron energy, ie in the tail of the electron beam. Actually, oscillations of the electron centroid is observed here for high electron energies and not for low energies.

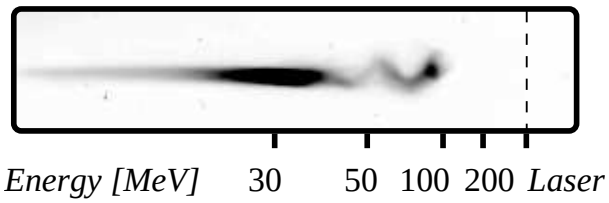

Figure 3.1: Example of electron spectrum showing oscillations of the average position of the electrons correlated to their energy. This image has been voluntarily saturated to show clearly the oscillations.

The laser hosing instability describes the coupling between a laser pulse and the driven plasma wave. Perturbations of the laser pulse modify the ponderomotive force, thus deforming the plasma wave which is no longer axi-symmetric. In return, this modified electron density profile acts on the tail of the laser pulse. This resonant coupling between perturbed laser pulse and the plasma wave has been observed experimentally (Kaluza et al., 2006) in experimental conditions close to ours. Nevertheless, we usually work at lower plasma density and the Thomson diagnostic has never shown significant oscillations. This effect is described in Ref. (Sprangle et al., 1994; Shvets and Wurtele, 1994) and these theories require an initial laser pulse perturbation (either a lateral shift from the axis of an ionic channel or a spatial chirp of the laser pulse centroid along the propagation axis). In our experimental conditions, the laser pulse length is shorter than the plasma wavelength, which damps this instability. Even in the case of a slight instable motion of the laser beam, the trapped electron would see the same perturbations of the electric field and the electron beam would experience a global deflection. This might be the origin of the electron beam pointing fluctuations for instance. This can't explain the several periods of modulation of the electron beam observed experimentally.

Apart the instabilities, if the electron overrun the laser pulse, they will be scattered by the electric field. This would mainly involve high energy electrons, i.e. those in front of the bunch. However, the laser pulse polarization is perpendicular to the axis of oscillation observed experimentally. The laser electric field doesn't seem to be responsible for this effect. Corrections that might arise when the paraxial approximation fails are still very weak, because the first order correction to the electric field is along the propagation axis (Quesnel and Mora, 1998). The correction along the axis of oscillations is of second order in $\varepsilon = 1/(k_0 w_0) \sim 7 \times 10^{-3}$ for $w_0 = 18\ \mu$m, which is negligible. Then, Faraday rotation of the laser polarization in the plasma is weak in underdense plasma. Finally, if one assumes that these effects might explain the observed the oscillations, then the electric field along the polarization axis would be significantly more intense and would totally disrupt the electron beam. This is not observed experimentally because the electron beam also remains collimated along the horizontal axis. The most accurate interpretation seems to be betatron oscillations, which is described in the following.

When the electron is not on the revolution axis of an ionic channel, a radial restoring force make it oscillate around this axis during propagation (Esarey et al., 2002). For a relativistic particle with a constant Lorentz factor, the oscillation period in a uniform

ionic channel is obtained by solving the equation of motion.

$$\frac{\partial}{\partial t}\gamma m\vec{v} = -\frac{m\omega_{pe}^2}{2}r\vec{e}_r \tag{3.1}$$

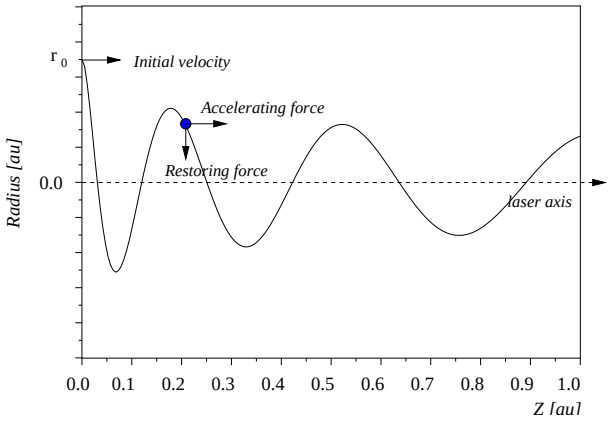

Figure 3.2: Betatron oscillations in a plasma channel for different electron energies. Their output angle depends on their energy.

A projection along the radial direction gives the equation of an oscillator at the betatron frequency $\omega_\beta = \omega_{pe}/\sqrt{2\gamma}$. This frequency depends on the electron energy and therefore, for identical injection conditions (identical radius $\vec{r}_0$, velocity $\vec{v}_0$), the electron leaves the interaction area with an output angle depending on their energy (see Fig. 3.2).

The ponderomotive force of the laser excites a plasma wave in its wake, where the radial restoring force is linear as in the case of the ionic channel. But this model doesn't describe the simultaneous acceleration of the electron by the longitudinal electric field from the wave. I have solved the equations of motion including a constant accelerating field E_z (see Appendix A. Let's write β_0 the initial normalized velocity (to c) and γ_0 the initial relativistic Lorentz factor, β and γ the same quantities at the end of the interaction and $E_0 = m_e c\omega_{pe}/e$. The electron is assumed to be injected at radius r_0 and their initial velocity is parallel to the propagation axis. In the paraxial approximation and assuming that $\sqrt{2\gamma_0\beta_0}E_0/E_z \gg 1$ (verified *a posteriori*), the output angle is written :

$$\theta_{E_z}(\gamma) = -\frac{\omega_{pe}}{2c}r_0\frac{(\gamma_0\beta_0)^{1/4}}{(\gamma\beta)^{3/4}}\sin\left[\frac{E_0}{E_z}\left(\sqrt{2\gamma\beta}-\sqrt{2\gamma_0\beta_0}\right)\right] \tag{3.2}$$

From the experimental image (Fig. 3.1), one obtains the correspondence between the final electron energy and the output angle. This curve is plotted on Fig. 3.3. Recent studies (Lu et al., 2006b) allow to reduce further the number of unknown parameters. The authors give the injection energy in the accelerating structure. The injection takes place at the back of the cavity when the particle velocity equals the plasma wave phase velocity. Taking into account the front edge erosion of the laser pulse, this leads to a reduced phase velocity and finally the following injection energy :

$$\gamma_0 = \frac{1}{\sqrt{3}}\frac{\omega_0}{\omega_p} \sim 10 \tag{3.3}$$

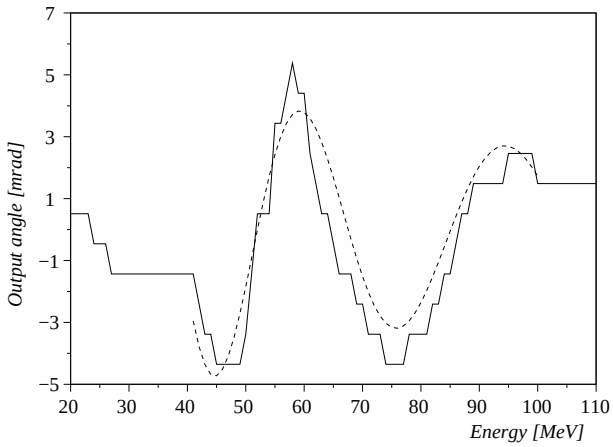

Figure 3.3: Optimization of the parameters from Eq. 3.2 to the experimental data with $r_0 = 0.35\mu$m, $E_0/E_z = 1.6$. (solid line) experimental curve from Fig. 3.1, (dashed line) optimization.

Setting the value of this parameter mainly sets the phase of the sinusoid in Eq. 3.2. The accelerating electric field and the radius of injection still need to be determined. They influence respectively the frequency of the oscillations and their amplitude in this equation. Optimization by the method of least squares gives the curve represented in dashed line on Fig. 3.3. The optimized parameters correspond to a radius of injection $r_0 = 0.35$ *mu*m and an accelerating field $E_z = 150$ GV/m. These parameters seems coherent with the values expected for this mechanism. Indeed, one thinks of a radius smaller than the wavelength plasma (14 *mu*m) and an accelerating field which allows to reach the maximum energy measured in experiments (100 MeV) in 3 mm of interaction.

The assumptions of this model are strong. It is simply used to illustrate the interpretation suggested. In reality, the interaction is more complex : the electric field might not be the same one for all the electrons because of the screening of the accelerating potential of the wave plasma by the other injected electrons (saturation). The radius of injection can also move during the propagation, possibly because of instabilities mentioned above. But the essential question which remains is “Why on this particular shot, was the injection off-axis?”. It is possible that an initial asymmetry in the laser leads to an asymmetry of the wave plasma and thus off-axis injection.

Similar images were obtained but only under the same experimental conditions. This comes from the fact that the electron beam is collimated and contains a high load only in a restricted range of parameters.

3.1.2 Propagation of an asymmetric laser pulse

Simulations were carried out by our colleagues from GoLP in Portugal for an initial asymmetric laser profile. To our knowledge, these are the first 3D PIC simulations carried out for a nonideal laser pulse. These results are still at a preliminary stage but make it already possible to highlight the experimental mechanism involved. In order to minimize the computing time, the parameters of simulation do not reproduce the experimental conditions: a laser pulse of duration 33 fs (FWHM), of energy 5 J centered to 800 nm is propagated

in a plasma of uniform initial electron density $n_e = 7.7\ times 10^{18}$ cm^{-3}.

Usually, theorists take Gaussian profiles spatially and temporally corresponding to the fundamental mode of propagation in the paraxial approximation. The figure 3.4 shows the transverse profile of intensity initial of the laser pulse voluntarily set to be asymmetric. The radius at $1/e^2$ of the intensity equals 7 and 12 μm respectively for positive and negative directions on both axes. The corresponding ponderomotive potential a_0 reaches a maximum of 6.5. For such intensity, the injection occurs immediately as the laser enter the plasma, which allows the direct relation between the laser profile and the electrons, while skipping the self-focusing section. The simulations is done in a volume of $48 \times 95 \times 95\,\mu$m^3 divided in $1874 \times 248 \times 248$ cells. Each cell contains initially 2 particles. The laser propagates along x_1 and is polarized along x_3.

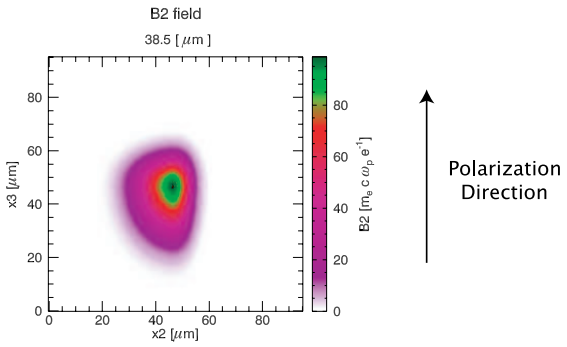

Figure 3.4: (Color) Initial asymmetric laser intensity profile.

Because of this initial laser intensity profile, the ponderomotive force is unbalanced during the propagation of the laser in the plasma, which leads also to an asymmetric plasma wave. In the end, one notes an injection shifted from the laser axis on Fig. 3.5. These images correspond to the electron density profiles in the plane of polarization of the laser and in the perpendicular plane, containing the axis of propagation.

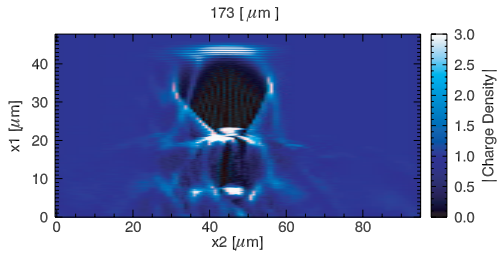

Figure 3.5: (Color) Electron density profile after 190 μm of propagation. The laser propagates from bottom to top. The snaphot was taken in the plane containing the laser axis and the transverse axis perpendicular to the plane of polarization.

According to the simulations, the duration of injection is short relative to the period of motion at the back of the cavity. This helps to confirm the hypothesis of the model described above (see Appendix A) : electrons are injected at the same radius and perform betatron oscillations during their propagation.

In order to simulate more particle, this simulation is reproduced in 2D geometry. This new simulation represents a volume of $83 \times 166\ \mu m^2$, composed of 3274×500 cells, each containing 81 particles initially. The plasma period is adapted to this 2D geometry and equals $\omega_0/\omega_{pe} = 13$ and the normalized vector potential reaches 3. The laser is polarized in the plane perpendicular to the simulation. Finally, one obtains an asymmetric shape of the plasma wave and an injection shifted on figure 3.6a. The angular distribution as function of the electron energy appears clearly on figure 3.6b after a propagation of 0.8 mm.

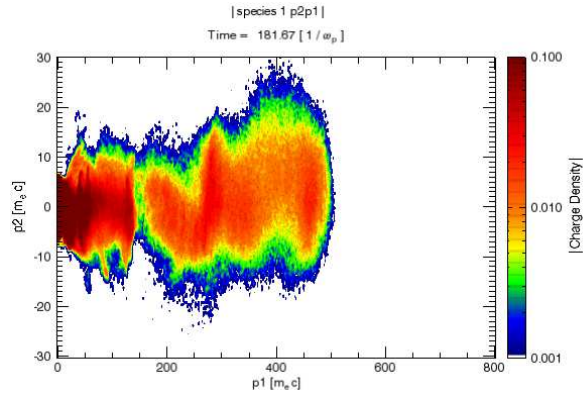

Figure 3.6: (Color) 2D PIC simulation : (a) Electron density after a propagation length of 0.8 mm, (b) angular dependence of the electron distribution with energy.

This study shows that an initial asymmetric laser pulse can lead to an asymmetric plasma wave. The energy-angle correlation observed experimentally has been reproduced, which validates the scenario. These studies on non-ideal interaction conditions are unique and emphasize the dependence of the interaction on the laser pulse fluctuations, inherent to experimental studies.

3.2 Transition radiation

Fine structures of the electron beam have also been observed in a different way. We focus here on the transition radiation emitted by a relativistic electron beam at a metal-vacuum boundary (Ginzburg and Frank, 1946; Goldsmith and Jelley, 1959). This technique is commonly used in particle accelerators to measure the electron beam properties such as electron energy and angular distribution (Wartski et al., 1975), the source size and the bunch shape (Shibata *et al.*, 1992), the duration (Kung et al., 1994) or the period of microbunching (Tremaine *et al.*, 1998). Because this is a surface effect, the thickness of this diagnostic can be very thin, which limits the scattering of the electrons, explaining the popularity of such a detector.

3.2.1 Angular and spatial distribution of the OTR

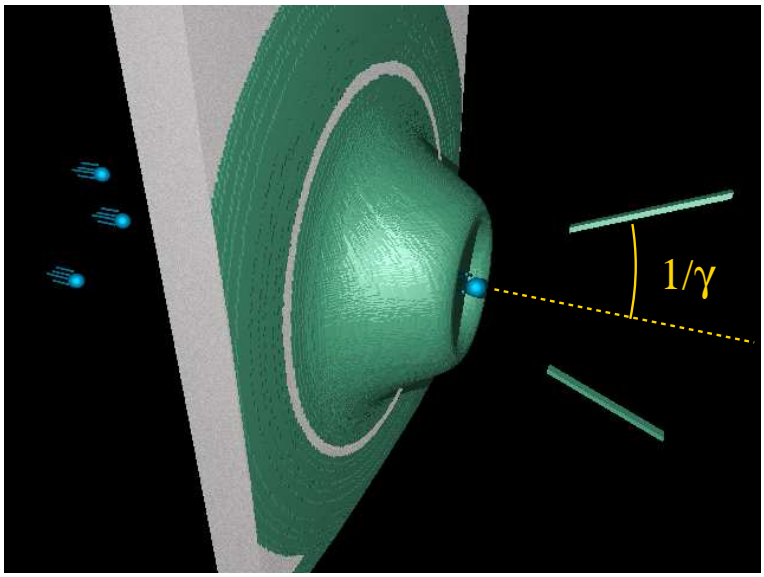

Figure 3.7: Transition radiation generated at an interface by an electron. The green area represents the amplitude of the propagating electric field generated at the interface. The divergence of this radiation evolves as $1/\gamma$, where γ is the relativistic factor of the particle.

In the visible range, this transition radiation is named Optical Transition Radiation (OTR). When an electron crosses a boundary, an electromagnetic wave is emitted (see Fig. 3.7). The global contribution from all electrons accelerated during the interaction reveals the structures of the electron beam. First, here is a summary of the analytical formulas from two theories giving the angular and the spatial distribution of the electric field generated at an interface.

Angular distribution

For a relativistic electron, analytical formulas give the OTR radiation emitted as a function of the azimuthal angle of observation θ and the properties of the electron at the interface (incidence angle ψ, distance to origin ρ, polar angle ϕ of the projection of the velocity vector on the radiator plane and the normalized momentum $u = \gamma\beta$) (Ter-Mikaelian, 1972; Schroeder et al., 2004). The geometry is represented in Fig. 3.8. The interface is placed at $z = 0$. The normalized electric field is projected along two perpendicular axes $\vec{E}^{(Sch)} = E_{\parallel}\vec{e}_{\parallel} + E_{\perp}\vec{e}_{\perp}$. The unitary vector $\vec{e}_{\parallel}$ is in the plane (x, O, z) and the vector $\vec{e}_{\perp}$ is collinear to (Oy). The normalized components of the electric field are :

$$\begin{cases} E_{\parallel} = \dfrac{u\cos\psi[u\sin\psi\cos\phi - \sqrt{1+u^2}\sin\theta]}{[\sqrt{1+u^2} - u\sin\psi\cos\phi\sin\theta]^2 - [u\cos\psi\cos\theta]^2} \\ E_{\perp} = \dfrac{u^2\cos\psi\sin\psi\sin\phi\cos\theta}{[\sqrt{1+u^2} - u\sin\psi\cos\phi\sin\theta]^2 - [u\cos\psi\cos\theta]^2} \end{cases} \tag{3.4}$$

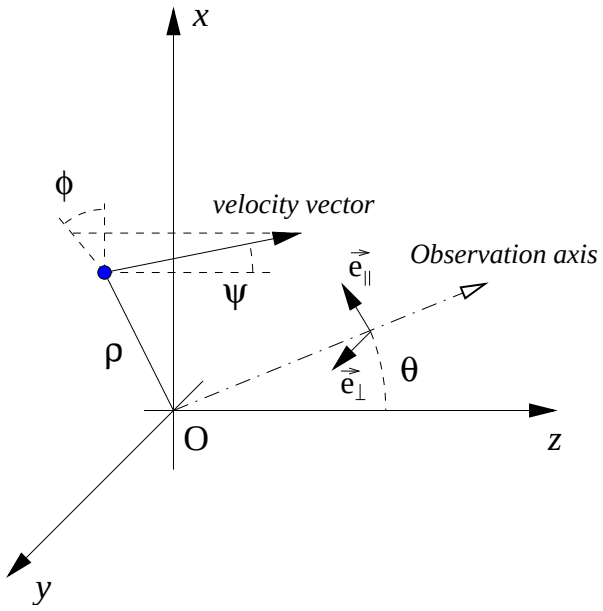

Figure 3.8: Definition of parameters for the angular distribution of the electric field. The blue point shows the impact position of the electron trajectory with the radiator plane placed at (x, O, y).

These formulas assume the interface is between a perfect conductor and vacuum. This theory allows to account for the angle of incidence of the electron. For an electron perpendicular to the radiator $\psi = 0$, the electric field reduces to a much simpler form, which exhibits the $1/\gamma$ trend of the divergence :

$$\left\| \vec{E}^{(Sch)}(\theta) \right\|^2 = \frac{\beta^2 \sin^2\theta}{(1-\beta^2\cos^2\theta)^2} \tag{3.5}$$

Spatial distribution

Other studies have lead to the spatial electric field distribution from an electron impinging at normal incidence on the radiator (Castellano and Verzilov, 1998). This theory is based on a pseudo-photon description of the electron. The total contribution from the electron and the field reflected by a perfect conductor gives the electric field which establishes. The origin of the coordinates is the intersection point between the electron and the radiator. The expression of the normalized electric field is expressed as function of the cylindrical coordinates : z the distance to the radiator, ρ the distance from the projection to the origin and ϕ the corresponding polar angle (which doesn't appear). The radiation is polarized radially (along $\vec{e_r}$). The geometry is shown on Fig. 3.9. The normalized electric field is written :

$$\vec{E}^{(Ca)}(\rho, z) = \int_0^\infty \frac{t^2}{t^2 + (\beta\gamma)^{-2}} e^{-ikz\sqrt{1-t^2}} J_1(k\rho t)\, dt\, \vec{e_r} \tag{3.6}$$

where k is the wave vector of the radiation observed and J_1 is the Bessel function of the first kind. As the authors underline, the argument in the exponential function,

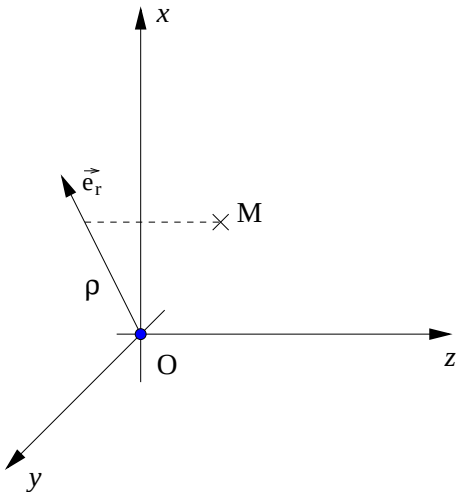

Figure 3.9: Definition of parameters for the spatial distribution of the electric field. The blue point shows the impact position of the electron trajectory with the radiator plane placed at (x, O, y).

involving the propagation distance, shows that propagating modes correspond to $t > 1$. Other modes correspond to a quasi-static field which established at the surface of the radiator. The integral can be split into a quasi-static term $\int_0^1$ and a propagating term $\int_1^\infty$ which corresponds to the emitted radiation. In the following, only the later term is computed. Figure 3.10 shows the radial evolution of the amplitude of the electric field for $\gamma = 200$.

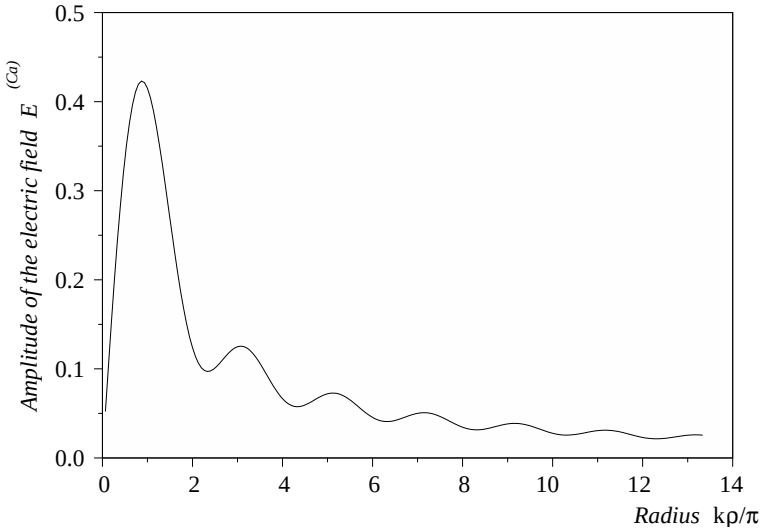

Figure 3.10: Amplitude of the electric field from Eq. 3.6 as function of the radius for $\gamma = 200$.

Calculation of phase

For an electron distribution, the individual contribution of each electron to the electric field contains a phase. This phase includes two terms (see Fig. 3.11) : a delay from the propagation of the electron up to the radiator δt_e, another delay taking into account the angle of observation of the radiation emitted δt_r. The total delay is $\delta t = \delta t_e + \delta t_r$ and the phase to be introduced in the electric field is $\exp(-i\omega\delta t)$ where ω is the pulsation of the radiation. In the case of the spatial distribution of the radiation, the calculation is performed at the surface of the radiator and the second delay is zero $\delta t_r = 0$.

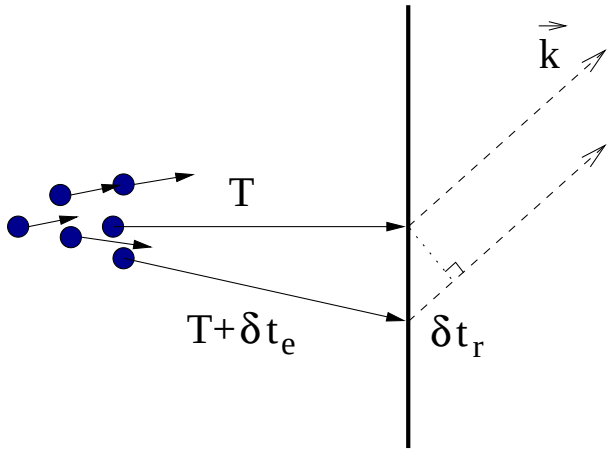

Figure 3.11: Illustration of the phase from the propagation of the electrons (δt_e) and from the emission of radiation (δt_r).

Here is an analytical example to understand the principle of the measurement. One assumes an point-like source of electrons with identical properties (energy, momentum). This beam is characterized by its temporal distribution $f(t)$. The electrons cross the radiator perpendicular to their direction of propagation. Under these assumptions, the individual amplitude of the electric field $\vec{E}(\theta)$ emitted by each electron is identical. The dephasing term depends only on their time of arrival on the radiator, i.e. on the temporal distribution $f(t)$.

If one computes the angular distribution of the radiation at pulsation ω, one integrates the contribution of all the electrons

$$\vec{E}_{tot}(\theta) = \sum_{k=1}^{N} \vec{E}(\theta)\exp(-i\,\omega\,\delta t(k)) \tag{3.7}$$

where $\delta t(k)$ is the delay for electron k to the interface. This can be rewritten using the distribution function $f(t)$ from the source

$$\vec{E}_{tot}(\theta) \propto \vec{E}(\theta)\int f(t)\exp(-i\omega t)dt = \vec{E}(\theta)\mathrm{TF}(f)(\omega) \tag{3.8}$$

The intensity on the detector after integration over the angles of observation becomes

$$I(\omega) \propto \int \left\|\vec{E}(\theta)\mathrm{TF}(f)(\omega)\right\|^2 2\pi\sin(\theta)d\theta \equiv I_0 \mid \mathrm{TF}(f)(\omega) \mid^2 \tag{3.9}$$

The electric field given in Eq. 3.5 is independent of the pulsation. This relation shows that the signal measured on the spectrometer depends on the Fourier transform of the distribution of the electrons. If structures exits in the electron beam, they will appear in the spectrum at corresponding wavelengths.

This simplified case illustrates the correspondence between the structures of the electron beam and the spectrum of the radiation emitted. In reality, the phase term is more complex and the signal can't be estimated using only a Fourier transform. A numerical simulation allow to compute the radiation for more complex electron distributions. This is detailled in section 3.2.4.

3.2.2 Experimental setup

In order to study the forward coherent radiation emitted by the electron beam, a 100 μm-thick aluminum foil has been added to the previous setup. It is called the radiator and was placed at several distances along the electron path to see the loss of coherence of the radiation emitted by the electron beam. This thickness of aluminium prevents the ASE from the laser from drilling a hole in the foil before the main pulse arrives, also in order to protect diagnostics placed behind. A lens with focal length 300 mm and collection angle 4° (width) images the surface of the radiator onto a CCD camera. Using a glass window, the simultaneous measurement of the spectrum in the visible range is performed on an imaging spectrometer containing a grating with 150 lines/mm. The experimental setup is shown on figure 3.12

The spectral range is limited to 400-850 nm because of a drop in sensitivity outside. Among all the shots, only few can be analysed because of the fluctuations in the signal intensity. The measured spectra are corrected for the instrumental spectral response of the detection system. The calibration was done using a white lamp (Oriel model 63355) with known spectrum, lend by LULI.

3.2.3 Imaging diagnostic

Fig. 3.13 shows the images obtained when varying the distance betwen the interaction point and the radiator. One notices that fluctuations at position 140 mm are large and correspond to shot to shot variations of ± 10 mrad as usually observed on the scintillator screen. As the radiator is moved further away, the size of the OTR signal almost doesn't change (of the order of 200 μm). The emission remains intense on an area which doesn't vary proportionally to the distance. One observes only a fraction of the electron distribution, for which the structures in the electron beam persist upon propagation and for which the emission remains partially coherent.

The decrease in the emitted energy as function of the distance to the radiator is shown on Fig. 3.14. The energy has been obtained using the absolute calibration of the detection system (CCD camera and neutral density filters) in the range 400-1000 nm. For a given position, one notices large fluctuations of the signal. The signal drops by several orders of magnitude with distance. This comes from a progressive damping of the structures of the beam during propagation because of the distribution of longitudinal and transverse momenta. For an incoherent emission, the energy level would remain constant, independent of the position of the radiator (because the collection angle is kept constant).

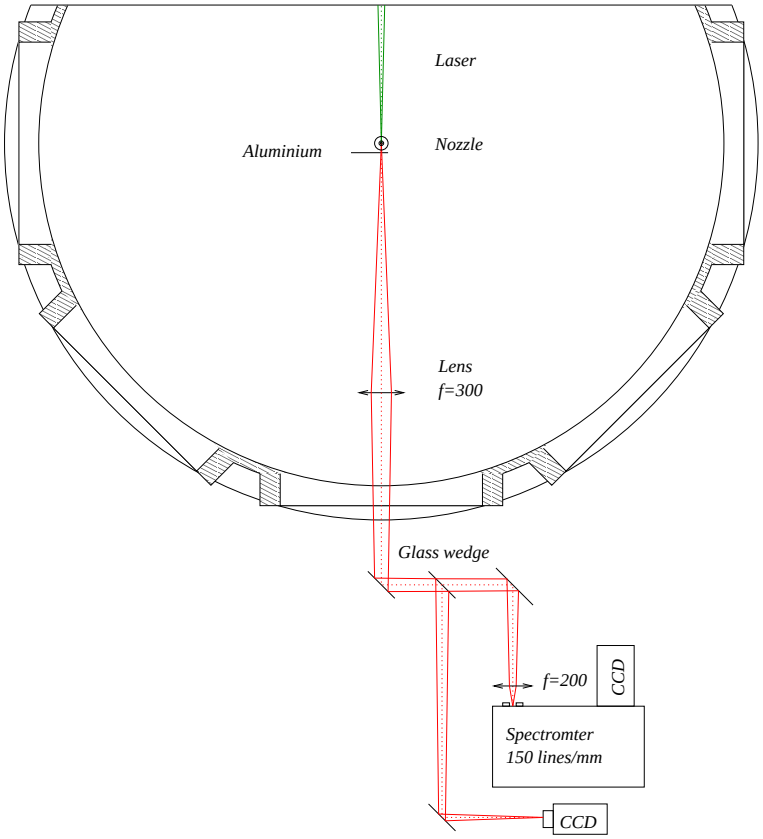

Figure 3.12: (Color) Experimental setup for the measurement of the OTR spectrum and the image of the radiator.

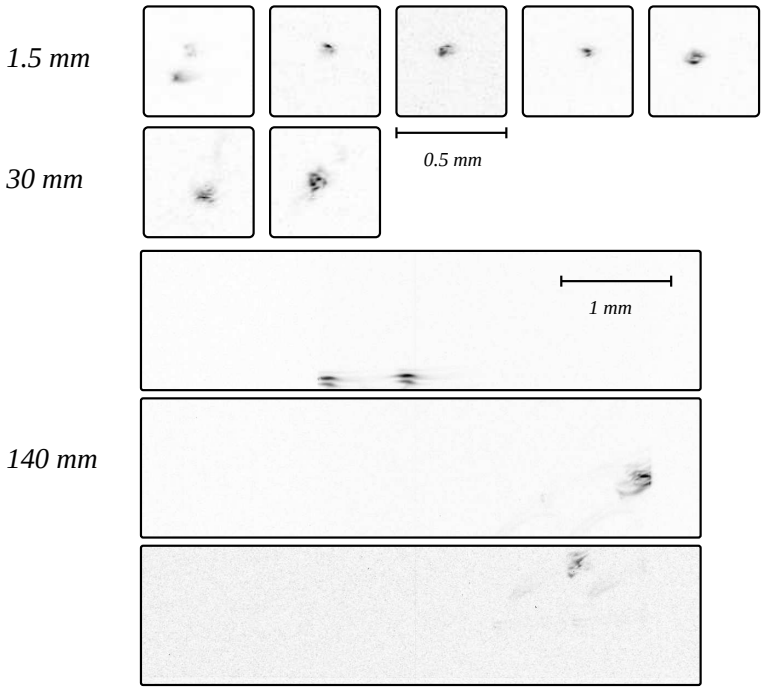

Figure 3.13: Example of images of the radiation emitted at the surface of the radiator for several distances between the source and the radiator. The 3 images at 140 mm have a magnification factor twice lower. The echo on the left is the back reflexion on the glass window used for the imaging diagnostic. Images have been normalized independently.

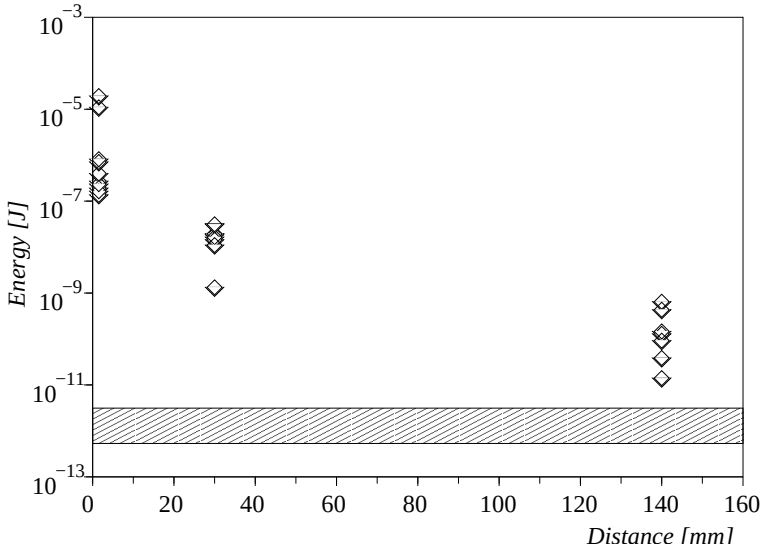

Figure 3.14: Evolution of the OTR energy in the range 0.4-1.0 μm with distance of the radiator, estimated using the absolute calibration. The hatched area corresponds to signal calculated for an incoherent emission using separate electron spectrum measurement.

Here is an estimation of the signal which would have been obtained for an incoherent emission of the OTR radiation. Knowing the angular and spectral distribution of the radiation (Eq 3.4), the collection angle and the spectral response of the CCD, it is possible to compute the number of counts measured for one electron. Experimental electron spectra acquired separately during this experiment were used to retrieve the spectral distribution. The level of signal obtained is shown in the cross-hatched area and is well below the experimental signal whatever the distance. In particular, for a distance of 1.5 mm, the measured signal is 5 orders of magnitude above the incoherent level. The emission is therefore partially coherent, which confirms that information can be obtained on the relative delay between electrons from the distribution (or at least from the fraction of the electron distribution which contributes efficiently to this intense radiation).

3.2.4 Spectral analysis

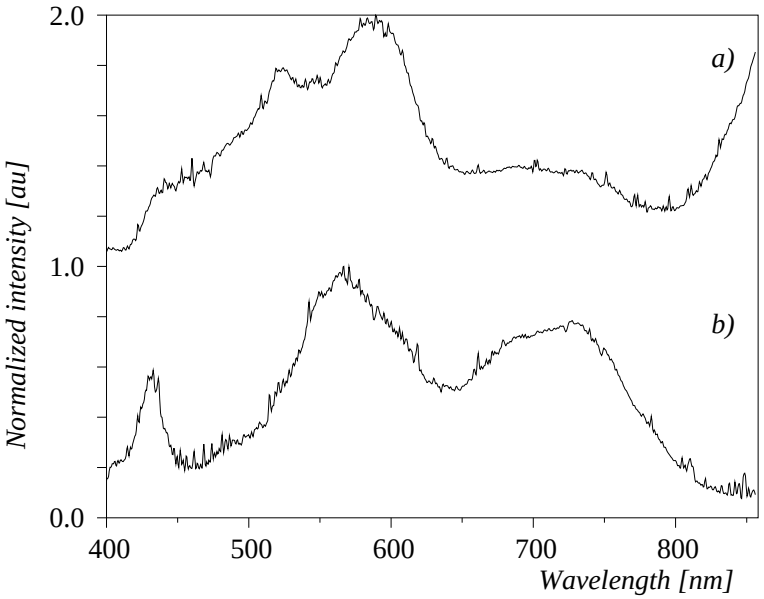

Figure 3.15: Examples of OTR spectrum measured experimentally for a radiator placed at 30 mm, after deconvolution of the instrumental response. The electron density was set to 5.0×10^{18} cm^{-3}. An iris was used with a collection angle (half-width) of a) 3 mrad and b) 8 mrad.

Fig. 3.15 shows two electron spectra obtained after deconvolution of the spectral response of the detection system. For these shots an iris was limiting the collected radiation and the half-angle of collection was respectively 3 and 8 mrad for spectra a) and b). The use of an iris is equivalent to the selection of the radiation from the most energetic electrons. The OTR spectrum is peaked a several wavelengths (430, 570, 590 and 740 nm) and its shape evolves from shot to shot. These spectral peaks reveals electron beam structures at the same wavelength. It has been verified that without gas, no signal was recorded in this range. The physical explanation to this emission is a possible overlapping of the electron beam with the back of the laser radiation in the accelerating cavity. The interaction

of electrons with the laser field has also been published recently when recording the evolution of the ellipticity of the electron beam with the polarisation of the laser (Mangles *et al.*, 2006).

One notes that the wavelength of the peaks differs from the central laser wavelength (810 nm usually). Actually, the laser spectrum is modified during propagation and especially relativistic self-phase modulation and plasma waves lead to a blue shift inside the cavity. It is shown is section 3.3.3 that these effects lead to a blue shift at the back of the laser pulse, where the electrons are. Consequently, it is not surprising that the electron beam is modulated at a wavelength which differs from the central wavelength of the laser.

In order to justify these experimental observations, the OTR spectrum emitted by an electron distribution from PIC simulation at an interface has been computed (using Eqs. 3.4 and 3.6). The electron distribution used comes from the simulation described in Ref. (Faure et al., 2004) with similar experimental conditions. Fig. 3.16 shows the electron beam structure in the plane of polarization of the laser. The amplitude of the oscillations increases as the electron beam overlaps with the laser field, justifying the interpretation of the modulations from the laser electric field. In the simulations, the electron distribution is modulated by a blue-shifted laser field.

The number of electrons is limited to 150000, to limit the computation time. Only electrons with energy above 100 MeV were used. In order to simplify the propagation, Coulomb repulsions were neglected. The electrons propagate along a straight line up to the radiator placed at position $z = 100$ μm. Electrons arrive at different time and the radiation is emitted at different places on the radiator. The electric field emitted by each electron is then computed by taking into account these delays in the emission.

This distance doesn't match the experimental conditions, but this helps to illustrate the emitted spectrum from a modulated electron beam. The large number of electrons in the experiment allow the observation of coherent radiation for larger distances. In the simulation, the signal vanishes quickly due to a lower number of electrons.

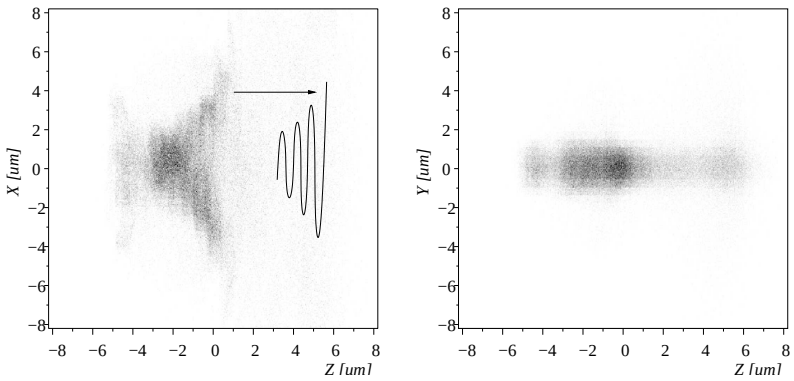

Figure 3.16: Electron density profile from the PIC simulation : (left) in the plane of polarization, (right) perpendicular to that plane.The electrons propagate from left to right. There is a structure in the electron density responsible for the coherent emission observed experimentally. This structure is reproduced to the right with a solid line.

Fig. 3.17 shows OTR signal emitted by the electron beam for the two methods. The

spectrum is peaked at 600 nm, corresponding to the wavelength of the electron beam modulations and this matches the experimental observations. The shape of the spectrum slightly differs between the different methods, which mainly comes from different hypothesis of each theory. Eq. 3.6 assumes that the electron incidence angle is perpendicular to the radiator. One also notices the second harmonic around 300 nm in the simulations. Experimentally, the sensitivity of the CCD camera didn't allow the observation of the second harmonic.

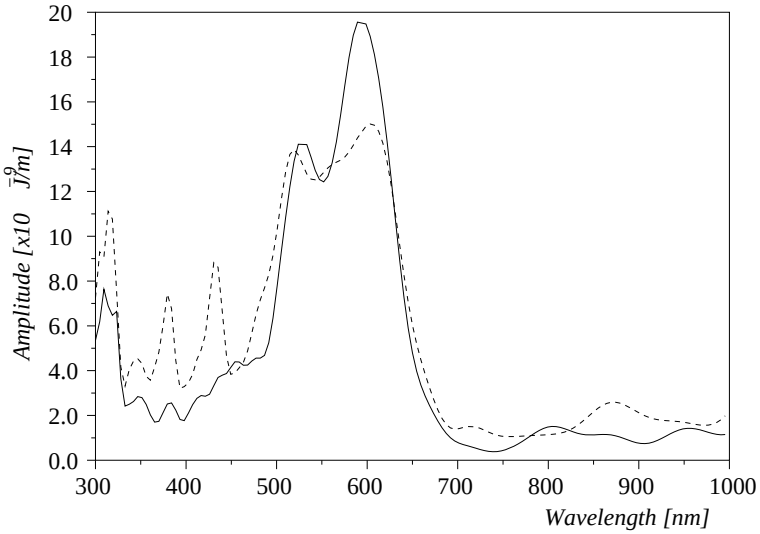

Figure 3.17: OTR spectrum after a propagation over 100 μm, simulated with an electron distribution from a PIC simulation, either using Eq. 3.4 (solid line) or Eq. 3.6 (dashed line).

3.2.5 Oscillations in the OTR spectrum

Now the radiator is placed at 1.5 mm. For this particular position, we have observed several times spectral modulations (see Fig. 3.18). This looks like interference pattern between two successive coherent sources. The analysis of spectral interferences is commonly used to measure the bunch separation in micro-bunched electron beams. Two coherent sources delyed by τ give an intensity $I(\omega)$ on the detector which oscillates with pulsation :

$$I(\omega) \propto \langle \mid E(\omega)e^{i\omega t} + E(\omega)e^{i\omega(t+\tau)} \mid^2 \rangle_t \tag{3.10}$$

$$\propto 2 \mid E(\omega) \mid^2 \cos^2(\omega\tau/2) \tag{3.11}$$

From the experimental data, the delay is estimated to $\tau = 74$ fs. Let's consider first the propagation effects : (i) if the average energy of the first electron bunch is higher than that of the second bunch, the separation between the two electron bunches will increase upon propagation to the radiator. (ii) If two electron bunches with the same kinetic energy don't have the same trajectory, they would reach the radiator at different times. Here are two numerical applications for realistic parameters of the interaction.

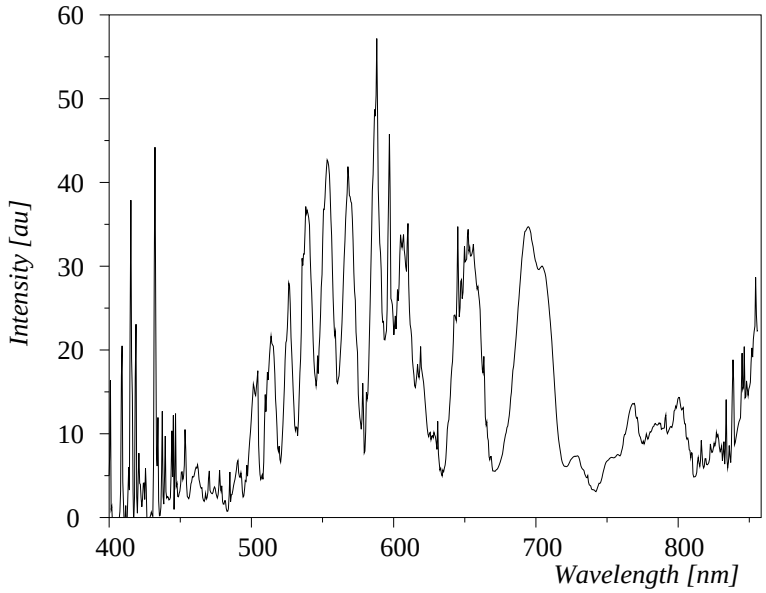

Figure 3.18: OTR spectrum showing modulations. Signal below 450 nm contains only noise : the sharp peaks come from X-rays that directly hit the CCD camera.

Numerical application

Let assume two electron bunches with identical direction of propagation. Let $\gamma_1 = 40$ and $\gamma_2 = 200$ be their relativistic factor. The delay on the radiator placed at position $L = 1.5$ mm is $\delta t_e \sim (1/\gamma_1^2 - 1/\gamma_2^2)L/(2c) = 1.5$ fs.

Consider now two electron bunches with the same kinetic energy propagating in different directions. The first one is oriented along the laser axis and crosses the radiator perpendicularly to the radiator. The second one makes an angle of $\alpha = 10$ mrad with this axis. This angle allows to observe interferences in the radiation emitted because the distance which separates the two electron beams on the radiator equals 15 μm, which is smaller than the OTR source size, usually estimated to $\gamma\lambda \sim 120$ μm for a 100 MeV-electron emitting at 600 nm. The delay which separates the two bunches on the radiator is $\delta t_e = (1/\cos(\alpha) - 1)L/c = 0.25$ fs.

Both geometrical effects are two weak to explain such a delay. Therefore, the two electrons beams are expected to have an initial separation and to originate from two different (successive) plasma wave buckets. Several electron bunches were already recorded on the same shot using scintillator screens. In that case, one would expect a delay corresponding to the plasma period. In the linear case, this one equals $\tau = 50$ fs for an electron density of ($n_e = 5.0 \times 10^{18}$ cm^{-3}), which is slightly lower than the observed delay. But in such non-linear interaction, the plasma period might be longer than the linear case due to the relativistic factor of the electrons. The geometrical effects described before may also account for a small additional delay.

Numerical application

The non-linear plasma period is written $\tau_p^{NL} = \sqrt{\gamma_e}\tau_p$, where γ_e is the relativistic factor of the electron in the plasma wave. If one neglects other sources of delay to the measured value, this gives a relativistic factor of $\gamma_e = 2.3$.

When the radiator is placed at 1.5 mm from the source, the additional phase coming from the transverse extension of the electrons bunch is negligible compared to 2π. For a usual divergence of the electron beam of $\theta_0 = 5$ mrad (half angle), this phase term equals $\pi\theta_0^2 l/\lambda = 0.23$ at a wavelength of $\lambda = 500$ nm. Consequently, the OTR emission depends only on the longitudinal (temporal) structure of the electron beam.

For instance, the main features of the observed spectrum in Fig. 3.18a) are reproduced in Fig. 3.18b) using the temporal profile shown in the inset. The first pulse is modulated at 550 nm by the laser pulse in order to produce a peak in the radiation spectrum. The second bunch, delayed by 75 fs, is not under the influence of the laser (not modulated) and creates a broadband OTR spectrum over the optical wavelengths which interferes with the peaked spectrum. There exist various realistic temporal profiles that allow to reproduce the observed modulations. Here, it is assumed that both electron bunches have the same electron spectrum corresponding to a measured one. The first and second bunches respectively contain 70 % and 30 % of the charge and have a duration of 10 fs and 3 fs (FWHM). Because the second electron bunch is not expected to be modulated, a fundamental result is the requirement of an ultra-short bunch duration (a few femtoseconds) in order to reproduce the signal level obtained in Fig. 3.14. These durations depend weakly on the other parameters of the electron distribution (distribution profile, fraction of charge contaned in each bunch, chape and amplitude of the modulations in the first bunch).

The interference of coherent OTR signal in the spectral domain has shown the generation of successive electron bunches in laser-plasma interaction. These are the different electron bunches which are observed usually on the electron spectrometer.

These results show the measurement of electron beam structures which generate a coherent radiation in the visible range. This radiation, coming from modulation of the electron beam by the blue-shifted laser electric field, losses coherence during propagation of the electron beam in vacuum. The frequency shift behind the laser pulse is presented in section 3.3.1 to explain the temporal shortening o the laser pulse. The structure of the electron beam can be even more complex and can contain several bunches, which leads to interference patterns in the radiation spectrum of femtosecond electron bunches. Very short electron bunches are necessary to reproduce the energy level measured experimentally.

3.2.6 Measurements in the terahertz range

Similar measurement were done in another frequency range from 8 to 10 μm (Faure et al., 2006). This corresponds to frequencies of the order of 30 THz. This experiment was performed in collaboration with the Laboratoire d'Optique et Biosciences. The experimental setup is shown on Fig. 3.19. The same radiator as before is placed at position $L = 3$ mm from the electron source. The radiation is recorded using a nitrogen-cooled HgCdTe infrared detector. This detector is sensitive to wavelengths shorter than 12 μm and its absolute calibration is known. The angle of collection is limited to $\theta_0 = 10$ mrad. In this study, the size of the electron beam on the radiator $\theta_0 L$ is shorter than the radiation wavelength, which imply spatial coherence of the signal. This detector is sensitive to the to the temporal coherence of the electron bunch and the measurement is sensitive to electron beam structure around 8-10 μm. This wavelength is comparable to the bunch duration. If the electtron bunch has structures of 30-50 fs, one should observe a coherent

signal around 10 μm.

Formulas given previously for the OTR radiation are still valid here, and more generally for frequencies below the critical frequency of the metal. This one is defined as the plasma frequency corresponding to the free electron density ($\sim 10^{16}$ Hz) (Jackson, 1925, p285).

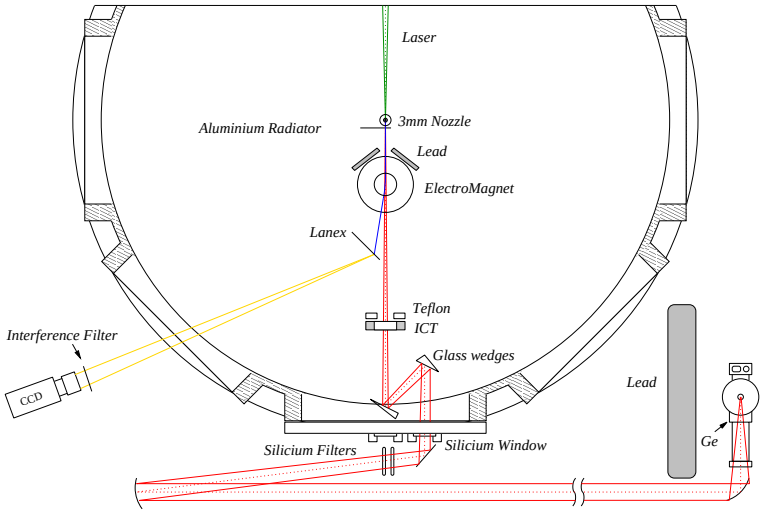

Figure 3.19: Experimental setup for the measurement of radiation in the range 8-10 μm.

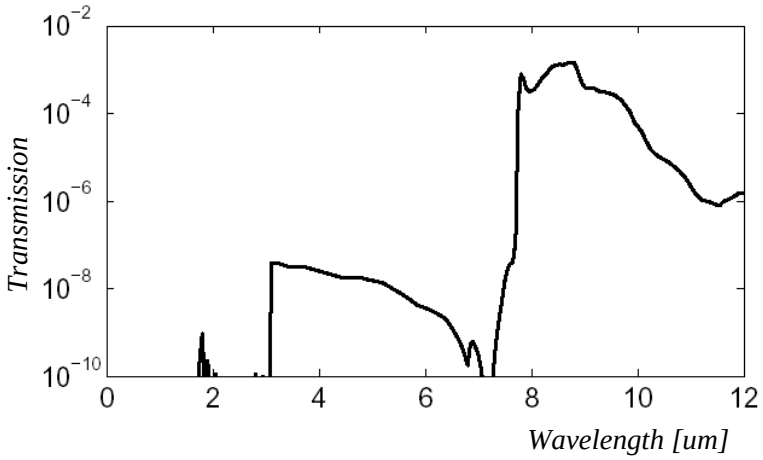

Figure 3.20: Global transmission including germanium filters, silicon filters, glass wedge and interference filter.

The measurement of the electron beam duration in the THz domain has already been used on conventional accelerators (Kung et al., 1994). This method was also used for electron beams originating from laser-plasma interaction in the range (Leemans et al., 2004). It is also possible to measure the bunch duration using electro-optic diagnostic (Yan et al., 2000; Wilke et al., 2002). This is based on the measurement of the rotation of polarization induced by the electric field from the electron beam as is propagates close

to a birefringent crystal. However, the geometry of such experiments makes very difficult the measurement of electron bunches shorter than 100 fs.

The global transmission of the filters (germanium, silicon, glass wedge, interference filter) is shown on Fig. 3.20. It is maximal at 8-10 μm and strongly damped for the laser wavelength. We checked that no signal was recorded without gas, when the laser directly hits the radiator. With gas, we have measured an intense signal at 8-10 μm. Using the calibration of the detection system, the energy is estimated to $dW/d\lambda = (6.5 \pm 3) \times 10^{-10}$ J/μm.

During this experiment, we have also measured the electron spectrum using the scintillator. It can be used to estimate the incoherent level of radiation by integrating the contribution from each electron.

$$\left.\frac{d^2W}{d\omega d\Omega}\right|_{Inc} = \frac{e^2}{4\pi^3\varepsilon_0 c}\sum_{n=1}^{N}\left\|\vec{E}^{(n)}\right\|^2 \tag{3.12}$$

where N is the number of electron above 50 MeV, $\left\|\vec{E}^{(n)}\right\|$ is the norm of the electric field emitted by electron n for an incidence angle set to zero (Eq. 3.5). The OTR radiation propagates with a divergence angle of $1/\gamma$. Due to a collection angle of 10 mrad, the radiation emitted by electrons below 50 MeV contribute weakly to the measured signal.

Fig. 3.21 shows the level of signal measured and the estimation in the incoherent case using Eq. 3.12. The incoherent level is below the measurement by three orders of magnitude. Consequently a part of the radiation emitted is coherent and the electron beam has temporal structures shorter than 50 fs.

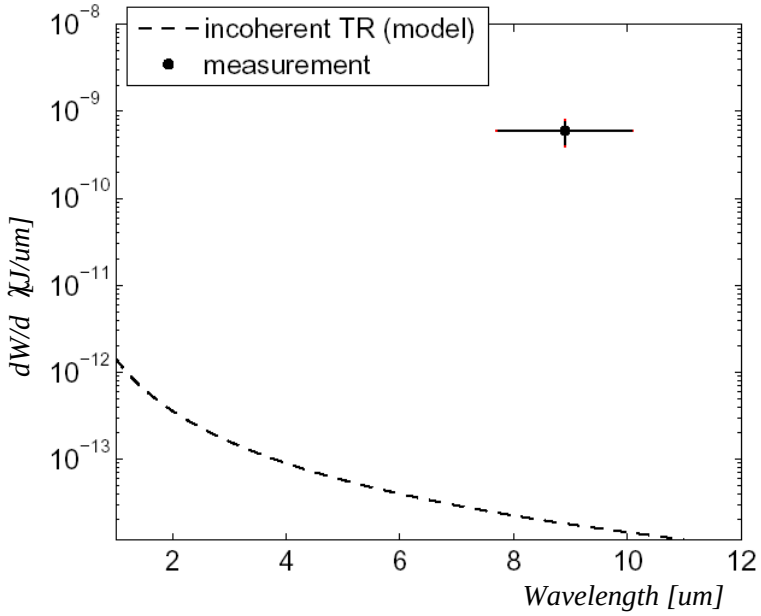

Figure 3.21: Spectral energy emitted : (point) measurement on the detector using the calibration of the experimental setup, (dashed line) level obtained for an incoherent emission.

Fig. 3.22 shows the evolution of the infrared signal and the number of electrons as function of the electron density. The optimum of coherent signal corresponds to optimal

interaction conditions, when the electron spectrum contains high-energy particles. Due to relatively large errorbars, it can't be said if the signal evolves linearly or quadratically with the charge.

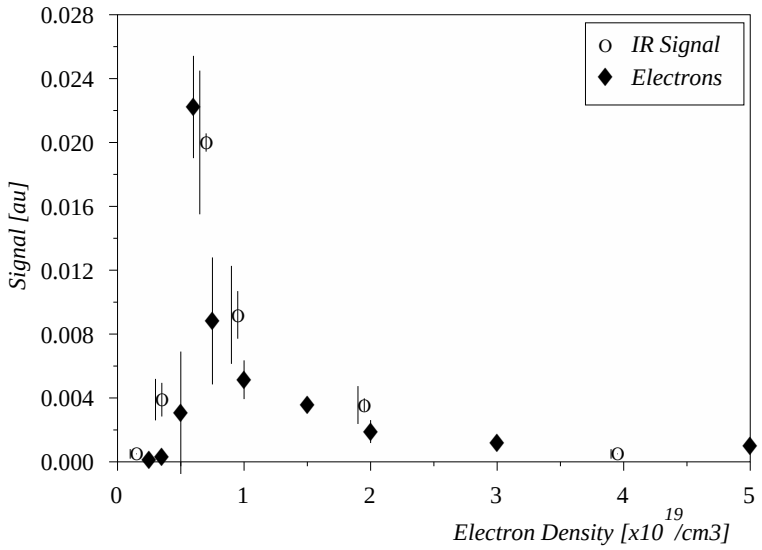

Figure 3.22: Infrared signal and number of electrons as function of the electron density. Errorbars on the infrared signal correspond to the electromagnetic noise on the measurement. Double errorbars are applied on the signal from electrons : one from the level of noise (on the left of circles) and the other from statistical fluctuations (in the middle of circles).

Finally, this measurement shows a partially coherent radiation, generated by an electron beam containing sub 50 fs structures. When trying to reproduce the observed level of signal using several realistic bunch profiles, the electron bunch duration needs to be shorter than 100 fs (FWHM) (Faure et al., 2006).

3.3 Laser pulse properties

Previous diagnostics were focused on the properties of the electron beam. The transmitted laser spectrum was also measured (Faure et al., 2005). I start by presenting some mechanisms responsible for the shortening of the laser pulse duration.

3.3.1 Origin of temporal shortening

In plasma, the propagation of the electric field depends on the refractive index of the medium (see Eq. 1.5). In the frame of a weakly relativistic interaction where the plasma response can be linearized, the index of refraction in under dense plasma ($\omega_p \ll \omega_0$) and with a linearly polarized laser field is

$$\eta = 1 - \frac{\omega_p^2}{\omega_0^2}\left(1 + \frac{\delta n}{n} - \frac{\langle a^2\rangle_t}{2}\right) \tag{3.13}$$

where there are two kinds of corrections, which depend on position $\xi = z - ct$:

- $\delta n/n$ is the electron density perturbation from the plasma wave. For long laser pulses, this gives birth to self-phase modulation instability, presented in Sec. 1.4.2.
- $\langle a^2 \rangle_t / 2$ is the relativistic correction to the refractive index. This term is responsible for relativistic self-phase modulation and relativistic self-focusing. Operator $\langle . \rangle_t$ is the average over an optical cycle.

The frequency shift obtained from the variation of refractive index is :

$$\delta\omega = \omega_0 \int \frac{\partial \eta}{\partial \xi} dz \tag{3.14}$$

Individual frequency shifts are shows on Figs. 3.23b-c. In the end, the intense part of the laser pulse stands in a red-shifted area (Fig. 3.23d). This local variation of the index of refraction also leads to a local variation of the laser group velocity

$$v_g = \frac{\partial \omega}{\partial k} = c \left(1 - \frac{1}{2} \frac{\omega_p^2}{\omega_0^2} \left(1 + \frac{\delta n}{n} - \frac{\langle a^2 \rangle}{2} \right) \right) \tag{3.15}$$

This is shown on Fig. 3.23e. The front of the laser pulse propagates slower than its back. This leads to a temporal shortening of the laser pulse during propagation.

This 1D explanation corresponds to simplified hypothesis but help to understand the origin of the obtained results.

3.3.2 Laser spectrum broadening

The transmitted laser pulse is significantly damped by the use of the reflexion on a glass wedge and 5 μm-thick pellicle. The laser light is collected using a spherical mirror and the pulse exits through a 300 μm-thick Mylar foil. The B-integral can be neglected in this window. Fig. 3.24 shows the two diagnostics used simultaneously : a single shot auto-correlator and a spectrometer. The beam is once again damped using pellicles and a glass wedge to adapt the intensity to the sensitivity of the CCD camera. An 8-bit CCD camera is used in the autocorrelator and a 16 bits Andor CCD is mounted on the spectrometer. The laser is focused on the slit of an imaging spectrometer containing a grating with 300 lines/mm.

Fig. 3.25 gives the transmitted laser spectrum for several electron densities, after de-convolution from the spectral response from the grating and the CCD. Without gas, the spectral width is 35 nm (FWHM). With gas, one notices an important red-shift, signature of the effect from plasma waves and relativistic effects. The spectral width reaches 100-150 nm (FWHM), which corresponds to a Fourier transform limit of 7-8 fs. Of course the spectral broadening is a consequence of temporal shortening but no evidence is given here. Consequently, a single sot auto-correlator has been used to measured the pulse duration.

3.3.3 Temporal shortening of the laser pulse

A single shot autocorrelator (Rebibo, 2000) has been used to measure the pulse duration. It contains a 50 μm-thick and type I BBO crystal. A prism used in reflection splits the

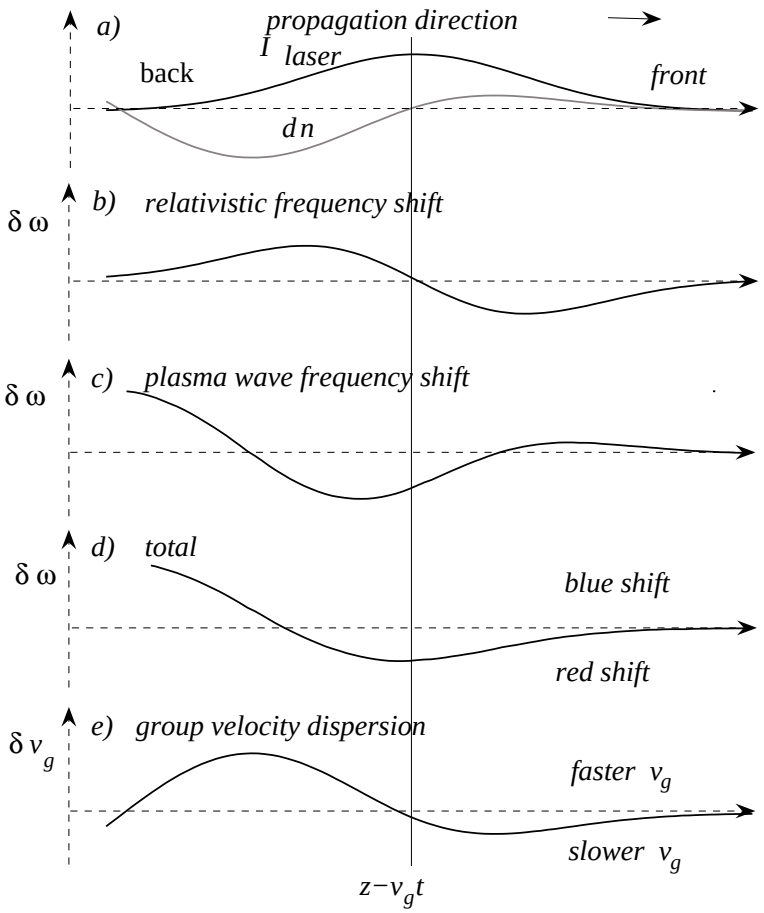

Figure 3.23: Principe of laser pulse shortening : a) Laser intensity and electron density perturbation, b) frequency shift from relativistic correction, c) frequency shift from plasma wave, d) sum, e) group velocity dispersion.

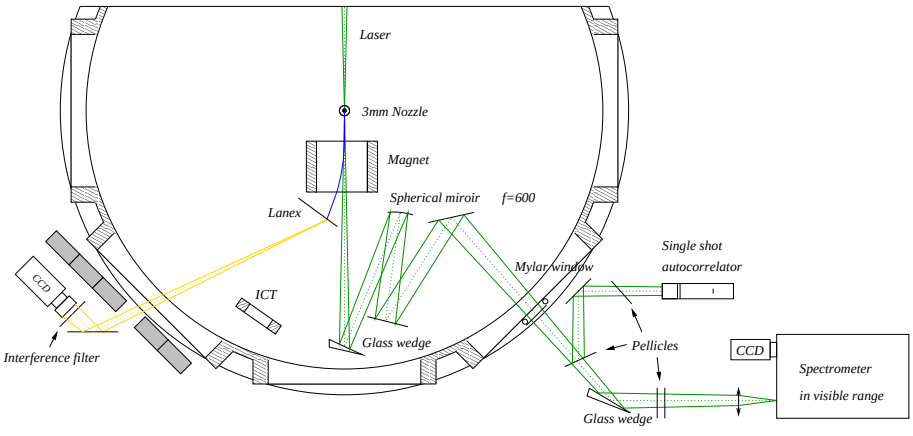

Figure 3.24: Experimental setup for the simultaneous measurement of laser pulse duration and spectrum.

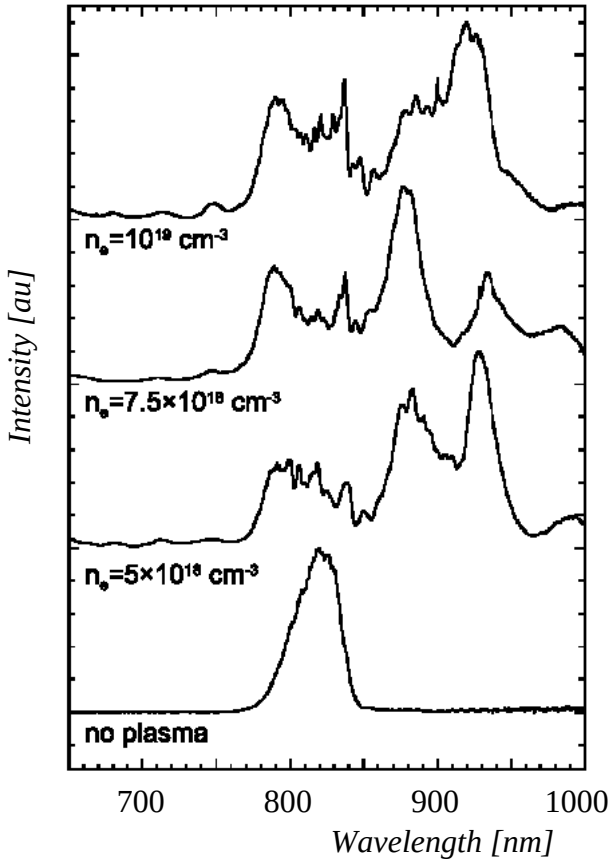

Figure 3.25: Transmitted laser spectrum for several electron densities.

laser beam in two parts which are sent in the crystal with an incidence angle of 5°. The minimum pulse duration that could be measured was 10 fs and includes the resolution from the geometry 2 fs and the phase matching from the BBO crystal which limits the measurement to 10 fs pulses.

Fig. 3.26 gives the signal obtained with and without gas. A significant pulse shortening is observed with gas. Without gas, the autocorrelation signal gives a FWHM width of 53 ± 2 fs. Hypothesis on the temporal shape of the pulse must be done to retrieve the temporal width of the pulse. The assumption of a Gaussian pulse leads to an initial laser pulse duration of 38 ± 2 fs (FWHM). With gas, the width of the autocorrelation signal shrinks down to 14 ± 2 fs (FWHM). Here, it's less easy to give an estimation of the temporal profile. Assuming extreme cases, a square pulse profile would lead to a width of 14 fs (FWHM), and a Gaussian pulse (best case) would lead to a duration of 9.9 ± 1.4 fs (FWHM) which is close to the resolution of the detector. There exist more complex temporal shapes that can lead to a thin autocorrelation trace even if the laser pulse has a large envelope (Trebino, 2002). Even if such modulations of the laser pulse in under-dense plasmas is not very likely, complementary measures using Spider or Frog techniques are necessary.

With gas, the image is smoother than without gas. In reality, this "auto-correlator" gives the temporal correlation between two separated parts of the same laser beam. Consequently, one should not expect a perfectly symmetric signal. The correlation in the beam coming from amplification stages, even if spatially filtered, gives inhomogeneities without gas. Image 3.26a gives the raw correlation of the beam, which contains intensity and phase inhomogeneities. On the opposite, during propagation of the beam in the plasma, non-linear effects mix the spatial information and lead to a better correlation of different parts of the beam. At the output, laser diffraction also mixes the information in near field where the measurement is done. Consequently, the correlation of two different parts of the beam is much more symmetric and vertically homogeneous with gas. The plasma smooths the laser. However, this effect doesn't appear so clearly on every shot.

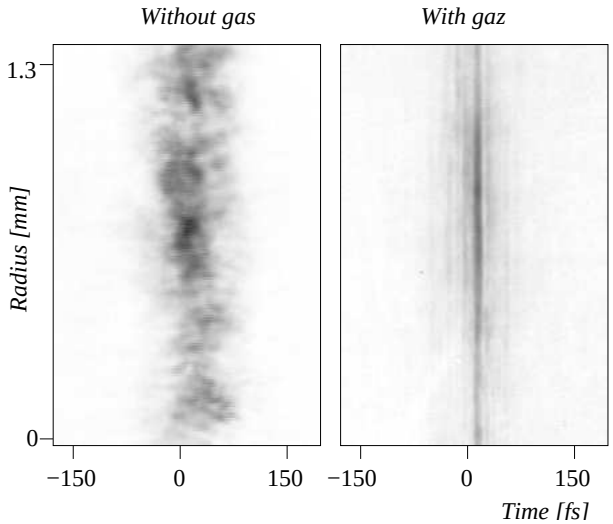

Figure 3.26: Signal obtained on the single shot autocorrelator with and without gas, for an electron density of 7.5×10^{18} cm^{-3}.

Finally, there are also secondary peaks in the autocorrelation signal with gas. This can be reproduced mathematically if one introduces, for instance, three secondary peaks in the temporal laser pulse profile. This may happen if the laser pulse doesn't completely fit in the first plasma bucket. In particular, when the electron density in increased (plasma wavelength decreases), one observes a modulated autocorrelation signal rather than a temporal shrinking (Faure et al., 2006) (see Fig. 3.27). This also refers to the difference between self-modulated laser wakefield acceleration (Sec. 1.4.2) and forced laser wakefield acceleration (Sec. 1.4.2).

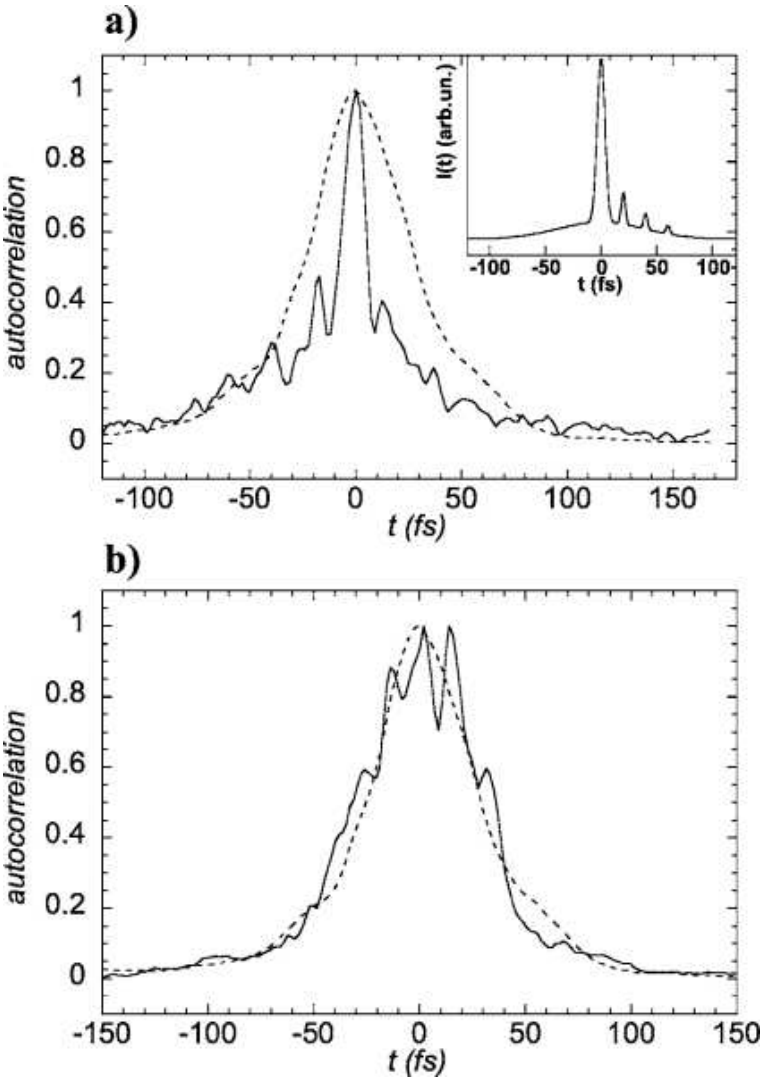

Figure 3.27: Autocorrelation signal for two different electron densities : a) 7.5×10^{18} cm^{-3} and b) 10^{19} cm^{-3}. The dashed curve represents the autocorrelation profile without gas. The insert on a) represents a possible shape which gives this autocorrelation trace.

Finally, the laser pulse was likely to be shortened from 38 fs to 10-14 fs when the laser pulse duration is close to the resonance with the plasma wavelength. Additional measurements are necessary to confirm this temporal shortening. The compression efficiency was

estimated to 20 ± 5 % of the initial energy. Such properties are interesting because the spectral band of amplification of crystals limits the laser pulse duration to values of about 30 fs. Other techniques which allow pulses shorter than 10 fs are used at lower energy (self-modulation in capillary tubes, optical parametric amplification). Their use at higher laser energy still needs to be demonstrated.

3.3.4 Transmitted laser intensity

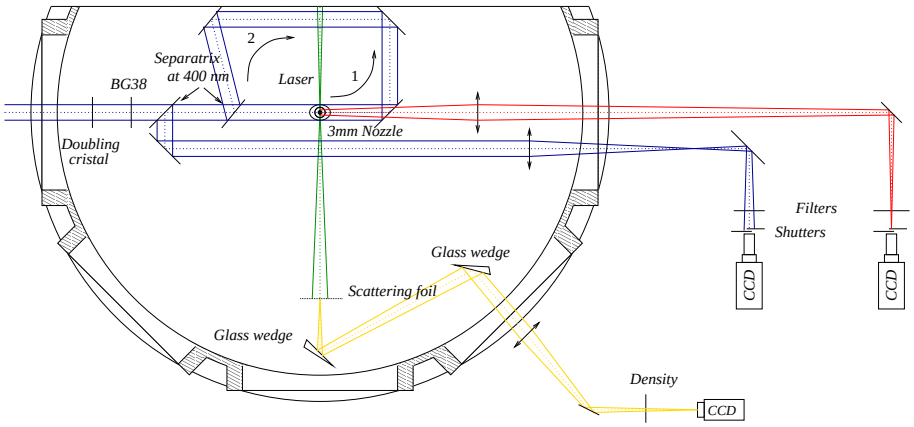

Figure 3.28: Experimental setup : Imaging of scattering foil, interferometry and Thomson diagnostic.

A simple diagnostic to visualize the transmitted laser intensity after the interaction point was set up (see Fig. 3.28). The imaging screen is a sheet of optical paper, placed perpendicular to the laser axis at a distance of 36 cm from the interaction point. This very thin scattering foil is imaged onto a CCD camera. Two glass wedges used in reflexion and neutral density filters are used to damp the radiation intensity. Fig. 3.29 shows the intensity profile measured with and without gas. Without gas, the signal is rather homogeneous in a ring corresponding to the natural divergence of the beam. With gas, a fraction of laser energy is scattered during the interaction. One observes a scattered radiation much wider superimposed with the fraction of light which remains in the cone of initial divergence.

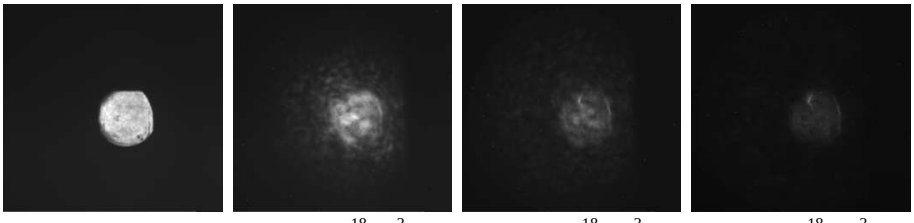

Figure 3.29: Spatial intensity distribution on the scattering foil for different electron densities. On the left, image without gas. Images have been normalized to the same color table.

When integrating the intensity over the solid angle corresponding to the natural divergence of the beam, one can estimate the fraction of signal contained in this area as function of the electron density. Fig. 3.30 summarizes this trend. The higher the electron density, the more scattered the radiation.

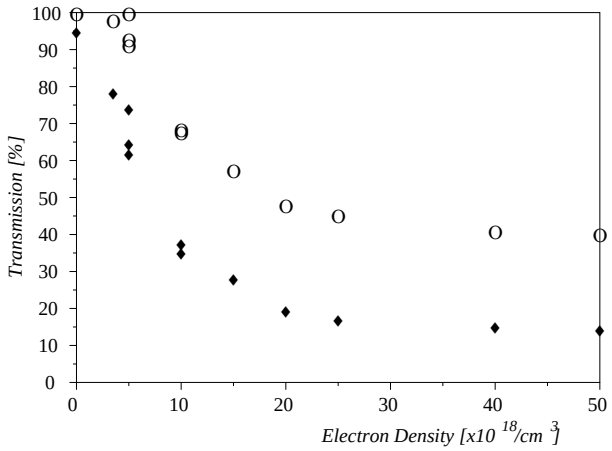

Figure 3.30: Fraction of laser intensity integrated over the whole scattering foil (circles) or in the cone of natural divergence of the laser beam (filled diamonds).

If the scattering foil is optically thin, then it acts as an attenuating filter on the incident radiation. It is considered here that the measured signal is proportional to laser intensity. In that case, curve 3.30 gives the fraction of energy contained in the laser cone after interaction. One notices that for an electron density of 6.0×10^{18} cm^{-3}, the transmission is about $40\% \pm 10\%$ in the laser cone. This value matches with the estimation on the single shot autocorrelator for the same aperture. When using the whole collected signal, $20\% \pm 10\%$ of laser energy is estimated to be scattered outside the laser cone. Finally, $40\% \pm 10\%$ of laser energy was damped in the plasma waves and a fraction of this energy is transfered to electron kinetic energy.

3.3.5 Thomson scattering

Electromagnetic dipole radiation emitted during the motion of an isolated electron in the laser electromagnetic field is called Thomson scattering. The emission lobe of this radiation at the laser frequency is directed along the vertical axis (perpendicular to the optic table). A mirror and a lens have been placed above the nozzle to collect the light and image the plasma onto a CCD (see Fig. 3.28). Fig. 3.31 shows and example of image. One notes an intense signal where the laser is focused, folowed by a weaker tail on a longer distance. Sometimes, we have observed several successive peaks, probably linked to successive refocus of the laser pulse. This diagnostic allows to visualize the propagation of the laser.

The physical meaning of the signal recorded is not obvious. The signal measured S depends on the laser intensity $I(y)$ and the electron density $n_e(y)$ (see Eq. 3.16) (Thomson, 1928). In the case of a very weak intensity, so that the plasma density perturbation is negligible, the signal depends only on the integral of the laser intensity along a line of

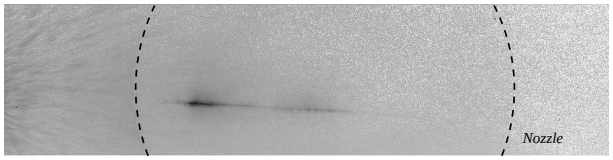

Figure 3.31: Example of Thomson scattering image. The laser is focused in the gradient of the gas jet density profile and propagates from left to right. Dashed line represents the output of the 3 mm diameter nozzle in the background.

sight.

$$S \propto \int I(y) n_e(y) dy \tag{3.16}$$

But in our very non-linear experimental conditions, the electron density is greatly modified by the propagation of the laser pulse and the signal gives no longer direct information on the laser intensity (Chiron et al., 1996). For instance, if the laser ponderomotive force expells all the electrons radially, the cavity in which stands the laser pulse doesn't contribute to Thomson scattering due to a lack of electron. Therefore, it's incorrect to try to estimate the maximal laser intensity or the interaction length from this diagnostic. In our experiments, the laser power exceeds the critical power for laser self-focusing P_c and the laser vector potential a_0 exceeds unity. This interaction is therefore very non-linear and this diagnostic is mainly used to align the laser beam along the center of the nozzle. The control of the interaction length can be reliably obtained by modifying the longitudinal density profile with a second laser pulse (Hsieh et al., 2006). This leads to a more accurate estimation of the local accelerating field of the plasma wave.

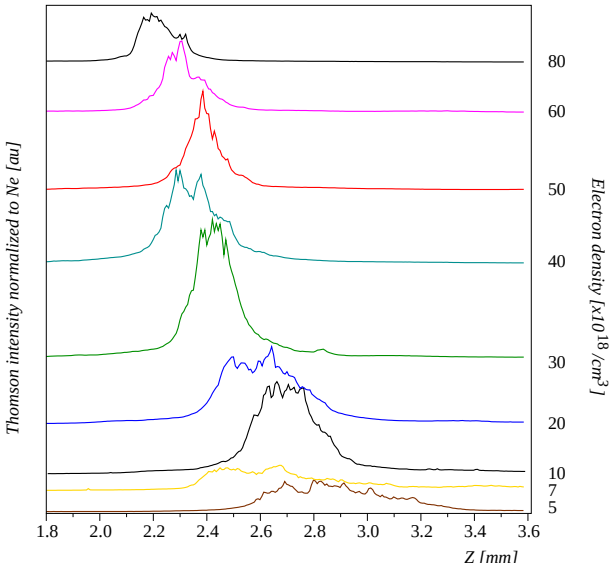

Figure 3.32: Intensity of Thomson scattering divided by the electron density for several electron densities. The signal was integrated along the transverse axis. Curves were shifted to avoid overlapping. The laser propagates from left to right.

However, some trends can be seen as the electron density varies. Fig. 3.32 shows the integrated Thomson scattering signal for several electron densities. Because the amplitude of these normalized curves is similar, this means that the Thomson scattered intensity is roughly proportional to the electron density as in the linear case. As the electron density increases, The emission of radiation starts further to the left. For such length (~ 0.5 mm), the properties of the laser doesn't significantly evolve because this length is shorter than the Rayleigh length (see Table 2.1). The critical power for self-focusing P_c depends on the electron density, which varies rapidly in the density gradient of the gas jet. For this interaction parameters, self-focusing starts at a given electron density. The increase of the electron density at the center of the nozzle also shifts the position where this critical density is reached towards the outer part of the nozzle. Self-focusing starts earlier.

3.3.6 Interferometry

Very often, this diagnostic is based on Michelson interferometer. But for ultra-short laser pulses, the length of each arm must be tuned to a precision less than 10 microns, which can be difficult. Consequently, a system filling the folowing criteria was searched for : systematic interferences, adjustable interfringe and maximal interference amplitude. Sagnac interferometer fulfills these requirements. The probe beam is split in two arm (labelled 1 and 2 on Fig. 3.28) using a beam splitter and the two pulses follow exactly the same optical path but in opposite direction. Interferences are automatic and their amplitude is 100 %. The delay between the two pulses above the nozzle depends on the size of the ring (2 ns in our experimental conditions). The experiment was set up so that the interaction of the main beam with the plasma takes place between the two snapshots of the plasma from the interferometer. Pulse 1 is the reference and crosses the gas jet before the main pulse. Pulse 2 reads the plasma density profile after interaction and contains all the information about the refractive index. This diagnostic is used at 400 nm using a BBO doubling crystal. We use a filter BG 38 to damp the laser wavelength at 800 nm by 5 orders of magnitude each time and to let the 400 nm go through. Radiation at 400 nm goes back to the laser system and are supressed by the compressor. This allow protection of the laser system.

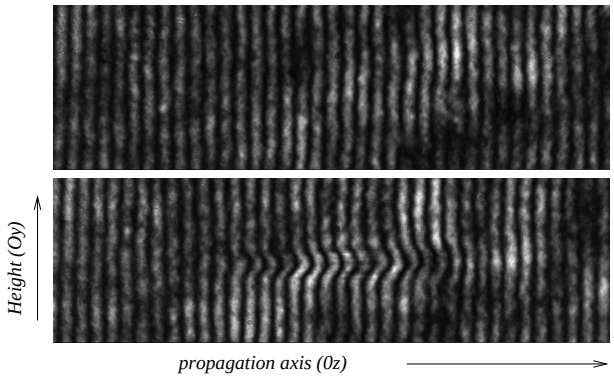

Figure 3.33: Interferometry diagnostic : (top) fringe pattern without interaction, (bottum) interferogram 17 ps after beginning of interaction. The laser propagates from left to right.

Fig. 3.33 shows the fringe pattern and and example of interferogram 17 ps after the beginning of the interaction for another 3 mm diameter nozzle. Fourier analysis leads to the phase map. A filter is applied to select frequencies around the fundamental wave number k_i of the interferogram. The spectrum is then shifter by $-k_i$ and the inverse Fourier transform is applied. The low frequency part of the modulation remains, corresponding to phase shift by the plasma. This phase shift ϕ depends on the integral of the refractive index $\eta(x)$ along a line of sight.

$$\phi = \int (\eta(x) - 1) k_i dx \tag{3.17}$$

where k_i is the wave number of the pulses in the spectrometer. For very underdense plasmas, the refractive index depends on the electron density as

$$\eta(x) = 1 - \frac{n_e(x)}{2n_c} \tag{3.18}$$

Under the assumption of an axi-symmetric density profile around the laser axis, the Abel inversion allows the retrieval of the electron density profile $n_e(r)$. This last part of the analysis is very sensitive to noise and initial parameters. Fig. 3.34 is the density map obtained after signal deconvolution. This map shows the free electron density, those removed from their initial Helium atom during the propagation of the main laser beam. The laser propagates at 1 mm above the output of the nozzle, from left to right. Numerical noise appears at the border of the image due to the analysis. One notices that density gradients are very sharp longitudinally, and that laser defocuses beyond focal plane (located at the entrance of the gas jet). A cut in electron density at position 3200 μm is drawn on the right side. The electron density reaches 16×10^{18} cm^{-3}, which is in fairly good agreement with independent measurement of atomic density, giving a maximal electron density of between 17 and 20×10^{18} cm^{-3} at this pressure (method described in Ref. (Semushin and Malka, 2001)). Fluctuation on top of the curve strongly depend on the analysis and have no physical meaning. This lineout, taken at the entrance of the gas jet, corresponds to the location where the laser is focused. The width of the ionized area is around 150 μm (FWHM) at this location.

In this section, correlation of the output angle of the electron beam with the electron energy was recorded, arising from an off-axis injection. The electron beam is modulated by the laser pulse at a frequency which appears using OTR radiation. The same measurement has also shown that a second electron bunch might be accelerated also in the next plasma bucket. The measurement in another spectral window indicates that this electron beam has temporal structures shorter than 30-50 fs, which gives an upper limit on the pulse duration. Finally, the laser itself is strongly modified and temporally shortened during this interaction down to intense pulses of 10-14 fs. Measuring the transmitted laser intensity, the laser energy which was dumped into the plasma waves was estimated to 40 % in our experimental conditions. Two other diagnostics allow to see the laser propagation : Thomson scattering gives the position where laser radiation is scattered on the plasma electrons and interferometry diagnostic gives the free electron density in the plasma, after the laser pulse has passed.

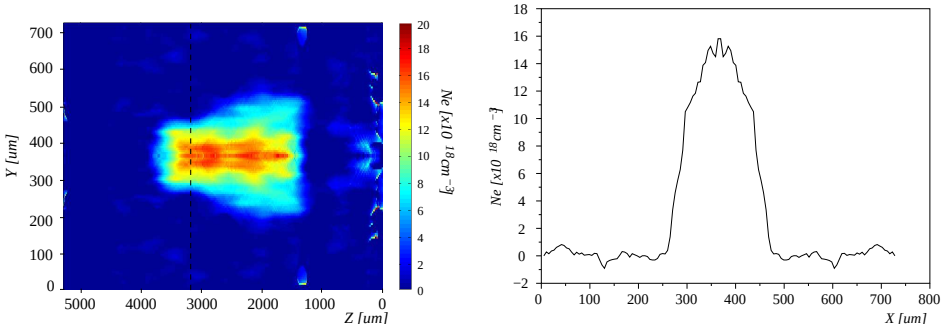

Figure 3.34: (Color) Electron density map in the plane containing the laser axis (Oz) and the vertical axis, 17 ps after beginning of interaction (left). The laser pulse propagates from left to right. Transverse lineout at position 3200 μm (right).

Chapter 4

Applications of laser-based electron beams

The subject of this thesis also concerns the applications of these electron sources. The group Particle Sources by Laser (SPL) promotes applications which emphasize the original properties of this electron source. γ-ray radiography, radiotherapy, the study of water radiolysis and the generation of a collimated and energetic X-ray are some examples of the use of electron beams developed in our laboratory. I have worked only on the first two applications. However, I also present activities lead by other groups. The study of water radiolysis using ultra-short electron beams is the research topic of Y.A. Gauduel's group and the mechanism of X-ray emission by betatron oscillations has been discovered in laser plasma-interaction by the group of A. Rousse.

Each application emphasizes some properties of the electron source. The γ-ray radiography with submillimeter resolution requires a small electron source with low divergence. Radiotherapy with the electron beam is based on a quasi-monoenergetic spectrum, with low divergence and the high energy of the electrons. For water radiolysis experiments, the brevity and the collimation of the electron bunch are essential characteristics to improve the temporal resolution of the signal. Finally, the generation of X-ray flash using the betatron mechanism requires all the assets of this source (electron energy, collimation, brevity and charge ...). Here are the results obtained in each field.

4.1 Application to radiography

Electron beams produced with 20 MeV conventional accelerators are difficult to focus to a spot size smaller than 1 mm due to the emittance of the beam (Lin, 1998; Haase et al., 2002). Consequently, the γ source, which is the bremstrahlung radiation produced by the electrons as they slow down in a medium with high atomic number, has a spot size of a few millimeters. In our experimental conditions, the electron source size is lower than the focused size of the laser (18 μm) and the beam has a low divergence, Consequently, it's possible to generate a secondary source with small dimensions

High resolution radiography of dense objects having fine structures has allowed to estimate the size of this secondary source to a few hundreds of microns. The properties of the sub-millimetre γ-ray source are consistent with Monte-Carlo simulations (Glinec et al., 2004).

This secondary source is very promising for non-invasive control of dense material (Chen et al., 2002) or medical applications (Kainz et al., 2004) or in field of research where the transverse size of the γ-ray source must be reduced. These experiments were done in collaboration with CEA DAM Île -de-France.

4.1.1 High resolution radiography

Experimental parameters correspond to optimal ones except the electron density ($n_e = 7.5 \times 10^{18}$ cm^{-3}) which was slightly higher than in previous chapters in order to stabilize the properties of the electron beam from shot to shot. A maxwellian-like electron distribution (exponential decay) with an electron temperature $T = 40$ MeV is shown in Fig. 4.1. When magnets are removed, the transverse dose profile corresponds to a cone of 1° (FWHM) (shown in the inset of Fig. 4.1).

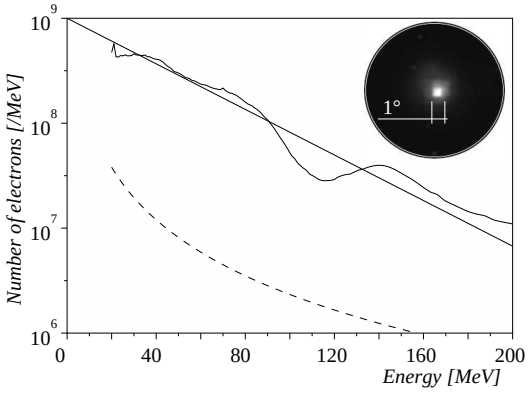

Figure 4.1: Electron spectrum fitted by a maxwellian distribution of temperature $T = 40$ MeV, and dose deposition profile in the scintillator shown in inset. The dashed curve the detection limit.

The experimental setup is shown on Fig. 4.2. The electron beam is converted into γ rays in a 2.5 mm-thick tantalum target, placed at 3 mm from the center of the nozzle. The bremstrahlung radiation produced during the scattering of the electron beam in the target is used to radiograph a spherical hollow object made in tungsten, placed at 220 mm from the nozzle. On the inner part, an axi-symmetric sinusoidal structure is etched on the inner part. These internal structures are shown on the $A - A'$ cut of this object on Fig. 4.3. For the left (right) side respectively, each oscillation of the 6 (5) periods of the sinusoidal curve correspond to a rotation of 11° (13°) and an amplitude of 1.9 mm (2.4 mm). The mean radius of the sinusoid from the center is 7.85 mm, which gives a thickness of 0.67 cm of tungsten along the laser axis (line of sight passing through the center of the object). For a controlled density of 18.064 ± 0.015 g/cm^3, this gives an areal density of 12.1 g/cm^2 along the laser axis. The axis of symmetry is chosen perpendicular to the laser axis.

The transmitted radiation is damped by the object and then detected on a γ camera composed of a Bismuth-Germanium-Oxide (BGO) scintillator, the surface of which is imaged onto a CCD camera. The imaging system is composed of a plane mirror, an objective with focal length of 105 mm, an intensifying screen and a CCD with 1300×1340 pixels. The size of each bar of the BGO crystal (600μm) in this square matrix with edge

160 mm limits the resolution of the detector. The scintillator is placed at a distance 1.6 m from the electron source. This makes a magnification factor of 7.3, which corresponds to a BGO bar size of 80 μm in the object plane. This choice of the magnification factor is a compromise between a correct spatial resolution and a dose deposition level high enough to be detected on the γ camera. The nozzle-to-object length is chosen large enough to limit the problem of parallelism which might blur the fine details on the radiography. In order to limit the noise on the image, electrons are removed from the laser axis using a magnetic field. This allows a reduction of radiation generated in material other than tantalum (especially in the object itself). An aluminum foil was added to scatter the electron beam and improve the contrast of the image. After several tries with different thicknesses, a thickness of 7.5 mm was chosen. Combination of magnets and aluminum foil allows an efficient reduction of noise generated in the object.

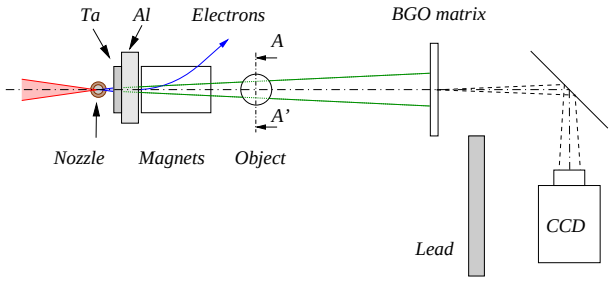

Figure 4.2: Experimental setup. Electrons are accelerated during the interaction between the laser pulse and the gas jet and then slown down in the tantalum target, which generates γ rays. Electrons are then removed from the laser axis with an intense magnetic field and an aluminum diffuser. The transmitted radiation intensity is then imaged onto a γ camera.

The experimental radiography obtained is shown on the right side of the 3D cut of the object on Fig. 4.3. The radiography shown has been corrected for the inhomogeneities (using a radiography without the object) in order to suppress the grid of the BGO matrix and to take into account the emission lobe of the γ radiation. All sinusoidal lobes can clearly be seen. From this image, the radial profile of the object can be reconstructed.

4.1.2 Retrieval of the internal profile of the object

This paragraph contains information transmitted by L. Le Dain.

The retrieval of the radial profile of the object has been done at CEA DAM Île-de-France with numerical tools developed during J.M. Dinten's thesis (Dinten, 1990). This axi-symmetric object is visualized perpendicular to the axis of revolution, which is adapted for a classical Abel reconstruction (Bracewell, 1999). This direct method is too sensitive to noise (especially close to the symmetry axis). A regularization on the data is introduced in the reconstruction process to reduce the sensitivity to the noise. Non-physical variation between two neighbor pixels is avoided. Fig. 4.4 represents the density field reconstructed for two kinds of regularization. This reconstructed profile reproduces all internal structures. A relatively high level of noise appears in the center of the object.

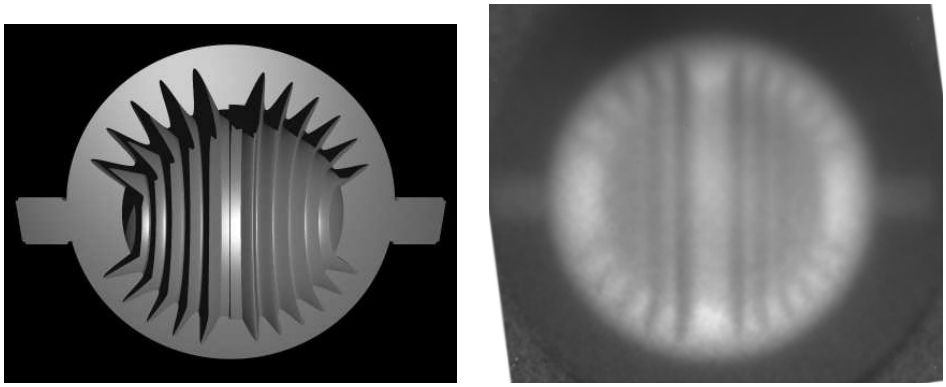

Figure 4.3: (left) 3D cut of the object, revealing the internal structure, (right) radiography of the 20 mm-diameter object. The experimental image has been corrected using a reference shot without the object.

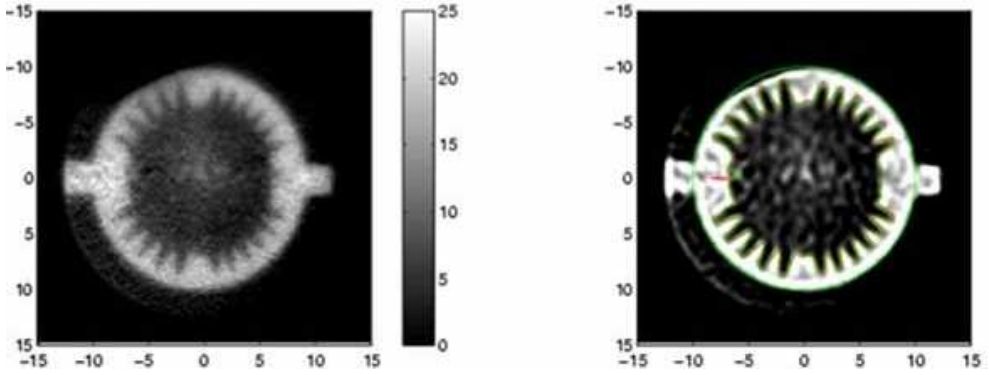

Figure 4.4: Radial profile of the object obtained from radiographs in Fig. 4.3. The two images correspond to two different parameters of the regularization process.

Then, a detection of contour is applied on the image. The algorithm is described in the following:

- Localization of zeroes of the Laplacian function calculated with local polynomial approximations on a moving window on the image (Qiu and Bhandarkar, 1996; Abraham et al., 2006). The validity of contours is given by a measurement of contrast.
- Contours are extracted manually by following maximal values.

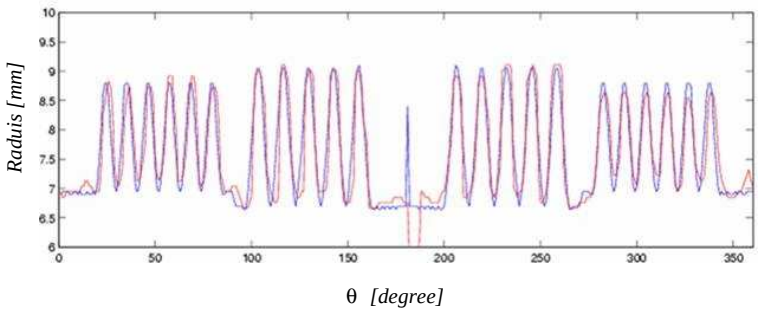

Figure 4.5: (Color) Internal contour of the object. This represents the radius of the contour as function of the angle from the center : (blue) theoretical contour, (red) retrieved contour.

In order to estimate the quality of the processing, the contour is compared to the theoretical contour from the manufacturer. Fig. 4.5 shows the open contour reconstructed from the radiography image and the theoretical contour. Thanks to good experimental data and a reduced blur, the two contours match very well. This experimental contour is also represented in green on the image on the right in Fig. 4.4.

4.1.3 Estimation of the γ-ray source size

The high resolution radiography presented above requires a small secondary source size. Even if the experiment was not designed to measure initially the source size, one can estimate it from radiographs and compare the results to Monte-Carlo simulations.

The radiography of an object with sharp edges was done to estimate the secondary source size. A 20 mm-thick steel plate in which square holes are drilled was used. A picture of this object is shown in Fig. 4.6. The radiography of the smallest holes is shown in the right side of the picture. Lines from the manufacturing process are also visible. This image is comparable to images obtained using the knife edge technique to estimate the source size. The signal was integrated over 5 horizontal lines around the central square on the radiography. The size is computed from using the derivative of this signal, which gives a source size of $450 \pm 15 \mu$m (FWHM).

This estimation contains several sources of error, which may lead to an over-estimation of the real size.

- the intrinsic detector blur (~ 170 μm in the plane of the object).

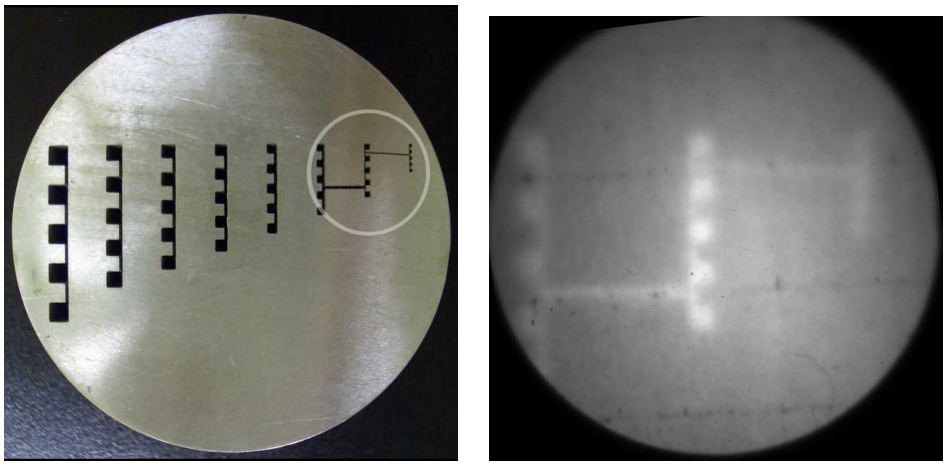

Figure 4.6: (left) Photo of the 20 mm-thick steel plate with square holes. The radiograph corresponds to the circle. (right) Radiography of holes with length 1.0, 0.75 and 0.4 mm used to estimate the γ-ray source size.

- the alignment of the 20 mm thick plate, which must be perfectly perpendicular to the laser axis, to reproduce a knife edge.

- noise on the radiography from electrons which may still generate γ-rays in the object itself.

Whatever, the spatial quality of the γ-ray source can be controlled and enhanced by placing the conversion target closer to the source or by decreasing the target thickness or even by using a more dispersive magnet to avoid using an aluminum foil.

Monte-Carlo simulations were carried out to estimate the properties of the radiation produced in the conversion target (Glinec et al., 2004). Simulations in the article give the radiation spectrum and allow the estimation of the divergence of the γ ray beam to approximately 3° (FWHM). The conversion efficiency of the kinetic energy from the electrons in radiation is about 49% in the tantalum target and about 3% in the aluminium target. Consequently, the contribution of this aluminium foil to the radiation can be neglected.

This experiment allowed the production of energetic and collimated secondary photon source, the size of which was estimated to be 450 ± 15 μm experimentally. The retrieved radial profile of the object testifies of a high resolution of the initial radiograph.

For this application a quasi-monoenergetic electron beam is not necessary. Actually, the process of bremstrahlung radiation leads to a broadband γ spectrum which is almost independent of the spectral structures of the electrons beam. Consequently, constraints on the generation of the electron beam are less strict, and shot to shot stability is improved. Commercial 100 TW laser systems are compact and affordable. Several fields of science might benefit from small and short γ sources. A snaphot of dense objects in motion can be obtained for aeronautics or defense. Evolution of structures under constaints and sub-millimeter cracks detection might have an interest in the car industry.

4.2 Application to radiotherapy

Currently, 99 % of radiotherapy is done with X ray beams. However, the dose deposition profile is not the best fitted to this application. Fig. 4.7 shows the depth dose deposited by different particles. Due to Bragg peak, protons deposit their energy at a depth corresponding to their energy. These particle are the most adapted to radiotherapy because they minimise the dose deposited in safe tissues but the production cost of such beams prevents from a rapid development. Moreover, the intensity modulated technique is rather limited for proton beams due to a slow motion of the heavy gantry. A seductive alternative is currently under development : proton beams can be produced from the interaction of a laser with a solid target. This is the second research topic of the SPL group at LOA. The study of the adequacy of proton beams from laser-plasma interaction to radiotherapy has already been published Malka et al. (2004). Such systems benefit from a reduced radioprotection because the proton beam can be produced in the treatment room and the transport of laser radiation up to the patient is cheap. This may also increase the speed of the gantry due to a reduced weight for intensity modulated protontherapy.

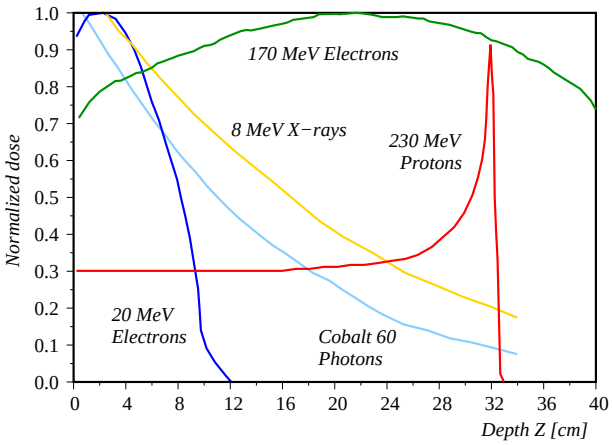

Figure 4.7: Comparison of the depth dose profile for different particles.

However, treatment using photons remains the more frequent. Electron beams from conventional accelerators with a modest size adapted to treatment rooms in hospitals have an output energy of about 20 MeV, which is not adapted to deep-seated tumors (above 10 cm). Feasibility studies for therapy with electron beams with energy 6-25 MeV from laser-plasma interaction (Kainz et al., 2004; Chiu et al., 2004) showed that these structures might be an alternative to conventional radiofrequency accelerators.

Recent development in radiotherapy, such as intensity modulated radiotherapy or volume scan with light ion beams, have significantly improved the conformity of the dose to a volume while sparing organs at risk (Oelfke and Bortfeld, 2003; Lomax, 1999). When combined with energy modulation, modulation in depth is also possible (Hyödynmaa et al., 1996; Åsell et al., 1997; Ma et al., 2000; Olofsson et al., 2004; DesRosiers et al., 2000; Yeboah et al., 2002). However, the maximum penetration depth for electron beams from conventional electron accelerators and the low quality of the transverse penumbra at this energy prevents from their use. These drawbacks can be avoided if the

electron energy is increased above 50 MeV. Under such conditions, the penetration depth becomes longer and the transverse penumbra sharper. On the opposite hand, the longitudinal penumbra is also increased. Assets of high energy electrons (150-250 MeV) for clinical applications has been recently investigated (Yeboah et al., 2002; Yeboah and Sandison, 2002). The authors compare the capabilities of prostate treatment using intensity modulated radiotherapy for photon, proton and high-energy electron beams. The conclusions states that best conformity to the volume is obtained for proton beam but covering rate for electron and photon beams are comparable. Moreover, electron beam provides a better lateral protection of safe tissues compared to photons.

A detailled study has been published in the range 150 - 250 MeV (DesRosiers et al., 2000). Simulations are performed for various configurations of the electron beam from a conventional accelerator (counter-propagating, perpendicular, ...). In order to fulfill this study and to show the interest of these compact sources for radiotherapy, I have simulated the dose deposited by a quasi-monoenergetic electron beam from our laser-plasma accelerator. The dose profile in a water phantom is computed for the electron distribution presented in Sec. 2.2. The study is carried out for two different geometries. On the one hand, the electron beam is used as it exits the interaction point. On the other hand, the electrons are refocused onto the target using different magnetic optics to improve the lateral gradient of the dose profile. A discussion is then drawn on the applicability of such beams. These simulations are performed in collaboration with DKFZ in Germany and this study has just been published (Glinec et al., 2006b).

4.2.1 Simulation parameters

Monte Carlo simulations with the code `Geant4` (*et al*, 2003) were performed in order to show the dosimetric properties of this electron beam. We first assume that the low energy part of the spectrum can be removed. For instance, one can imagine adding a chicane to stop all low energy electrons. We will focus all the simulations on the high energy peak. Since electrons are accelerated in a small region with dimensions comparable to the laser waist, we will use a point-like electron source, the energy of which is distributed along a Gaussian shape with a width of 40 MeV (FWHM), centered at 170 MeV. The initial angular spread is chosen to be independent of the electron energy and corresponds to a Gaussian width of 10 mrad FWHM. A total of 10^5 electrons are used in the simulation. This value is lower than the measured number of electrons, which is about 3×10^9. This choice is a compromise between the time needed to complete the simulations and the statistical fluctuations. All output values are normalized with respect to the incident bunch charge. In order to obtain the dose for a single laser shot, one needs to multiply the normalized dose (in Gy/nC) by the charge of an electron bunch (0.5 nC). The following simulations are performed for a single shot, but our laser system can operate at 10 Hz.

In the simulations, the electrons are propagated in vacuum up to a water phantom, even if in practice the electrons will have to travel in the air up to the patient. Scattering in the air was studied in Ref. (DesRosiers et al., 2000). It appears that the beam spread in air after a propagation over 100 cm corresponds to an angular spread of 5.4 mrad FWHM for 200 MeV electrons. This value overestimates the spread at lower distances. If one assumes that a quadratic sum is representative of the convolution of the initial divergence with the spread in the air, we obtain a divergence of 11.4 mrad at 100 cm from the electron

source. This should be compared to the initial divergence (10 mrad). The conclusion of the article states that "For beams below 200 MeV, this distance should be not greater than 70 cm". We will neglect scattering in the air in this study.

We have computed the dose deposition profile in this water target. Its thickness was 40 cm and the transverse dimension was chosen to be much broader than the transverse spread of the electron beam. We plotted the dose distribution in a longitudinal plane from a 4 cm $\times$ 4 cm $\times$ 40 cm box, placed on the propagation axis (Oz), and divided in $100 \times 100 \times 100$ cells. The geometry of the simulation is shown on Fig. 4.8

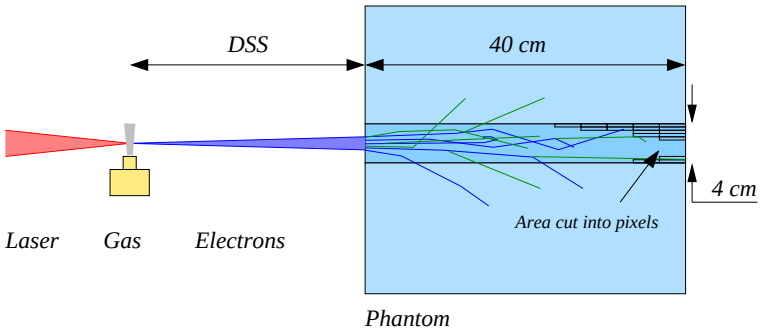

Figure 4.8: (Color) Geometry of the simulation.

4.2.2 Direct irradiation

The source to surface distance (SSD) has been set to 4 different distances : 15 cm, 30 cm, 60 cm, 100 cm. In the following, another geometry is discussed (Sec. 4.2.3) , where the electron beam is refocused using magnetic fields and which will be referred as SSD $= -30$ cm. The physical processes described by `Geant4` included discrete events (elastic scattering, photon production, ionization) and continuous energy loss (collisional and radiative stopping powers). The free parameter called `CutRange` was set to 100 μm. It describes the propagation range of secondary particles, thus requiring more computation time for lower values. The production of neutrons was studied in (DesRosiers et al., 2000), where they conclude that the relative biological effectiveness should be increased by a factor < 1.03 in order to account for neutron production and radioactivity. This point is not discussed here.

Dose distribution

Fig. 4.9 shows the isodose curves for this laser-plasma electron source. For each simulation, the following isodoses are represented : 0.1, 0.2, 0.5, 1, 2, 5, 10, 20, 50 Gy/nC. The dose distributions show a forward peaked pattern in depth, with a slight broadening due to the electron scattering. In the first 10 cm of the phantom, the shape of these curves strongly depends on the initial electron distribution. This effect is damped for larger depths in the phantom, where electron scattering leads to a similar dose profile in all cases. However, even for SSD of 100 cm, these isodoses remain relatively parallel to the central axis. For instance, the 0.1 Gy/nC curve extends up to 34 cm longitudinally

SSD [cm]	15	30	60	100	-30 (focused)
Peak dose value [Gy/nC]	61	18	4.7	2.0	20

Table 4.1: Dependence of maximum dose with the source to surface distance. The negative SSD corresponds to a configuration presented in Sec. 4.2.3

without exceeding 4 cm transversely. The value of the maximum dose increases as the SSD decreases, since the energy is concentrated in the width of the electron bunch impinging into the phantom, as seen in Table 4.1. Multiple scattering collisions occur during the electron propagation, explaining why the energy is distributed further laterally as the depth increases.

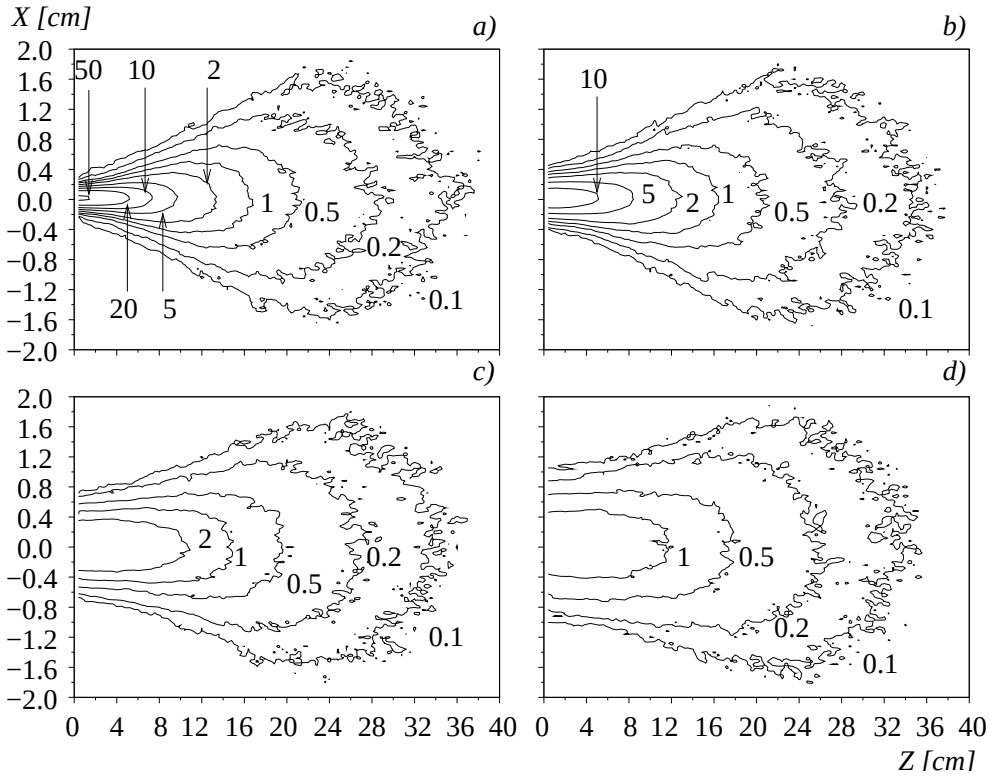

Figure 4.9: Isodose curves for different levels : 0.1, 0.2, 0.5, 1, 2, 5, 10, 20, 50 Gy/nC. The distance from source to surface is : a) 15 cm, b) 30 cm, c) 60 cm, d) 100 cm. The two axis are on a different scale.

Longitudinal and transverse dose profiles

The depth dose distribution integrated over the transverse direction is shown in Fig. 4.10. This curve is the same for all simulations presented here, since the angular distribution and the spectrum remain unchanged. It represents the longitudinal profile that would be obtained if a series of shots with small separation (compared to the transverse profile) irradiates the whole area to be treated. This curve has a broad peak around 20 cm from

the entrance. For a deep seated tumor (20 cm for instance), this electron beam provides a better sparing of tissues at risk when compared to conventional photon beams, for which the depth dose peak is located in the first 5 centimeters. The control of the central energy of this electron beam would allow to fit the position of the peak with the depth of the tumor. This peak is the consequence of several factors :

- the collisional stopping power for electron in water increases dramatically at low energy
- the secondary particles are emitted mainly in the forward direction and they will deposit their energy deeper in the medium
- the electron flow becomes less laminar as the depth increases. The electron track becomes curved and looses directionality at large depths, which increases the energy deposited at a given depth.

Due to an electron range larger than the thickness of the water phantom, one should obtain a dose signal over the whole depth of the phantom.

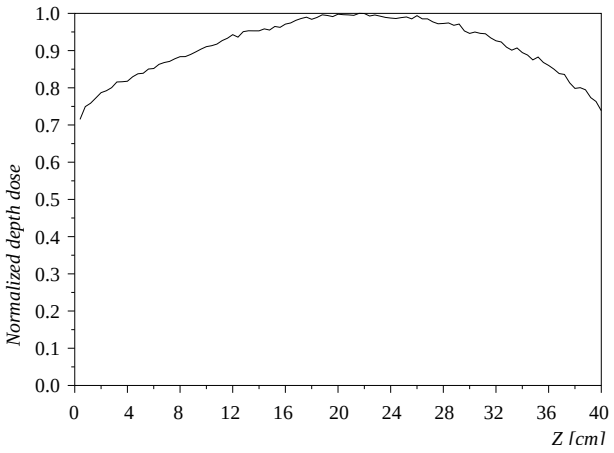

Figure 4.10: Integrated depth dose curve.

Fig. 4.11 shows the central-axis dose and the transverse profile at 10 cm depth for different SSD. Because of the lateral scattering, the electrons diverge from the central axis of the pencil beam, which explains the decreasing dose profile on central axis of Fig. 4.11a. Then, Coulomb scattering is mainly responsible for the quasi-Gaussian shape of the lateral profiles. The values of the lateral spread at various depths are given in Table 4.2. In this section, the lateral spread is defined as the radial distance between 90% and 20% of the maximum dose at a given depth, for a single shot. The width of the transverse profiles increases with depth and also with the SSD. This electron beam can deliver a high dose with sharp penumbra deep inside the tissues.

The values in Table 4.2 are difficult to compare with the study of DesRosiers *et al*, where their simulations use larger irradiation fields. This explains why we avoid using the term “penumbra” in this section, and prefer the word “spread”. We will introduce in Sec. 4.2.4 the numerical factor needed to simulate the penumbra width for a laterally broader irradiation field.

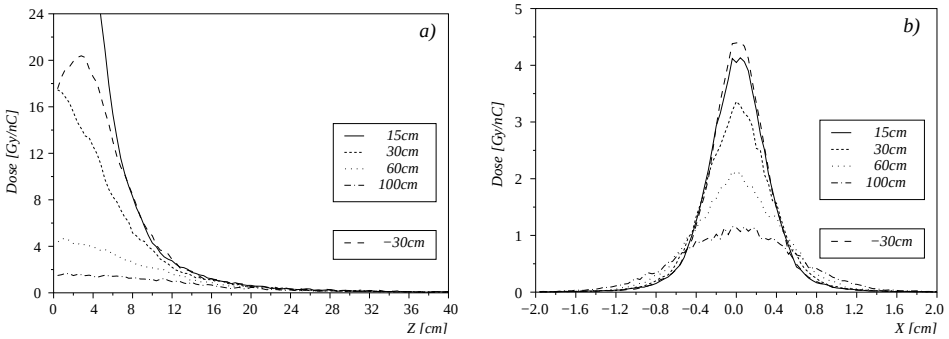

Figure 4.11: Dose profiles for all simulations : a) longitudinal along propagation axis, b) transverse at 10 cm depth for different source to surface distances.

SSD [cm]	15	30	60	100	-30 (focused)
Longitudinal Distance [cm]					
$R_{90\%}$	1.4	2.1	2.6	3.1	4.3
$R_{20\%}$	6.8	9.8	16	18	11
Transverse Spread [cm]					
at z=1 cm	0.10	0.18	0.36	0.57	0.17
at z=5 cm	0.16	0.23	0.40	0.63	0.18
at z=10 cm	0.36	0.41	0.53	0.73	0.35
at z=15 cm	0.65	0.67	0.77	0.97	0.61

Table 4.2: Longitudinal distance and transverse spread for a single shot. $R_{90\%}$ and $R_{20\%}$ represent depths of 90% and 20% of the maximum dose respectively, along the central axis. The transverse spread is defined as the radial distance between 90% and 20% of the maximum dose at a given depth. The negative DSS corresponds to a geometry discussed in Sec. 4.2.3. The unit is one centimeter.

As the distance to the water phantom increases, the initial lateral spread increases. In practice, the scale of the gantry, the shielding from radiation from the laser-plasma interaction point prevents from using short SSD. It would be interesting to study a modified electron distribution which would give similar or even better dose deposition profiles for larger distances from the laser-plasma interaction point. Using a magnetic system (typically a quadrupole triplet), it is possible to refocus an electron beam further. We will study this point in the next section.

4.2.3 Converging electron beam

One assumes that a compact magnetic field is applied on the electron beam in order to refocus it further. A cartoon with necessary items is shown on Fig. 4.12. In such conditions, the low-energy electrons can be removed with a compact 20 cm-long monochromator (optional), the electron beam can be refocused with a 20 cm-long quadrupole triplet and shielding can be added around the interaction point. A more compact system which combines the monochromator and the focusing system has already been presented for a proton beam (Fourkal et al., 2003). This idea can be extended to electrons. The geometry of this system won't be discussed here. The laser propagates up to the interaction point. Dangerous radiations are produced after the interaction, which means that shielding is necessary starting from this place. This system has to be small in order to fit in a treatment room. The geometry of the radioprotection won't be discussed here either. The studies carried out in the previous section are still valid if the electron beam is refocused outside the water volume. But now, it's also possible to focus inside the phantom.

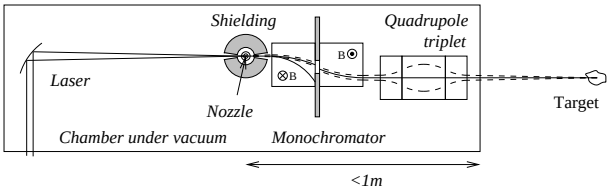

Figure 4.12: Drawing of a monoenergetic laser-plasma accelerator. The laser is focused using an off-axis parabolic mirror in a gas jet to accelerate electrons. The electron beam is filtered (by a monochromator) and refocused (using a quadrupole triplet) outside the chamber under vaccum.

The spectral width of the electron distribution leads to chromatic aberrations when is is refocused, i.e. electrons with different energies won't be refocused at the same distance. First, it is possible to decrease the spectral width with the monochromator. Second, the spectral width might be narrower because the measurement is limited by the spectrometer resolution. We have measured other spectra even narrower (see Fig. 2.8). In this last simulation presented here, one neglects the chromatic aberration which depend on the geometry of the magnetic system used. An achromatic magnetic system has already been studied (Raischel, 2001). The electron beam is set to refocus at position $z = 30$ cm without phantom. The magnification factor is -1, which means that the spatial distribution at the surface of the phantom is the same as in the diverging 30 cm case. The electron beam still propagate in vacuum.

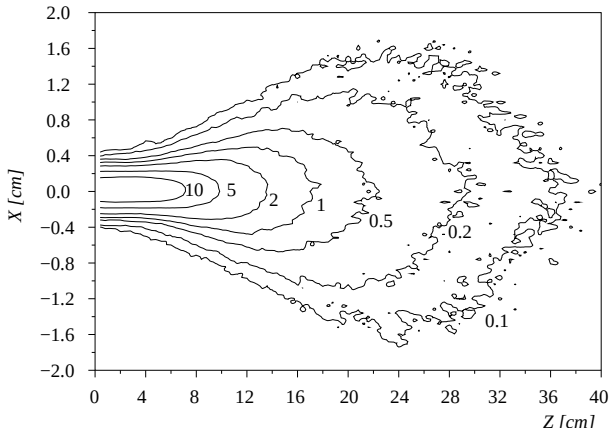

Figure 4.13: Isodoses for the electron beam focused at position $z = 30$ cm in a water target with divergence of 10 mrad (FWHM). The two axes are not on the same scale.

As expected, the maximal dose is higher when electrons are refocused in the target (20 Gy/nC in Table 4.1). The position of this maximum is now shifted to 2.9 cm inside the phantom. The dose deposition at this depth is now higher than in the diverging case (14 Gy/nC at 2.9 cm). Figure 4.11a shows the dose along the central axis of this simulation. One notes that the two curves start at the same level. Over the first 6 cm, the focusing effect is balanced by the scattering. The electron flux is more concentrated along the axis, as shown in Table 4.2. Consequently, the dose along the central axis doesn't fall as fast as in the diverging case, but rather shows a peak in depth in the phantom. Actually, the longitudinal and transverse dose distributions are similar to values obtained in the diverging case for an SSD of 15 cm.

In this configuration, the transverse gradient length evolves slower than in the diverging 30 cm case (see Table. 4.2) and the isodoses remain parallel to the central axis during the first 6 cm (compare Fig. 4.13 and Fig. 4.9b). This allow a better control of the exposure of tissues at risk in the neighborhood of the area under treatment. The angular distribution mainly affects the shape of the isodoses. The effect of the initial divergence is damped after a short propagation in the medium. This scattering also reduces the impact of chromatic aberrations.

4.2.4 Discussion

Regarding the use of one single electron bunch, the focusing of the electron bunch would be useful for stereotactic radiosurgery of subcentimetric lesions, such as cerebral arteriovenous malformations or metastasis, located at depths distal to 10 cm, since the energy deposition is concentrated very locally around the central axis of the spot.

From the results presented above for a single bunch of electrons, it is possible to study the adequacy of the dose distribution for laterally broader irradiation fields, more likely to be applied for clinical use. In the following, we discuss the potential of VHE laser-accelerated electrons scanned laterally in order to irradiate larger fields. Simulations showing multi-beam configuration will be presented elsewhere. The aim is to achieve high

homogeneous dose profiles in the target volume and steep gradients at the field edges in order to spare normal tissues and organs at risk, i.e. narrow lateral penumbrae are needed in depth. We recall that for one single bunch of electrons, quasi-Gaussian lateral dose profiles were found, with standard deviation at a given depth denoted σ. This standard deviation is obtained from Table 4.2 by dividing the transverse spread by 1.33 . This implies that in order to achieve homogeneous lateral dose profiles at that depth, we have to assume that

- the interval between the spots is lower than the σ of the dose kernels
- the lateral extent of the field should exceed 3.5 times the σ of the dose kernels.

Under these conditions, a lateral electronic equilibrium along the central axis of the beam can be achieved, and a high dose can be homogeneously applied over the lateral extent of the target volume.

Since the σ of the electron dose kernel increases with depth, the shape of the central axis dose distribution is expected to be strongly dependent on the size of the field. In particular one should expect the dose along the central axis to drop faster at larger depths for decreasing field sizes. This effect can be observed in the study of DesRosiers *et al* for 1 cm and 5 cm field radii.

One can estimate, for a given depth, the size of the field necessary to achieve a flat lateral dose profile and also the width of the corresponding 90%-20% lateral penumbra. This penumbra, corresponding to the convolution of this gaussian distribution with a heaviside function (to reproduce the semi-infinite irradiation field), is obtained by multiplying σ by the convolution factor 2.12 . We find a σ of about 0.31 cm for a SSD of 30 cm, at 10 cm depth, which would lead to a width of the lateral penumbra of about 0.65 cm, provided that the field size exceeds 1.1 cm radius. These estimations are in agreement with the results of DesRosiers *et al*, although their study was performed for VHE electrons having a narrower initial energy spread than our experimental beam. They obtained, for instance, a lateral penumbra of 0.69 cm at 10 cm depth using 200 MeV electrons. This analysis shows that one should expect for the dose distributions resulting from scanned VHE laser-accelerated electron beams lateral penumbrae whose widths are in the same order of magnitude than those from 15 MV photon beams.

Here is an estimation of the treatment speed. For a 5 cm $\times$ 5 cm irradiation field, this makes a total of 256 positions on a grid with a distance of 0.31 cm between two consecutive shots. Provided that the accelerated charge is reduced to deliver every shot the required dose established from the treatment planning (typically 1.8 - 2.2 Gy), the irradiation would last 26 seconds. The tuning of the dose deposition can be operated by selecting more or less electrons in the monochromator or by adjusting the interaction parameters.

The dose deposition profile for a SSD of 100 cm is also interesting from a clinical point of view : it provides an important dose deep in the volume (1 Gy/nC), with a moderate energy deposition at the entrance of the phantom (max of 2 Gy/nC). These values are closer to the requirements of radiotherapy. The distance between two consecutive shots becomes larger ($\sigma = 0.55$ cm), which makes the treatment faster, but the lateral penumbra for a semi-infinite irradiation field also becomes larger (1.2 cm at 10 cm depth). This configuration is adapted if there is no sensitive tissue in the vicinity of the region under treatment.

The same analysis can be performed for the focused electron beam. The main difference is that the width of the lateral dose distributions is significantly decreased at 10 cm depth. In order to get an homogeneous dose coverage of the tumor target volume by scanning, the interval between the beam spots needs to be reduced. However the big advantage is that increased lateral gradients are obtained at the field edges. In particular one would get a lateral penumbra of 0.55 cm for the scanning of the focused electron bunch in comparison to 0.65 cm for the unfocused one.

An important point of discussion is the large dose rate delivered by one single bunch of VHE laser-accelerated electrons. For instance, in the focusing 30 cm case we have a maximum dose of 10 Gy in a single laser shot (20 Gy/nC and 0.5 nC/shot). The values obtained for a single shot are far above the conventional dose applied during a treatment (typically 1.8 to 2.0 Gy). However, it is possible to control and reduce the number of accelerated electrons by adjusting the interaction parameters (laser energy, pulse duration, electron density, ...), as shown in Chapter 2. For instance, by decreasing the electron density to 3×10^{18} cm^{-3}, we were able to produce a VHE electron beam having a similar spectral quality but with a ten times lower charge. The noise level prevented detection of lower charge at even lower electron densities. The main difficulty that remains concerns the stability of the electron beam from shot to shot. This issue is being studied currently by all research groups working in this field. Because the fluency is very high, additional studies are necessary to determine if biological effects depends on the bunch duration.

Therefore, we believe that VHE electron beams produced by laser-plasma interaction could have a clinical potential, at least for similar indications as those treated by high-energy conventional photons. Further studies are currently in progress to extend the present dosimetric study and to investigate in detail the feasibility of scanned VHE laser-accelerated electrons for intensity-modulated radiation therapy.

In practice, the fast evolution of laser technology leads to a reduction of the size and cost of the laser system. The safety is also increased because the laser light can propagate from the laser facility up to the interaction point without needing any shielding, which will be located mainly after the interaction point. One may also manipulate the electron beam, filter it and refocus it, with a magnetic field to improve the dose deposition properties. This compact laser system is expected to be of interest when the overall dimensions are restricted by the room volume. Since the electron beam direction follows the laser propagation axis, the point scanning technique can be achieved by moving the final focusing optics and the nozzle (in a gantry).

Since this electron source is pulsed, the radiotherapy could be combined with a detection of motion in tissues, to improve the quality of the exposure. Many studies are currently being done in the field of adaptive radiotherapy.

4.3 Application to femtolysis[1]

The interaction of an electron beam with matter induces molecular damage often irreversible. Thus, the irreversible effects of ionizing radiation were the main topic of the previous section, dedicated to destruction of cancerous cells. During their interaction with biological media, the ionizing radiation (photon or particles) induce early physico-

[1] contraction of **Femto**second radio**lysis**

chemical transformations. These ultra-fast radical events, which take place on a very short time ($10^{-14} - 10^{-10}$ s), are responsible for molecular, cell or tissue damages observed on long time scales (second, day, month). The understanding of these radical events requires spectroscopic studies with an ultra-high temporal resolution (Gauduel and Rossky, 1994; Gauduel et al., 2000).

With FWHM of 3 to 10 ps (Kozawa et al., 1999; Wishart, 2001; Belloni et al., 2005), the temporal characteristics of pulsed electron sources, obtained by conventional linear accelerators (Linac), are a real limitation to the study of ultra-fast radical events. New opportunities appear with electrons beams produced during laser-plasma interaction and which provide electron bunches shorter than 100 fs. The study in real-time of radical events induced by by the interaction of relativistic particles with media of biological interest becomes accessible. The knowledge acquired during the last years in radical femtochemistry of low energy (¡ 10 eV) in liquid phase (Gauduel et al., 1998, 2000) are essential to start femtochemistry of high energy ($\sim$ MeV). The project Water Femtolysis, the solvent of life, which is developed at LOA, aims at this better understanding.

The initial work has began before I started my PhD. However, I present a brief summary of some results (Gauduel et al., 2004; Brozek-Pluska et al., 2005) which concern the development of high-energy femtochemistry in liquid phase, when using an electron beam from a TW laser.

For a better understanding of early damages induced by ionizing radiation on water molecules, time-resolved absorption spectra have been recorded. One of the goals is to understand the coupling between secondary electron and liquid hole induced in the formation of the OH radical and the hydronium ion (hydrated proton). Due to a high oxidizing potential, the OH radical has a major role in radiobiology, radiotherapy and radio-induced cell destruction.

The experimental setup is shown on Fig. 4.14. An off-axis parabolic mirror (a) with focal length of 30 cm was used to generate and electron source with energies below 15 MeV (b) in a gas jet with electron density 1×10^{19} cm^{-3}. The spectrum (c) is represented by a maxwellian distribution of temperature 4.5 ± 0.5 MeV. In order to reduce the direct influence of the laser beam and in order to limit the perturbation of the liquid medium by low energy electrons (¡ 2 MeV), a 1 mm-thick copper foil (d) was inserted between the electron source and the water target (e). The angular distribution of the electron beam was recorded separately on a stack of radiochromic films, spaced by copper foil to slow down electrons and to select the energy range recorded by each sensitive radiochromic film.

An infrared probe of duration 30 fs, centered at 820 nm and having spectral width of 40 nm (FWHM) allows the analysis of s-p transition of secondary electrons removed from their water molecule by relativistic electrons, and stabilized by interaction with these molecules. The hydrated electron with a configuration of type s, represents the most reducing potential elementary radical of the water molecule. The understanding of its early coupling with the OH radical and the hydronium ion H_3O^+ is studied in the frame of the Femtolysis project.

The intensity of the probe pulse was below 10^{-3} J cm^{-2} in order to neglect the direct excitation of the medium. The signal was measured on a high dynamical range CCD camera (16 bits) (f). A delay line allows a precise control of the delay between the electron bunch and the absorption signal. Another advantage of laser-plasma interaction is the perfect synchronisation of the excitation by the electron beam and the optical reading

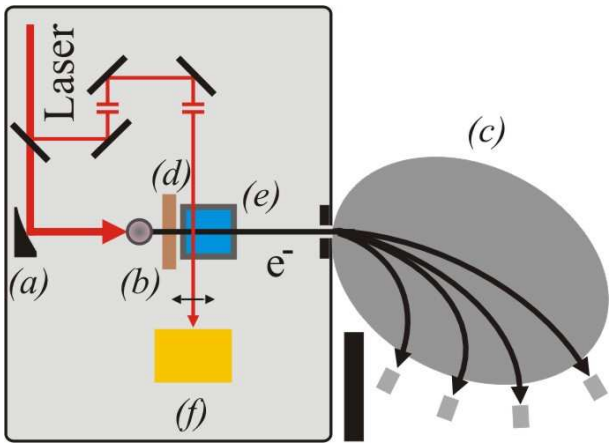

Figure 4.14: (Color) experimental setup for the radiolysis experiment. The electron beam excites water molecules at 294 K. The variation in absorption of a 30-fs long laser pulse is measured on a high dynamic-range CCD camera. The delay between excitation and optical reading is controlled by a delay line.

by the infrared probe. The absorption signal is represented on Fig. 4.15. This curve is obtained by comparing the measured signal with and without the electrons along the line of sight intercepted by one pixel. One obtains an absorption signal which reaches a maximum 3.5 ps after the excitation and which decays on longer time scales.

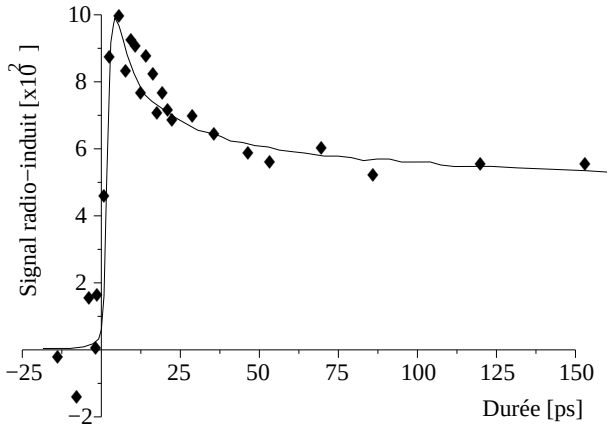

Figure 4.15: Absorption signal for different position of the delay line. Each dot corresponds to an average over several shots.

The analysis of this signal is rather complex because the excitation and the measurement are done along perpendicular axis. It means that electrons continue propagating while reading the absorption signal. Thus, the measured signal contains the individual absorption response taken at different times. One measures actually the convolution between the unique sample and the response functions of the experimental setup. After estimating the global convolution functions of the electron beam and the measurement itself, the absorption signal for a single sample after its excitation is obtained by deconvolution.

The amplitude of the absorption signal gives the average density of solvated electrons produced. The primary radiolytic yield Ge^{-}_{hyd} has been estimated to 6.8 ± 0.5 molecules / 100 eV at time 3.5 ps (Brozek-Pluska et al., 2005). This yield is expressed per unit of dose, which is estimated to 15.5 ± 1 Gy on the axis by Monte-Carlo method. The authors insist on the fact that this yield is higher than the predictions from stochastic models of water radiolysis (Pimblott and La Verne, 1998; Muroya et al., 2002) for which data are extrapolated from much longer time scales. Quantum systems involved on such short time scales are more complex than those used up to now to describe the evolution of this elementary radical.

These preliminary experimental data show that these numerous evanescent quantum systems have to be taken into account to reproduce the absorption curves at short interaction times. The ionization trajectories of the water molecules leading to hydration of secondary electrons and the generation of OH radicals useful for radiotherapy occurs in spurs during the prethermal regime ($\sim 10^{-13} - 10^{-12}$ s).

Complementary studies are necessary to confirm the values of all the free parameters in such systems. However, the innovative aspects of the Femtolysis project for radiobiology and its potential applications in radiotherapy are the results of synergy between experiments in high-energy femtochemistry and spatio-temporal predictions in ionization spurs obtained using numerical simulations based on quantum chemistry methods.

4.4 Application to the generation of X-ray radiation (betatron mechanism)

The laser-plasma accelerator can be used to generate a broad-band, collimated and energetic X-ray source. The generation of this radiation is based on the oscillations of the electron bunch around the central axis of the ionic channel, created by the laser. In other words, electrons undergoing an acceleration will emit radiation (Jackson, 1925). The electric fields that bend the electron trajectory are so intense that this radiation extends to the X-ray domain (a few keV, subnanometer wavelength). I point out that in section 3.1, we have studied the oscillations of the isocenter of the electron beam. Even without such oscillations of the center, individual oscillations of the electrons still exist.

The mechanism responsible for the generation of the synchrotron radiation has been studied for laser-plasma interaction (Whittum et al., 1990; Esarey et al., 2002; Kiselev et al., 2004). This radiation has been measured at Laboratoire d'Optique Appliquée by A. Rousse's team (Rousse et al., 2004; Ta Phuoc et al., 2005). This X-ray source is different from other existing sources : the generation of high order harmonics is limited to wavelength of the order of 10 nm. The generation of radiation using K-α sources allows to reach subnanometric wavelengths, but their emission occurs in 4π steradians which limits its application.

The experimental setup is shown on figure 4.16. After the interaction, electron trajectories are bent using a magnetic field (0.3 T over a length of 20 cm). A beryllium filter cut radiation below 1 keV. The radiation profile is measured directly on axis by an X-ray CCD camera, placed at 50 cm from the interaction point. The sensitivity of this camera limits the observation of X-rays to energies below 10 keV. The divergence of the radiation is estimated to 50 mrad (FWHM) in this spectral range. The radiation spectrum is estimated

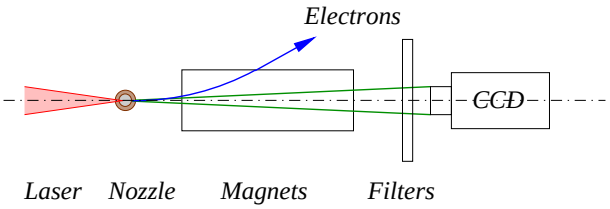

Figure 4.16: Experimental setup for the measurement of X-ray created by betatron mechanism.

by inserting different filters in front of the CCD. Measurements have been done with 25 μm beryllium (1-10 keV), and adding either 40 μm-thick aluminium filter (4-10 keV) or a 25 μm-thick copper filter (6-10 keV). This is represented on figure 4.17. Taking into account the spectral shape, the authors estimate the number of photons to exceed 10^8 per shot, per steradian and in 0.1% bandwidth. This value corresponds to the optimal electron density for the generation of synchrotron radiation, which is $n_e = 10^{19}$ cm^{-3} in 3 mm of helium gas. This optimum is correlated to the quality of the electron source. Below this density, the number of electrons drops fast, which also descreases the X-ray signal. For higher electron densities, the X-ray signal also drops because the electron beam quality degrades : the number of electron at high energy decreases, the divergence of the electron beam increases.

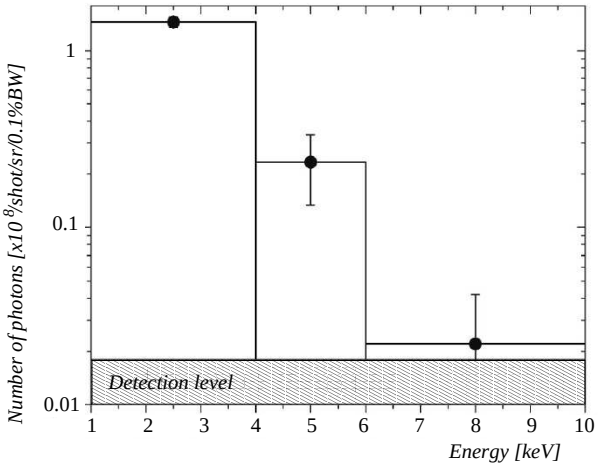

Figure 4.17: X-ray spectrum using different filters.

In conventional structures, this radiation is generated when the electron beam passes though an undulator, composed of magnets with alternative polarity. But the forces which act on the electron beam in laser-plasma interaction are much higher than the forces from the magnets. Thus, the oscillation wavelength is shorter and the X-ray emission spectrum extends towards higher energies. The compactness of such system is an asset. The number of photons also depends on the number of oscillations in the structure and a longer interaction length might be necessary to increase the intensity of the radiation.

Such a source can be used for time-resolved X-ray diffraction experiments, for absorp-

tion experiments and X-ray spectroscopy experiments. The use of this electron source for coherent amplification of X-ray radiation (XFEL) is currently being investigated. Finally, the generation of X-ray radiation by Thomson scattering on a second laser pulse is also being studied in the laboratory.

Conclusion and perspectives

Conclusion

The interaction of an ultra-intense and ultra-short laser pulse with a gas jet allows the production of an electron beam with original properties. By adjusting the parameters of the interaction, a quasi-monoenergetic electron beam has been obtained experimentally after an acceleration length of 3 mm. This beam is energetic, collimated and with a short initial duration. The charge contained in the bunch is about a hundred of pC. The detailed dependency of the properties of the electron beam with interaction parameters has revealed the important role of self-focusing effects and pulse shortening. Particle simulations show that these processes leads to the creation of a cavity behind the laser pulse, where the acceleration takes place. Electrons that are trapped have similar injection properties and undergo the accelerating field of the plasma wave without being disturbed by the transverse electric field of the laser. In such conditions of interaction, the electron beam obtained is quasi monoenergetic.

These properties have been obtained is a narrow range of parameters. For laser parameters, the lengthening of the laser pulse makes the electron beam immediately vanish. The decrease of the laser energy shows that the electron density has to be increased to recover the electron beam. The modification of the aperture of the focusing optics reveals that the electron beam is less energetic when the laser is tightly focused. Numerical studies are currently being done to explain this trend. For plasma parameters, the increase of the electron density breaks the spatial quality of the electron beam. It becomes polyenergetic, with a maxwellian spectrum and a larger divergence. At lower density, we have also obtained a quasi-monoenergetic spectrum but the charge drops quickly. Statistics of the electron beam were also shown to reveal the difficulty to obtain quasi-monoenergetic spectra in a reproducible way.

Finer structures of the electron beam have been observed and interpreted using physical models. The electron beam has structures at the laser wavelength and at the plasma wavelength which have been observed using coherent emission of radiation at a metal-vacuum interface. Independently, a correlation between the output angle and the electron energy has been measured and attributed to betatron oscillation during the propagation of the beam. Finally, the properties of the transmitted laser have also been measured. Using a single shot autocorrelator, we have shown a temporal shortening of the laser pulse, signatures of non-linearities in the propagation of the pulse. This interaction gives not only an electron beam with unique properties but also a very short laser pulse (10-14 fs) after being filtered by the plasma. No other method is known yet to generate such short laser pulses containing such a large energy (efficiency of 20%). The measurement of the

transmitted laser energy allows the estimation of the fraction of energy transmitted to the plasma waves as function of the electron density.

The electron spectrometer developed and used during this thesis is described in detail. Analytical formulas are summarized and the expression for the dispersion has been used to build two new spectrometers, the resolution of which are adapted to higher electron energies for future experiments. Two independent methods have been used to determine the amplitude of the spectrum. The first one is based on the normalization to the charge measured by an integrating current transformer. The second one is the absolute calibration of the scintillator. The efficiency of the scintillator is extrapolated from measurements done on a conventional pulsed accelerator. Results obtained with these two methods differ and the mismatch is finally attributed to a parasited signal from the ICT despite numerous test to get rid of electromagnetic noise.

These electron beams are currently produced by laser systems working at high repetition rate (10 Hz), which is an asset for applications. With present technological evolution, a 100 TW laser system is affordable (a few millions euros) and should allow to reach 1 GeV. Industrials also develop compact laser systems adapted to university labs or hospitals. In order to promote the properties of this source, the group Particle Sources by Laser has always looked for new applications.

A γ-ray radiography experiment has been carried out in collaboration with the team from CEA DAM Île-de-France. This non-destructive inspection approach has allowed the visualization of small-scale details and the resconstruction of the radial profile of the object. Thanks to submillimetric resolution of this secondary radiation source, high quality images have been obtained.

The dose deposition of a quasi monoenergetic electron beam in a water volume has been simulated using Monte-Carlo technique to show the interests of such a source for radiotherapy. During this collaboration with the team from DKFZ, we have shown that such a treatment could compete with those done by conventional techniques. Contrary to previous studies on laser-plasma interaction, the available dose is now adapted to the treatment which leads to a reasonable treatment time.

The application of short electron sources to water radiolysis, perfectly synchronized with the probe beam for the measurement, allows to probe subpicosecond time scales, which is not accessible with classical methods.

Finally, betatron oscillations performed by the electron during their acceleration also generates an energetic, collimated X-ray flash adapted to diffraction or absorption studies.

Perspectives

It has been shown that the electron beam produced has a high spatial and spectral quality. The charge density is high and the repetition rate is useful for applications. The applications developed during this thesis aim at showing the relevance of this source directly in medicine for new treatments. For this, dose simulations have been performed. The following part of this study should be the exposure of a phantom to visualize this dose deposition profile. For biology and short time scales femtochemistry, the significant improvement of the divergence of the electron beam leads to a better temporal resolution for the femtochemistry experiment. A new experimental campaign should emphasize the

importance of transient quantum states. This study of the behaviour of matter irradiated by ultra-short dense energy deposition is a new field and I am convinced that this accelerator will be a precious tool for many studies in this field. Moreover, this primary electron source can be used to generate secondary γ-ray sources for non-destructive inspection of dense objects and the high-resolution visualization in car industry or also the motion of fast objects in aeronautics In the X-ray domain, the oscillations of the electron beam produce a broad-band, intense, collimated and short X-ray radiation which will be used in absorption experiments and time-resolved spectroscopy measurements. Then, studies are carried out to inject this electron beam inside classical undulators to amplify coherently the X-ray radiation (XFEL).

Developments are being done to increase and stabilize the energy of the electrons. Two methods exist to increase the electron energy : either by extrapolating this acceleration regime to even higher laser intensities and energies, over longer acceleration lengths, or by injecting this first quasi monoenergetic electron bunch into a linear accelerating structure (acceleration in two stages). The guiding of laser pulses can be used to increase the interaction length.

In addition to the increase of the electron energy beyond 1 GeV, efforts must also be done to stabilize the beam. The acceleration in a linear stage allows a direct control of the average energy of the electrons and the spectral width of the distribution. Studies are performed to enhance the control of the electron injection. The electron beam obtained during this thesis has the required properties as an injector : it has to be ultra-short, so that all electrons experience the same accelerating field, it must deliver an important charge and its must have good spatial (spatial) and spectral (monochromaticity to transport of the second stage) qualities. Then, the use of a second counter propagating laser can also control the injection time in the plasma wave initially below the wavebreaking limit.

Our experimental conditions were very close to this transition where quasi-monoenergetic structures appear and this interaction can naturally stabilize above this threshold. Some theoreticians call this an asymptotic convergence towards higher intensities (Gordienko and Pukhov, 2005). Current laser developments also lead to more stable systems, which should decrease shot-to-shot fluctuations linked to non-linear mechanisms and therefore to initial fluctuations of the interaction. This initial self-focusing section in the density gradient of the gas jet is crucial and requires additional studies.

The large number of petawatt-class laser systems currently being built all around the world are evidence of this international competition. Big projects are currently being built in Europe, in the field of laser-plasma interaction at very high intensity among which I can cite those in which Laboratoire d'Optique Appliquée is involved : the project Propulse, consortium of research laboratories, companies and physicians, aims at the production of high-energy protons for medical applications. The project XFEL (acronym for X Free Electron Laser) wants to produce intense coherent X-ray radiation with an electron beam. Finally, the project ELI (acronym for Extreme Light Infrastructure), lead by our director Gérard Mourou, will be a large-scale infrastructure to address the need for more powerful systems for many research topics concerning laser-plasma interaction at ultra high intensity.

Appendix A

Betatron oscillation model

This appendix contains an analytic model describing the betatron oscillations of a relativistic electron also undergoing a constant longitudinal force.

A.1 Analytical equations

Here are the equations of motion for a relativistic electron in a constant longitudinal field and a linear radial restoring force (which leads to oscillations) (see Fig. A.1).

Assumptions of the model are :

- The acceleration length is much less than the dephasing length (in order to consider a constant accelerating field).
- The electron is injected at radius r_0, with an initial energy $\gamma_0 mc^2$, and an initial velocity parallel to the propagation axis.
- One considers small oscillation angles (paraxial approximation) $v_r \ll v_z$.

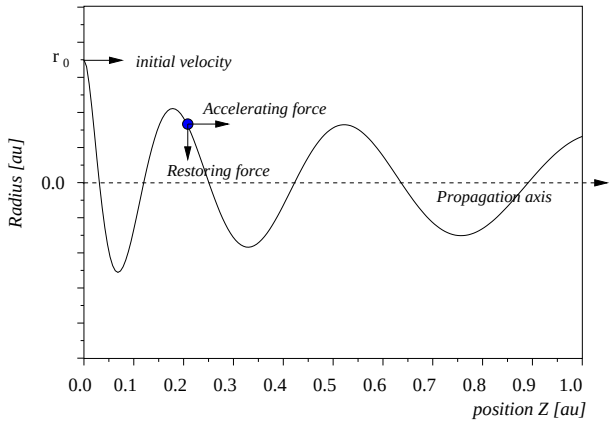

Figure A.1: Example of trajectory for an electron undergoing a linear radial restoring force and a constant longitudinal accelerating force.

The electron undergoes a force $\vec{F}$

$$\vec{F} = eE_z\vec{e}_z - \frac{m\omega_{pe}^2}{2} r\,\vec{e}_r \tag{A.1}$$

In order to simplify, I set $E_z > 0$ to avoid any confusion in the final equations. The equation of motion for a relativistic electron in this field is

$$\frac{d}{dt}(\gamma m\vec{v}) = \vec{F} \tag{A.2}$$

One projects this equation along the two axis

$$\frac{d}{dt}(\gamma v_z) = \frac{e}{m}E_z \tag{A.3}$$

$$\frac{d}{dt}(\gamma v_r) = -\frac{\omega_{pe}^2}{2} r \tag{A.4}$$

The first equation A.3, describes the energy gain in the accelerating field

$$\gamma v_z - \gamma_0 v_{z0} = \frac{e}{m}E_z t \tag{A.5}$$

Using the assumption of small oscillation angles, one has $v_z \sim \beta c$, which gives

$$\gamma\beta = \frac{eE_z}{mc}\, t + \gamma_0\beta_0 \equiv a\, t + b \tag{A.6}$$

The second equation in the system A.4 contains all the physics of the oscillations

$$\frac{d}{dt}(\gamma v_r) = \dot{\gamma} v_r + \gamma \dot{v}_r = -\frac{\omega_{pe}^2}{2} r \tag{A.7}$$

Introducing a new variable $d = \omega_{pe}^2/2$, equation A.7 can be rewritten as follow :

$$(a\, t + b)\, \ddot{r} + a\, \dot{r} + d\, r = 0 \tag{A.8}$$

The solution of such a differential equation is not trivial. For $r(0) = r_0$ and $\dot{r}(0) = 0$ the solution is :

$$r(t) = \frac{\pi\sqrt{db}}{a} r_0 \left[\mathrm{J}_1\left(2\sqrt{db}/a\right)\ \mathrm{Y}_0\left(2\sqrt{d(b+at)}/a\right) - \mathrm{Y}_1\left(2\sqrt{db}/a\right)\ \mathrm{J}_0\left(2\sqrt{d(b+at)}/a\right)\right] \tag{A.9}$$

where J_0 and J_1 are Bessel functions of the first kind of order 0 and 1 respectively, Y_0 and Y_1 are the Bessel function of second kind of order 0 and 1 respectively.

Using the approximation of small angles, one has $\theta \approx v_r/v_z \approx v_r/c$. Then, the angle relative to the propagation axis is

$$\theta(t) = -\frac{\pi d\sqrt{b}}{a\sqrt{b+at}} \frac{r_0}{c} \left[\mathrm{J}_1\left(2\sqrt{db}/a\right)\ \mathrm{Y}_1\left(2\sqrt{d(b+at)}/a\right) - \mathrm{Y}_1\left(2\sqrt{db}/a\right)\ \mathrm{J}_1\left(2\sqrt{d(b+at)}/a\right)\right] \tag{A.10}$$

Using the physical variables and using Eq. A.6, this becomes

$$\theta_{E_z}(t) = -\theta_0 \frac{E_0}{E_z}\sqrt{\frac{\gamma_0\beta_0}{\gamma\beta}}\left[\mathrm{J}_1\left(\frac{E_0}{E_z}\sqrt{2\gamma_0\beta_0}\right)\ \mathrm{Y}_1\left(\frac{E_0}{E_z}\sqrt{2\gamma\beta}\right)\right.$$
$$\left. -\mathrm{Y}_1\left(\frac{E_0}{E_z}\sqrt{2\gamma_0\beta_0}\right)\ \mathrm{J}_1\left(\frac{E_0}{E_z}\sqrt{2\gamma\beta}\right)\right] \quad \text{(A.11)}$$

where $E_0 = mc\omega_{pe}/e$ and $\theta_0 = \dfrac{\pi\omega_{pe}}{2c}r_0$

One can try to simplify this equation by adding additional assumptions. If one assumes that $\sqrt{2\gamma_0\beta_0}E_0/E_z \gg 1$, then one can use the following equivalents

$$\mathrm{J}_0(x) \to \sqrt{\frac{2}{\pi x}}\sin(x+\pi/4)$$
$$\mathrm{J}_1(x) \to \sqrt{\frac{2}{\pi x}}\sin(x-\pi/4)$$
$$\mathrm{Y}_0(x) \to -\sqrt{\frac{2}{\pi x}}\cos(x+\pi/4)$$
$$\mathrm{Y}_1(x) \to -\sqrt{\frac{2}{\pi x}}\cos(x-\pi/4)$$

$$\theta_{E_z}(t) = -\frac{\theta_0}{\pi}\frac{(\gamma_0\beta_0)^{1/4}}{(\gamma\beta)^{3/4}}\sin\left[\frac{E_0}{E_z}\left(\sqrt{2\gamma\beta}-\sqrt{2\gamma_0\beta_0}\right)\right] \quad \text{(A.12)}$$

Equation A.12 shows that the amplitude of the oscillations decreases because of the acceleration to relativistic energies. Here, the equation of motion is described by three parameters : the amplitude of the oscillations (controlled by θ_0), the frequency of the oscillations (controlled by E_z) and the phase of the oscillations (linked to the injection energy γ_0).

Without accelerating electric field ($E_z = 0$), one obtains the usual equation of oscillation with frequency $\omega_\beta = \omega_{pe}/\sqrt{2\gamma_0\beta_0}$, which is commonly used to describe betatron oscillations.

A.2 Optimisation of parameters

In this section, we use Figure 3.1 from section 3.1.

The injection energy can be estimated using simple arguments. In the bubble regime, the injection is localised at the back of the bubble. If one refers to the separatrix introduced in Sec 1.2.3, one sees that the injection energy to enter the separatrix is equal to the Lorentz factor associated to the plasma wave : $\gamma_0 = \gamma_p \sim \omega_0/\omega_p$. The electron has to travel longitudinally at the speed of the plasma wave to be trapped. Recent studies (Lu et al., 2006b) have also taken into account the speed of erosion of the laser, which decreases its group velocity and therefore the velocity of the plasma wave. Consequently, the injection energy becomes :

$$\gamma_0 = \frac{\omega_0}{\sqrt{3}\omega_p} \quad \text{(A.13)}$$

For an electron density of $n_e = 6 \times 10^{18}$ cm^{-3}, one obtains $\gamma_0 \sim 9.5$. There remain two parameters : θ_0 and E_z.

Let's justify now the assumption made to simplify the asymptotic expressions of the Bessel functions. Here is a fast estimation for an electric field E_z of 100 GV/m and a plasma frequency of 1.4×10^{14} rad/s. Then, $\frac{E_0}{E_z}\sqrt{2\gamma_0\beta_0}$ gives 10.4, which holds the assumption $\frac{E_0}{E_z}\sqrt{2\gamma_0\beta_0} \gg 1$ a priori. One can check a posteriori that this assumption is still valid when the optimization is finished.

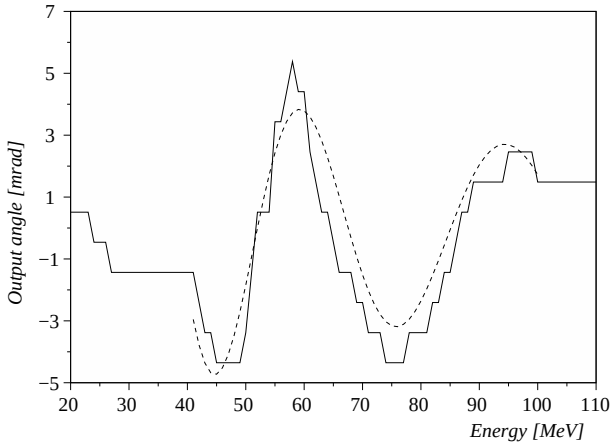

Figure A.2: Optimization of the parameters from eq. A.12 to the experimental data with following parameters : $\theta_0 = 0.25$, $E_0/E_z = 1.6$. (solid line) experimental data, (dashed line) optimization.

Optimal parameters are $E_0/E_z = 1.6$ and $\theta_0 = 0.25$. Knowing the electron density, we obtain the accelerating field $E_z = 150$ GV/m. Such an accelerating field is plausible because it corresponds to values reporter in equivalent PIC simulations (Tsung et al., 2004). One can express the injection radius from θ_0 which equals $r_0 = 0.35$ μm which is well below the size of the cavity.

This model can be criticized and/or refined. In reality the electric field is not constant, the injection is not necessarily parallel to the propagation axis but this leads to much more complex equations. This model contains the essential features to explain such an electron spectrum : an accelerating force and a restoring force which triggers the oscillations. Values obtained are consistent with the physical process. One still has to understand what triggered such oscillations of the mean direction of the electrons as function of the energy. It might be possible that an asymmetric laser field leads to an asymmetric injection, or that the laser axis has shifted during propagation.

Appendix B

Description of the electron spectrometer

In this appendix, I give analytic formulas and experimental work carried out to characterize this detector. This whole study was used to design two new and larger spectrometers, one being designed to see electrons accelerated to 1 GeV. Many other teams working in laser-plasma field also use this kind of detector

B.1 Experimental setup

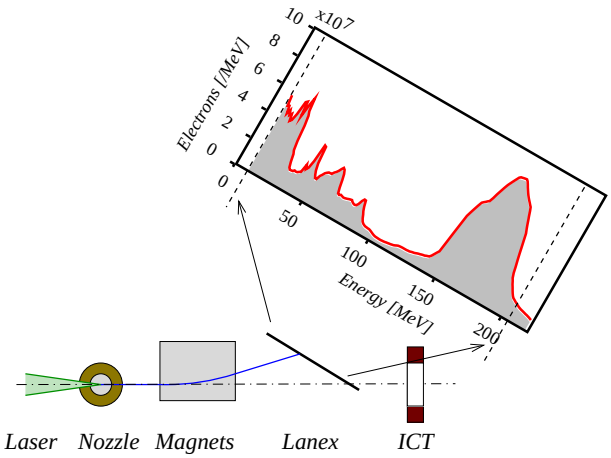

Figure B.1: (Color) Experimental setup used to measure the electron spectrum.

Figure B.1 illustrates the detection setup. Electrons coming from the plasma are dispersed while they travel in the magnetic field and then hit the scintillator. We image the surface of the scintillator on a CCD camera with large dynamical range (16 bits). The relaxation radiation emitted by the atoms from the scintillator is recorded to monitor the electron spectrum along the horizontal axis and the divergence along the vertical axis. The charge can be estimated using the ICT, center on the laser axis. We measure this way the number of electrons collected by this device after dispersion. This corresponds to the energetic part of the spectrum.

The description of the spectrometer is split in two parts : the first one to remind the electron trajectory in this magnetic field, up to the detector, and the second one which

concerns the detection system composed of the scintillator and the imaging system (in Appendix C).

The magnet is composed of two rectangular NdFeB magnets of length $L_m = 5$ cm, width $l_m = 2.5$ cm and thickness 1 cm, separated by a distance of 1 cm. The magnetic field, measured at the center with a magnetic Hall probe, gives $B_m = 0.45$ T. Here is a summary of analytical formulas giving the trajectory for an electron.

B.2 Analytic trajectory

B.2.1 For a rectangular magnet

In this part, we consider a uniform magnetic field, equal to B_m in the magnet and null outside. The radius of curvature R for a relativistic electron of energy E_0 in this magnetic field is given by

$$B_m R = \frac{\sqrt{E_0(E_0 + 2mc^2)}}{ec} \tag{B.1}$$

where e represents the charge of an electron and c the celerity of light. We can consider that observed electrons have an energy much larger than the rest energy, which simplifies this relation to $B_m R = E_0/(ec)$

The geometrical parameters which describe the system are Ds the source-to-magnet distance, Dl the magnet-to-scintillator distance, along the laser axis, θ_l the angle of the scintillator with respect to the transverse axis. Different parameters are defined on figure B.2.

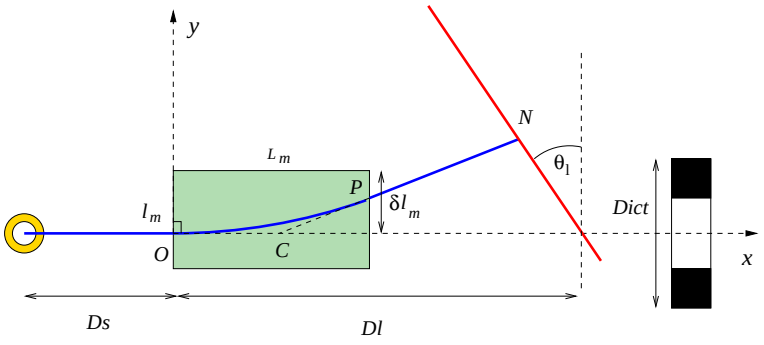

Figure B.2: (Color) Definition of parameters used in the text.

The trajectory of an electron can be described by simple geometric shapes : a straight line outside the magnetic field and a circle's arc in the magnet. The origin of the frame is taken at the entrance in the magnet. The electrons arrives along (Ox), perpendicular to the surface of the magnets. If the electron exits on the opposite side, the intersection of his circular trajectory with the magnet in P has coordinates :

$$(x_P, y_P) = (L_m, R - \sqrt{R^2 - L_m^2}) \tag{B.2}$$

In our experiments, the holder of the magnets prevents electrons from exiting by the side. Electrons that exit by the opposite side follow the relation $y_P < \delta l_m$, where δl_m is the maximum ordinate of the marget.

Point C, which is at the intersection of the tangent to the electron trajectory when it enters and exits the magnet, is defined by $OC = CP$. this gives the following coordinates :

$$(x_C, y_C) = \left(\frac{x_P^2 + y_P^2}{2x_P}, 0 \right) \tag{B.3}$$

Finally, the intersection in N of the electron trajectory with the scintillator by linear trajectory is written :

$$(x_N, y_N) = \left(Dl - y_N \tan(\theta_l), \frac{(Dl - x_C) y_P}{x_P - x_C + y_P \tan(\theta_l)} \right) \tag{B.4}$$

B.2.2 For a circular magnet

Expression B.4 remains valid for a circular magnet with uniform magnetic field, center C and radius $R_m = OC$. One simply needs to replace x_C by R_m.

B.2.3 Adjustment to the magnetic field measured experimentally

In the previous paragraph, The magnetic field was assumed to be uniform. In reality, because nothing has been done to close the field lines, reality is far from this simplified geometry. The real magnetic field has a gradient length comparable to the distance between the poles. in order to take this into account, the real magnetic field has been measured step by step with a Hall probe.

Magnetic field at every position in the dipole approximation

It is not possible to measure the three components of the magnetic field for each position. In order to simulate the electron trajectories, I have written a program that gives all this information. I assume that all materials are magnetically transparent and I compute the total magnetic field from elementary dipoles in the magnet. The magnetic field radiated by a dipole placed in P and measured in M is written

$$d^3\vec{B}(M) = \frac{\mu_0}{4\pi} \vec{\nabla}_M \left(\frac{d\vec{\mathcal{M}} . \vec{r}}{r^3} \right) \tag{B.5}$$

where μ_0 iv the vacuum permeability, $\vec{\nabla}_M$ is the operand of partial derivatives in M, $d\vec{\mathcal{M}} = \vec{m}\, dx_P\, dy_P\, dz_P$ is the elementary dipole magnetic momentum and $\vec{r} = \overrightarrow{PM}$ is the relative position of M with respect to P.

The idea is to basically integrate this equation over the volume defined by the two magnets (P coordinates). It is possible to integrate analytically the magnetic field along some axes for rectangular and circular magnets. This won't be detailled because more complex commercial programs are also available.

On Fig. B.3, one sees the experimental measurements, the result of the computation and the uniform magnetic field used previously. The amplitude of the computed curve has been adjusted to match the measurement at the center of the magnet. The adequacy is really correct between calculations and measurements. One notices that the magnetic

fields reverses sign outside the magnet, which decreases the overall efficiency of the magnet. Because nothing has been done to guide the field lines, it is not surprising that the magnetic field changes sign outside.

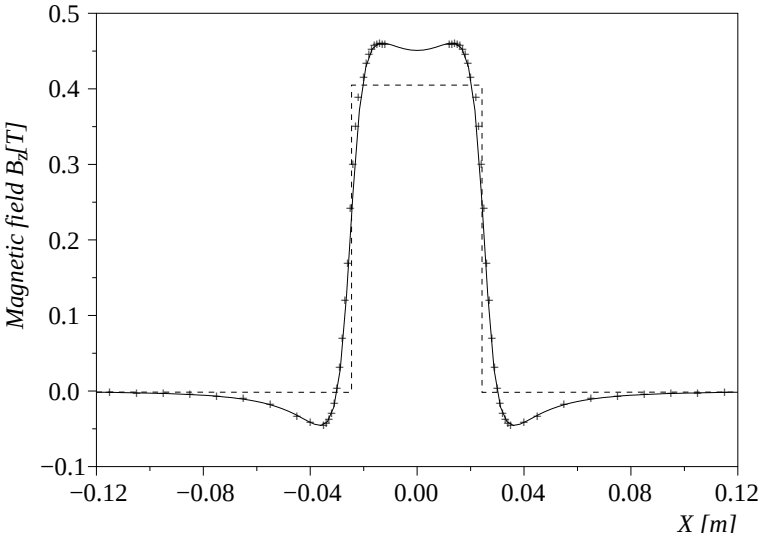

Figure B.3: Comparison of the measured magnetic field *Bz* along the laser axis (plus) to numerical calculations (solid line) and the effective magnetic field used for analytical formulas (dashed line).

Dispersion

We introduce now the effective magnetic field B_m^{eff} which will be used in analytical formulas. Its expression is

$$B_m^{eff} = \frac{1}{L_m} \int_{-\infty}^{+\infty} B_z(x) dx \tag{B.6}$$

where $B_z(x)$ is the component along (Oz) of the magnetic field measured along the propagation axis of the laser. In our experimental conditions, the effective magnetic field equals $B_m^{eff} = 0.41$ T.

Dispersion curves obtained for the calculated magnetic field and for analytical formulas are shown in Fig. B.4. The two curves are almost indistinguishable, which justifies the use of analytic formulas in the following. The uncertainty arising from their separation is negligible from the uncertainty due to the transverse size of the electron beam on the scintillator.

B.2.4 Dispersion power

The resolution of this spectrometer is mainly limited by the divergence of the electron beam. This was not taken into account in the analytic formulas from the previous section, because the electrons trajectory was supposed to be perpendicular to the magnet surface. It has to be understood that even for a perfectly monoenergetic electron beam, the low divergence would give a circular signal (actually elliptic) on the detector around

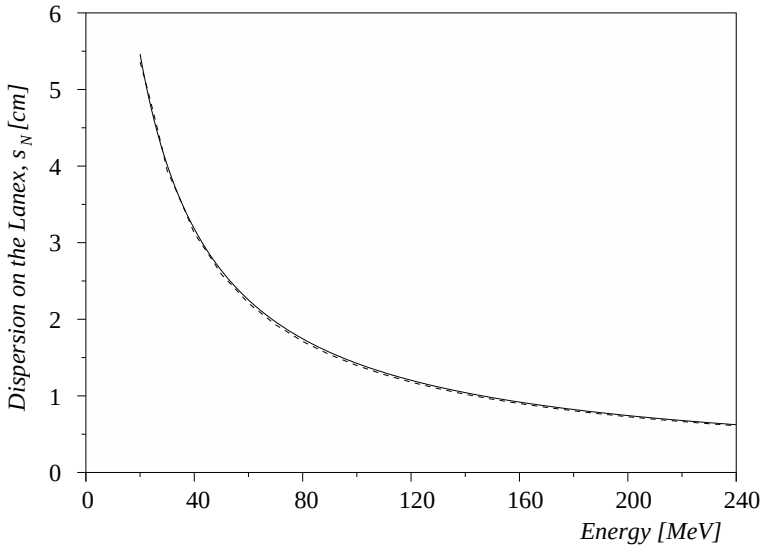

Figure B.4: Dispersion on the phosphor film as function of the electron energy for analytical formulas (dashed line) and for a simulation reproducing the real magnetic field int he magnet at each position (solid line).

the average deviation. The divergence angle can be measured in the transverse direction (non-dispersive because the influence of the magnetic field is negligible). For underdense plasmas, we have measured a divergence of 10 mrad, which weakly depends on the electron energy above 20 MeV for the best shots. In this study, the focusing force of the magnetic field from the edge effect will be neglected (Humphries, 1986). Here is an estimation of these edge effects in the plane perpendicular to the dispersion plane. For thin magnetic lenses, the focal length for an electron of divergence $\theta_s \ll 1$ is $f \sim 2R/\theta_s$, where R is the gyroradius of the electron. If one considers a beam with electron of 100 MeV, with divergence 10 mrad impinging on magnets with a magnetic field of 1 T, the focal length would be 67 m, which is much longer than the size of the experiment.

The relative resolution in energy is defined as the energy range corresponding to the divergence of the electron beam around the average energy E_0, divided by E_0. As the detector is bent, the longitudinal spread of the electron beam on the detector, to the lowest order is $\delta_s = L_{tot}\theta_s/\cos(\theta_\perp)$, where L_{tot} represents the total length of the electron trajectory from the interaction point to the Lanex and $\theta_\perp = \theta_l - \theta_e$ is the angle between the normal to the scintillator and the electron trajectory. θ_e is the angle of the electron with respect to the (Ox) axis (see Fig. C.2) and is written

$$\theta_e = \arctan\left(\frac{y_P}{x_P - x_C}\right) \tag{B.7}$$

Assuming that $\delta_s \ll s_N \ll L_{tot}$, where $s_N = y_N/\cos(\theta_l)$ is the path length along the detector, the resolution for an energy E_0 is :

$$\frac{\delta E}{E_0} = \frac{\delta_s}{E_0} \div \frac{ds_N}{dE} \tag{B.8}$$

Parameter	Symbol	Value
Spectrometer		
Magnet		
Equivalent mag field	B_m^{eff}	0.41 T
Length	L_m	5 cm
Width	l_m	2.5 cm
Shift	δl_m	1.3 cm
Distance to scintillator	D_l	17 cm
Scintillator		
Angle	θ_l	55°
Conversion efficiency	$\varepsilon dE/dx$	1.8 MeV/cm
Areal density	h_S	33 mg/cm^2
Phosphor density	ρ_{GOS}	7.44 g/cm^3
Energy of a photon	E_{ph}	2.27 eV
Transmission factor	ζ	0.22
ICT		
Diameter	D_{ICT}	10 cm
Detection system		
Solid angle	$\delta\Omega$	2.0×10^{-3} sr
Observation angle of the CCD	θ_{CCD}	15°
Lens	q_L	0.95
Quartz	q_Q	0.95
Interference Filter	q_{IF}	0.20
Size of a pixel projected along the scintillator	δs_{pix}	0.28 mm
Electron source		
Distance to the magnet	D_s	6 cm
Divergence	θ_s	10 mrad

Table B.1: Experimental parameters, explained in the text

The equivalent for high energies is :

$$\frac{\delta E}{E_0} \underset{E_0 \to \infty}{\sim} \frac{(Ds + Dl) R \theta_s}{(Dl - L_m/2) L_m} \tag{B.9}$$

This resolution degrades linearly with the electron energy E_0 (included in the the expression of the radius of curvature R).

Numerical application

For the experimental parameters summarized in Table B.1, one obtains a relative resolution of 6, 14, 27 and 53% for electrons with energy 20, 50, 100 and 200 MeV respectively.

B.3 Development of new spectrometers

The main objectives of current experiments is the measurement of energetic electrons. Adapted spectrometers are necessary. When the length of the magnet is much larger than the two other lengths ($D_s \ll D_l$ and $D_l \sim L_m$), then Eq. B.9 becomes $2R\theta_s/L_m$ which evolves as the inverse of $B_m L_m$. Thus, in order to improve the resolution, one has to increase the dispersing power of the magnet (linked to the product $B_m L_m$) either by increasing the magnetic field, or by increasing the magnet length.

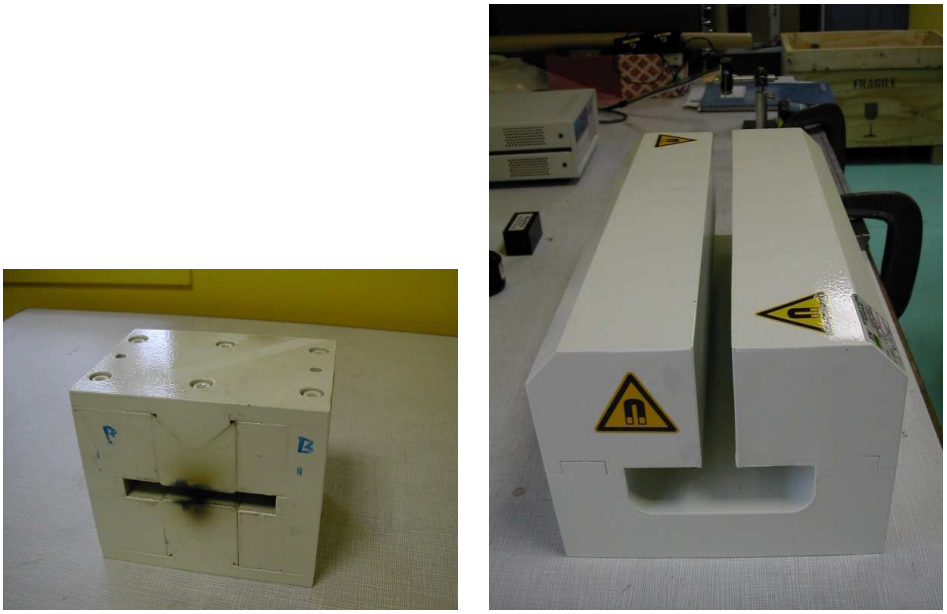

Figure B.5: (Color) Pictures of the 10 cm long magnet (on the left) and the 40 cm long one (on the right).

The maximal magnetic field of rare earth magnets is about 1.3 Tesla in the gap. We have ordered two new magnets with a magnetic field of $B_m = 1$ T between the two poles (see Fig. B.5). The lengths of these magnets are 10 cm and 40 cm. The first one will give a higher resolution that the home-made magnet for energetic electrons (¿100 MeV). The 40 cm-long spectrometer will be used to record electrons with energise of the range of 1 GeV for future experiments. Thanks to the work of the manufacturer to close the field lines, the effective magnetic field has be estimated to be $B_m^{eff} = 1.3$ T for the 10 cm one, which is this time higher than the magnetic field at the center. This testifies a higher quality for this kind of magnet (the magnetic field doesn't change sign outside). This compact spectrometer gives a resolution of 10% at 200 MeV for this divergence, which is much better than the one used previously. Howeverr, the resolution is 49% at 1 GeV, which is not acceptable.

The second spectrometer designed for 1 GeV is much longer and the geometry needs to be modified. In particular, the scintillator has to be placed much further away, which will also lead to an increase of the diameter of the electron beam (because of the divergence). However, with parameters from Table B.2, the resolution at 1 GeV is equal to 18%. We hope also that the divergence of the electron beam will be smaller at this energy,

Modified parameter	Symbol	Value
10 cm spectrometer		
Nominal magnetic field	B_m	1.1 T
Effective magnetic field	B_m^{eff}	1.3 T
Length of the magnet	L_m	10 cm
Width of the magnet	l_m	10 cm
Shift	δl_m	5 cm
Magnet-scintillator distance	D_l	17 cm
Source-magnet distance	D_s	6 cm
40 cm spectrometer		
Nominal magnetic field	B_m	0.85 T
Effective magnetic field	B_m^{eff}	0.87 T
Length of the magnet	L_m	40 cm
Width of the magnet	l_m	8 cm
Shift	δl_m	4 cm
Magnet-scintillator distance	D_l	55 cm
Source-magnet distance	D_s	10 cm

Table B.2: List of modified parameters for the new magnets.

which would also improve the resolution. This magnet, open on one side, also allows the measurement of less energetic electrons, which will leave the magnet by the sides. The distance between the poles has also been increase to 2 cm because the magnet is longer, which gives a final effective field of $B_m^{eff} = 0.87$ T longitudinaly.

This appendix summarizes the work done to build a single shot electron spectrometer. Analytical formulas which give the impact position on the scintillator and the resolution are given. The analytic dispersion is also compared to measurements to adapt the value of the effective magnetic field. Using a compact home-made spectrometer, we have measured new properties of the electron beam : a quasi monoenergetic peak at high energy. However, even if the raw image shows a narrow signal, the deconvolved spectrum is broadened. Consequently, a more dispersive magnet is necessary for this kind of experiment and also a second longer magnet for acceleration to the GeV level. Calculations have been performed to estimate the length of the magnet to reach a sufficient resolution at high energy (200 MeV and 1 GeV).

Appendix C

Determination of the amplitude of the electron spectrum

Initially, the amplitude of the spectrum was determined from the charge measured by the ICT. This appendix presents the absolute calibration, based on the global yield of the detection system to obtain the number of electrons.

The light from the scintillator is emitted by phosphor grains (Giakoumakis and Miliotis, 1985). We will assume that the energy emitted in the visible range is proportional to the energy deposited in the chemical layer Gd_2O_2S:Tb. The energy deposition in pure gadolinium oxysulfide (GOS) is independent of the electron energy above 1 MeV, which is shown in the next paragraph. In order to represent the electron spectrum on a linear scale, one has to take into account the dispersion of electrons. This is based on equations from appendix B.2. Then, the two calibration methods are presented.

C.1 Simulation of the energy deposition in the scintillator

First, I justify that the energy deposition from the electrons in the scintillator can be considered constant above 1 MeV. The equivalent thickness of pure GOS, which emits light, is 44 μm for the Lanex Kodak Fine.

The use of tabulated values for the stopping power (total or collisional), published in (ICRU), implies no propagation of secondary particles. In other words, all secondary particles deposit their energy at the place where they have been created. In reality, one has to take into account the propagation of these secondary particles (mainly photons and electrons), which can leave the scintillator and deposit the energy further away. Monte-Carlo simulations such as `Geant4` (*et al*, 2003) allow to simulate all the particles required. Therefore, I've simulated the propagation of electrons in a 44 μm-thick GOS target. The dose deposition is represented on Fig. C.1. The solid line above 1 MeV is almost horizontal, which means that the effective dose deposition in 44 μm of pure GOS is independent of the energy of the electrons above 1 MeV.

In order to check the computation of dose, I've added the energy of secondary particles that left the scintillator to this curve. The obtained curve matches perfectly the tabulated values for the collisional stopping power. Then, if I also add the energy of secondary photons which left the target, the new curve also matches perfectly the total stopping

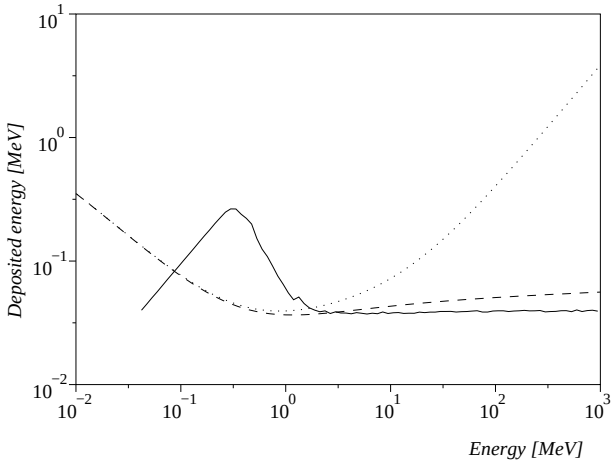

Figure C.1: Energy deposition in pure Gadolinium Oxysulfide from : tabulated values of the collisional stopping power (ICRU) (dashed line), total stopping power (points) and from the Monte-Carlo simulation (solid line).

power. It is perfectly normal to reproduce those curves because `Geant4` uses these tables in its model of elastic scattering and bremstrahlung radiation.

For energies below 1 MeV, there is a peak which doesn't match the tabulated values. Actually, the simulation is not adapted to represent these energies : below 0.3 MeV, electrons lose all their energy and nothing exits from the GOS, which give a straight line with slope 1. Between 0.3 MeV and 1 MeV, the electron energy varies during the propagation in the simulation and the dose deposition increases as the electron loses energy. A correct calculation of the stopping power requires an electron energy large compared to the energy lost in the medium, which is not fulfilled for low energies. For information, the minimum energy for an electron for which the penetration depth exceeds the thickness of the target is 0.12 MeV. The penetration depth ρ is the average integrated path length that an electron can travel before stopping and is defined in the continuous slowing down approximation by :

$$\rho(E) = \int_E^0 \frac{1}{\frac{dE}{dx}(E)} dE \tag{C.1}$$

where dE/dx is the effective stopping power of the particle.

In reality, Lanex Kodak Fine contains several layers of different materials (the description of which is given in Table C.1). The dose deposition calculated in the full scintillator confirms that the energy deposition is constant above 1 MeV.

Such simulations have already been done for other type of detectors (Tanaka et al., 2005) (Film Fuji BAS-SR2025). Their detector contains elements which are excited in a metastable state by the incoming radiation (electrons). The optical reading in a scanner triggers the forced desexcitation of these levels. The authors had already concluded for their system that the energy deposition became energy-independent above 1 MeV and verified it experimentally for electrons of 11.5, 30 and 100 MeV.

Element	Material	Density (g/cm^3)	Thickness (cm)
Shielding			
Aluminium foil	aluminium	2.7	0.0100
Kodak Lanex Fine			
protective coating	cellulose acetate	1.32	0.0010
plastic substrate	poly(ethylene terephtalate)	1.38	0.0178
scintillator	Gd_2O_2S + binder	4.25	0.0084
protective coating	cellulose acetate	1.32	0.0005

Table C.1: Composition of the scintillator.

C.2 Calibration of the scintillator at Elyse

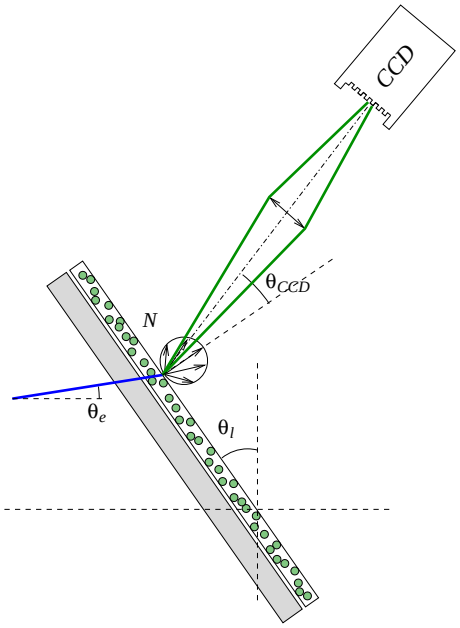

Figure C.2: (Color) Scintillator, imaging system and associated parameters.

The description of the scintillator and the imaging system have already been described for incident X-rays (Radcliffe et al., 1993) and protons (Boon, 1998). We have used the scintillator Kodak Lanex Fine which is composed of several layers (Schach von Wittenau et al., 2002) (see Table C.1). In particular, it contains a mixture of phosphor grains in a urethane binder (see Fig. C.2). The areal density of the phosphor is $h_S = 33$ mg/cm^2 for this scintillator. The thickness of pure scintillator is obtained by dividing h_S by the density of GOS (7.44 g/cm^3). One obtains a thickness of 44 μm, which is the value used before. The following is dedicated to the calibration of this powder contained in the scintillator, since only this part emits visible light.

However, as explained by S. N. Boon, there exist no information on the efficiency of scintillators for proton or electron beams. The intrinsic conversion efficiency ε in

Gd_2O_2S:Tb, which is the fraction of deposited energy which is converted into visible light in the material, has been measured only for X-ray beams (Giakoumakis et al., 1989). The different measurements gave values between 15 % and 20 %. For several reasons, these values are not correct for electrons : (i) manufacturers don't know if the scintillator is linear for such electron fluence, (ii) the intrinsic conversion efficiency depends on the nature and the energy of the radiation. Previous studies have been carried out only for X-rays in the range 20-70 keV.

The calibration of this scintillator for electrons has thus been performed on the accelerator Elyse at Orsay (Belloni et al., 2005). This is a radiofrequency accelerator used for radiolysis. The photocathode delivers electrons which are accelerated to a maximum energy of 9 MeV using radiofrequency cavities and each pulse contains a maximum of 5 nC. We have been working at a repetition rate of 1 Hz in order to ensure that the scintillator didn't heat. Electron bunches had a duration of 15 ps. At the output of the accelerator, electrons travel through a 12 μm-thick aluminium foil and then propagate in air (see Fig. C.3). They travel through the core of the ICT and then through the scintillator placed perpendicular to the beam and imaged onto a 16 bit Andor CCD camera, looking at an angle of 45° at a distance of 61 cm from the surface of the scintillator. The exposure time was the same as during the experiments (90 ms), which is much longer than the relaxation time of the scintillator (of the order of a millisecond). We have also used an interference filter at 546 nm to reproduce the usual experimental conditions. The scattering of the electrons in the aluminium foil implies all these elements to be placed as close as possible from each other to avoid loosing any signal. Because all electrons travel through the core of the ICT and because there is no electromagnetic noise, this device gave a reliable charge contained in the electron bunch, matching the value obtained independently with a Faraday cup placed in the beam. The dark current level was negligible. We have been working at three different energies : 3.3, 4.8 and 8.5 MeV.

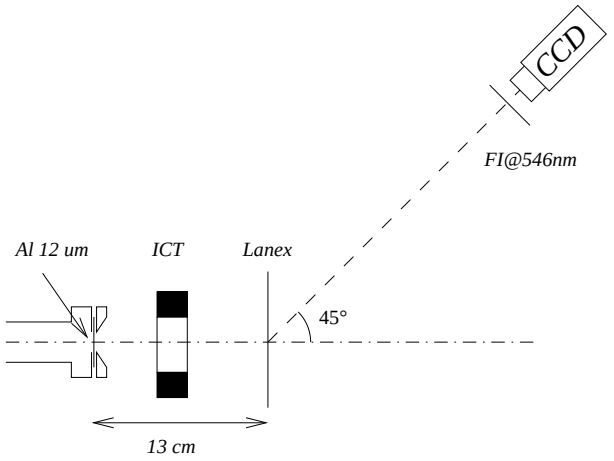

Figure C.3: Experimental setup for the calibration of the scintillator.

The scintillator response is linear as function of the charge (see Fig. C.4). Figure C.5 shows the ratio between the integrated number of counts on the CCD and the measured charge from the ICT for the three electron energies. This ratio is independent of the electron energy, in accordance with simulations of the energy deposition presented above (in

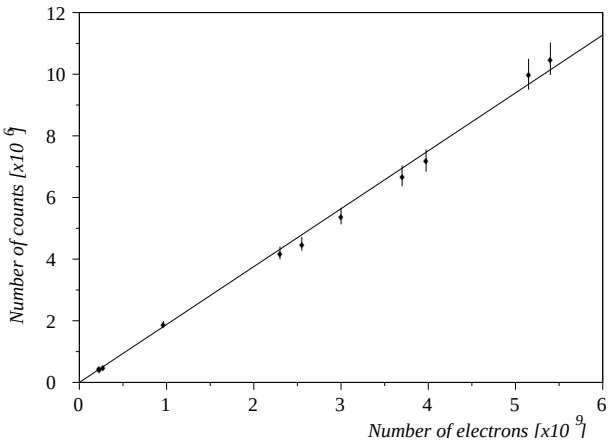

Figure C.4: Evolution of the measured signal as function of the charge at 3.3 MeV.

Fig. C.1). The error bars are larger at 8.5 MeV because the signal contains X-rays that can perturb the ratio. Using the experimental geometry and formulas presented previously, one obtains the fraction of kinetic energy of an electron which has been converted into visible light per unit of thickness of pure scintillator $\varepsilon dE/dx = 1.8 \pm 0.2$ MeV/cm. Using the results from the Monte-Carlo simulation, this leads to $\varepsilon = 16\% \pm 2\%$, which is surprisingly close to the the value for X-rays (Giakoumakis et al., 1989). This value is independent of the geometry and the detection system. It can be used for other scintillators (Gd_2O_2S:Tb) for which the areal density is known.

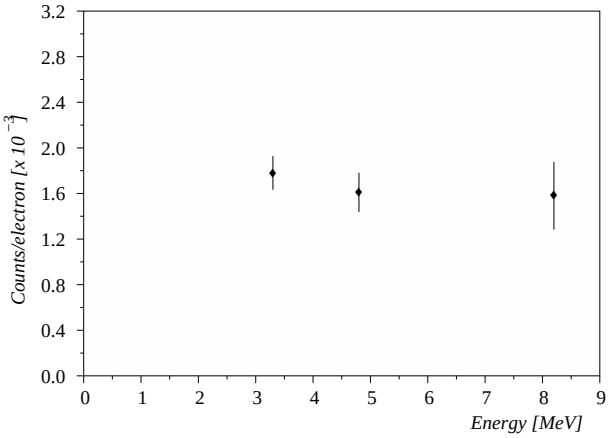

Figure C.5: Ratio of the number of counts measured on the CCD camera to the number of electron contained in the bunch at 3.0, 4.8 and 8.5 MeV. The error bars account for statistical fluctuations of the ratio for each energy and for the analysis.

C.3 Absolute calibration

Assuming that the intrinsic conversion efficiency can be used in our experimental conditions, it is possible to obtain the relation between the number of electrons which travelled through the scintillator and the number of counts on the CCD by estimating the global response of the optical system.

C.3.1 Conversion in photons in the scintillator

The equivalent number of photons N_{cr} created at the central wavelength in the scintillator for each incident electron is

$$\frac{dN_{cr}}{dN_{el}} = \frac{1}{E_{ph}} \varepsilon \frac{dE}{dx}\, \delta x \tag{C.2}$$

where $\delta x = h_S/(\rho_{GOS}\cos(\theta_\perp))$ is the equivalent thickness of pure phosphor crossed by an electron and E_{ph} is the energy of a photon at 546 nm. Other lines in the emission spectrum will be damped by the interference filter placed in front of the camera.

C.3.2 Collection by optics

Created photon experience multiple elastic scattering in the medium and at its interfaces, because of the variation of index of refraction. The fraction of light which escapes the screen has already been estimated (Radcliffe et al., 1993). By extrapolating this curve to the areal density of our scintillator, the transmission factor becomes $\zeta = 22\%$. The angular distribution is close to a Lambertian law (cosine) (Giakoumakis and Miliotis, 1985). According to that article, this law is adapted to radiations leading to homogeneous dose deposition along the thickness of the scintillator. The authors also stress that the incidence angle of the electron on the screen has no influence on the angular distribution at the rear side. Finally, the number of photons collected by the detector by each pixel of the camera, for each created photon is

$$\frac{dN_{coll}}{dN_{cr}} = \zeta\, g(\theta_{CCD})\, \delta\Omega\, q_l\, q_Q\, q_{IF} \tag{C.3}$$

where $g(\theta_{CCD}) = \cos(\theta_{CCD})/\pi$ is the normalized Lambertian law, evaluated at the observation angle of the camera, $\delta\Omega$ is the solid angle of collection. q_l, q_Q and q_{IF} are transmission factors of the lens, the quartz window in front of the CCD and the interference filter respectively. The transmission of the interference filter is the fraction of light energy in the visible range of the emission spectrum of the scintillator which is transmitted.

C.3.3 Yield of the camera

We have been using a CCD camera from Andor, model DV420-FI for the detection. The quantum efficiency (number of electrons produced for an optical photon) of the camera at -20° C and at wavelength 546 nm is $QE = 26\%$ and $r = 7$ electrons are required to make one count on the CCD (for a readout time of 16 μs per pixel). These data are provided by the manufacturer. The yield of the CCD is

$$\frac{dN_{cts}}{dN_{coll}} = \frac{QE}{r} \tag{C.4}$$

Finally, the measurement gives the number of counts $\mathrm{Cts}(E_0)$ corresponding to each pixel of the CCD. The initial spectrum is obtained using the following formula :

$$\frac{dN_{el}}{dE}(E_0) = \frac{\mathrm{Cts}(E_0)}{\delta s_{pix}} \frac{ds_N}{dE} \div \left(\frac{dN_{cts}}{dN_{coll}} \frac{dN_{coll}}{dN_{cr}} \frac{dN_{cr}}{dN_{el}} \right) \tag{C.5}$$

where δs_{pix} is the size of a pixel projected along the scintillator.

This absolute calibration is compared to another calibration method using an integrating current transformer.

C.4 Use of an integrating current transformer

We have been using the combination of an Integrating Current Transformer (Bergoz ICT-055-070-20:1) and a Beam Charge Monitor (Bergoz BCM-RRS/B) to obtain the charge contained in a part of the spectrum. This second device integrates the signal from the ICT and holds a constant voltage proportional to the measured charge at the output. The value given by this device can be inaccurate for several reasons :

- This electrical device is not designed to measure electron bunches as short as 100 fs. When the electron bunch is very short, the signal from the ICT can oscillate because of the excitation of a resonance in the circuit. However, the measurement unit (BCM) integrates these oscillations and is expected to give a reliable measurement as explained in the documentation.
- The influence of electrons that travel in the surrounding area of the ICT or inside the coil itself isn't known, even if we know that a perfect ICT should give a null contribution from all electrons travelling outside. Normally, all electrons should flow inside the core of the ICT.
- The electronic system is also sensitive to the electromagnetic field from the laser and the one generated at the interaction point. Thus, the ICT has been placed as far as possible from the interaction point ($\sim$ 50 cm). The ICT was also shielded from direct exposure to the laser light by inserting a perforated teflon mask in from of it.
- Finally, this device is also sensitive to the huge amount of low energy electrons which are sent in all directions from the interaction point. Their contribution to the measured signal can significantly alter the impact of the measurement. In order to block these low-energy electrons, we have placed lead shielding all around the magnet.

After additional null tests, the signal given by the ICT seemed to be consistent with our expectations. The absolute calibration which has been available later during my thesis has given lower charge.

The number of counts on the camera is corrected for the energy dispersion. The number of electrons dN_{el}/dE with energy between E_0 and $E_0 + dE$ is proportional to $f(E_0)$

$$f(E_0) = \mathrm{Cts}(E_0) \frac{ds_N}{dE}(E_0) \tag{C.6}$$

where $\mathrm{Cts}(E_0)$ is the number of counts corresponding to energy E_0 (integrated along the non-dispersive axis), ds_N/dE represents the energy dispersion. The final spectrum dN_{el}/dE is obtained from $f(E_0)$ by normalizing the signal above E_{ICT} (minimum energy intercepted by the ICT) to the number of electrons collected by the ICT. However, the effective diameter is difficult to determine and the cutoff energy has been set to the two extreme diameters of the ICT (internal and external). This leads to large error bars when using this calibration method.

Two independent methods are proposed to determine the amplitude of the electron spectrum : either using the absolute calibration of the detector, or using an integrating current transformer. A detailled description of all physical parameters involved in this calculation is given in the text. These two methods are compared in the section with experimental results (Sec. 2.2.4). However, these two methods suffer from drawbacks : the ICT is sensitive to electromagnetic perturbation and to very-low-energy electrons, the response from the scintillator can differ from the one measured on the conventional accelerator when exposed to a brief electron beam with a large fluency.

Bibliography

Abraham I., Abraham R., Desolneux A., and Li Thiao-Te S. Significant edges in the case of a non stationnary gaussian noise. *Pattern Recognition Letters*, 2006. submitted.

Amiranoff F., Bernard D., Cros B., Jacquet F., Matthieussent G., Miné P., Mora P., Morillo J., Moulin F., Specka A. E., and Stenz C. Electron acceleration in nd-laser plasma beat-wave experiments. *Phys. Rev. Lett.*, **74** p5220–5223, 1995.

Andreev N. E. and Kutnetsov K. K. Monoenergetic laser wakefield acceleration. *PRST*, **3** p021301, 2000.

Andreev N. E., Gorbunov L. M., Kirsanov V. I., Pogosova A. A., and Ramazashvili R. R. Resonant excitation of wakefields by a laser pulse in a plasma. *JETP Lett.*, **55** p571, 1992.

Antonsen T. M. and Mora P. Self-focusing and raman scattering of laser pulses in tenuous plasmas. *Phys. Rev. Lett.*, **69** p2204, 1992.

Arkhiezer A. I. and Polovin R. V. Theory of wave motion of an electron plasma wave. *Sov. Phys. JEPT*, **3** p696–705, 1956.

Åsell M., Hyödynmaa S., Gustafsson A., and Brahme A. Optimization of 3d conformal electron beam therapy in inhomogeneous media by concomitant fluence and energy modulation. *Phys. Med. Biol.*, **42** p2083, 1997.

Belloni J., Monard H., Gobert F., Larbre J.P., Demarque A., De Waele V., Lampre I., Marignier J.L., Mostafavi M., Bourdon J.C., Bernard M., Borie H., Garvey T., Jacquemard B., Leblond B., Lepercq P., Omeich M., Roch M., Rodier J., and Roux R. Elyse : a picosecond electron accelerator for pulse radiolysis research. *Nucl. Instr. & Meth. in Phys. Research A*, **539** p527, 2005.

Boon S. N. *Dosimetry and quality control of scanning proton beams*. University Library Groningen, 1998.

Bracewell R. *The Fourier transform and its applications*. McGraw-Hill, New York, 3 edition, 1999. ISBN 0070070164.

Brozek-Pluska B., Gliger D., Hallou A., Malka V., and Gauduel Y.A. Direct observation of elementary radical events: low- and high-energy radiation femtochemistry in solutions. *Rad. Phys. and Chem.*, **72** p149–157, 2005.

Bulanov S. V., Inovenkov I.N., Khoroshkov V. I., Naumova N. M., and Sakharov A.S. Nonlinear depletion of ultrashort and relativistically strong laser pulses in an underdense plasma. *Phys. Fluids B,* **4** p1935, 1992.

Castellano M. and Verzilov V.A. Spatial resolution in optical transition radiation beam diagnostics. *Phys. Rev. Spec. Topics Acc. & Beams*, **1** p062801, 1998.

Chen Y.J., Bertolini L. R., Caporaso G. J., Chambers F. W., Cook E. G., Falabella S., Goldin F. J., Guethlein G., Ho D. D.-M., McCarrick J. F., Nelson S. D., Neurath R., Paul A. C., Pincosy P. A., Poole B. R., Richardson R. A., Sampayan S., Wang L.-F., Watson J. A., Westenskow G. A., and Weir J. T. Downstream system for the second axis of the darht facility. In *Proc. of the XXI International Linac Conference*. US Department of Energy (US), 2002. ISBN UCRL-JC-146612.

Chiron A., Bonnaud G., Dulieu A., Miquel J.L., Malka G., Louis-Jacquet M., and Mainfray G. Experimental onservation and simulations on relativistic self-guiding of an ultra-intense laser pulse in underdense plasmas. *Phys. Plasmas*, **3** p1373–1401, 1996.

Chiu C., Fomytskyi M., Grigsby F., and Raischel F. Laser electron accelerators for radiation medicine : A feasibility study. *Med. Phys.*, **31** p2042, 2004.

Clayton C. E., Everett M. J., Lal A., Gordon D., Marsh K. A., and Joshi C. Acceleration end scattering of injected electrons in plasma beatwave accelerator. *Phys. Plasmas.*, **1** p1753, 1994.

Clayton C.E., Tzeng K.C., Gordon D., Muggli P., Mori W.B., Joshi C., Malka V., Najmudin Z., Modena A., Neely D., and Dangor A.E. Plasma wave generation in a self-focused channel of a relativistically intense laser pulse. *Phys. Rev. Lett.*, **81** p100, 1998.

Dawson J.M. Nonlinear electron oscillation in a cold plasma. *Phys. Rev.*, **133** p383, 1959.

Decker C.D., Mori W.B., Tzeng K.C., and Katsouleas T. Nonlinear theory of intense laser-plasma interaction. *Phys. Plasmas,* **3** p2047, 1996.

DesRosiers C., Moskvin V., Bielajew A. F., and Papiez L. 150-250 mev electron beams in radiation therapy. *Phys. Med. Biol.*, **45** p1781, 2000.

Dinten J.M. *Tomographie à partir d'un nombre limité de projections; régularisation par des champs markoviens*. PhD thesis, Université de Paris Sud: Centre d'Orsay, 1990.

Drake J.F., Kaw P.K., LEE Y.C., Schmidt G., Liu C.S., and Rosenbluth M.N. Paramatric instabilities of electromagnetic waves in plasmas. *Phys. MFluid.*, **17** p778, 1974.

Esarey E., Hubbard R.F., Leemans W.P., Ting A., and Sprangle P. Electron injection into plasma wake fields by colliding laser pulses. *Phys. Rev. Lett.*, **79** p2682, 1997.

Esarey E., Shadwick B.A., Catravas P., and Leemans W.P. Synchrotron radiation from electron beams in plasma-focusing channels. *Phys. Rev. E,* **65** p056505, 2002.

et al Agostinelli S. Geant4 - a simulation toolkit. *Nucl. Instr. Meth. A*, **506** p250, 2003.

Everett M.J., Lal A., Gordon D., Clayton C.E., Marsh K.A., and Joshi C. Trapped electron acceleration by a laser-driven relativistic plasma wave. *Nature*, **368** p527–529, 1994.

Faure J., Glinec Y., Pukhov A., Kiselev S., Gordienko S., Lefebvre E., Rousseau J. P., Burgy F., and Malka V. A laser-plasma accelerator producing monoenergetic electron beams. *Nature*, **431** p541, 2004.

Faure J., Glinec Y., Santos J.J., Malka V., Kiselev S., Pukhov A., and Hosokai T. Observation of laser pulse self-compression in nonlinear plasma waves. *Phys. Rev. Lett.*, **95** p205003, 2005.

Faure J., Glinec Y., Gallot G., and Malka V. Ultra-short laser pulses and ultra-short electron bunches generated in relativistic laser-plasma interaction. *Phys. Plasmas*, **13** p056706, 2006.

Fourkal E., Li J. S., Ding M., Tajima T., and Ma C.-M. Particle selection for laser-acceleration proton therapy feasibility study. *Med. Phys.*, **30** p1660, 2003.

Fritzler S., Lefebvre E., Malka V., Burgy F., Dangor A. E., Krushelnick K., Mangles S. P. D., Najmudin Z., Rousseau J.-P., and Walton B. Emittance measurements of a laser-wakefield-accelerated electron beam. *Phys. Rev. Lett.*, **92** p165006, 2004.

Fubiani G., Esarey E., Schroeder C.B., and Leemans W.P. Beat wave injection of electrons into plasma waves using two interfering laser pulses. *Phys. Rev. E*, **70** p016402, 2004.

Gahn C., Tsakiris G. D., Pukhov A., VehnMeyer-ter J., Pretzler G., Thirolf P., Habs D., and Witte K. J. Multi-mev electron beam generation by direct laser acceleration in high density plasma channels. *Phys. Rev. Lett.*, **83** p4772, 1999.

Gauduel Y. and Rossky P.J. *Ultrafast Reaction Dynamics and Solvent Effects: experimental and theoretical aspects*. AIP Press, New York, 1994. ISBN 1-56396-280-2.

Gauduel Y., Sander M., and Gelabert H. Ultrafast reactivity of ir-excited electron in aqueous ionic solutions. *J. Phys. Chem. A*, **102** p7795–7803, 1998.

Gauduel Y., Gelabert H., and Guilloud F. Real-time probing of a three-electron bonded radical: ultrafast one-electron reduction of a disulfide biomolecule. *J. Am. Chem. Soc.*, **122** p5082–5091, 2000.

Gauduel Y. A., Fritzler S., Hallou A., Gliger D., and Malka V. Femtosecond relativistic electron beam triggered early bioradical events. In *Femtosecond laser applications in biology*, volume 5463, pages 86–96. SPIE, 2004.

Geddes C. G. R., Toth CS., Van Tilborg J., Esarey E., Schroeder C. B., Bruhwiler D., Nieter C., Cary J., and Leemans W. P. High-quality electron beams from a laser wakefield accelerator using plasma-channel guiding. *Nature*, **431** p538, 2004.

Giakoumakis G. E. and Miliotis D. M. Light angular distribution of fluorescent screens excited by x-rays. *Phys. Med. Biol.*, **30** p21–29, 1985.

Giakoumakis G. E., Nomicos C. D., and Sandilos P. X. Absolute efficiency of gd_2o_2s:tb screens under fluoroscopic conditions. *Phys. Med. Biol.*, **34** p673–678, 1989.

Ginzburg V.L. and Frank I.M. *Zh. Eksp. Teor. Fiz.*, **16** p15, 1946.

Glinec Y., Faure J., Le Dain L., S. Darbon, Hosokai T., Santos J. J., Lefebvre E., Rousseau J. P., Burgy F., Mercier B., and Malka V. High-resolution γ-ray radiography produced by a laser-plasma driven electron source. *Phys. Rev. Lett.*, **94** p025003, 2004.

Glinec Y., Faure J., Pukhov A., Kiselev S., Gordienko S., Mercier B., and Malka V. Generation of quasi-monoenergetic electron beams using ultrashort and ultraintense laser pulses. *Laser & Part. Beams*, **23** p161–166, 2005.

Glinec Y., Faure J., Guemnie-Tafo A., Malka V., Monnard H., Larbre J.P., De Waele V., Marignier J.L., and Mostafavi M. Absolute calibration for a broad range single shot electron spectrometer. *Rev. Sci. Instr.*, **77** p103301, 2006a.

Glinec Y., Faure J., Malka V., Fuchs T., Szymanowski H., and Oelfke U. Radiotherapy with laser-plasma accelerators: Monte carlo simulation of dose deposited by an experimental quasimonoenergetic electron beam. *Med. Phys.*, **33** p155, 2006b.

Goldsmith P. and Jelley J.V. *Phil. Mag.*, **4** p836, 1959.

Gorbunov L. M. and Kirsanov V. I. Excitation of plasma waves by an electromagnetic wave packet. *Zh. Eksp. Teor. Fiz.*, **93** p509, 1987.

Gorbunov L.M., Kalmykov S.Y., and Mora P. Laser wakefield acceleration by petawatt ultrashort laser pulses. *Physics of Plasmas*, **12** p3101, 2005.

Gordienko S. and Pukhov A. Scalings for ultrarelativistic laser plasmas and quasimonoenergetic electrons. *Phys. Plasmas*, **12** p043109, 2005.

Haase O., Goebbels J., Illerhaus B., Bailey M., and Sene M. High energy tomography and crack detection. *J. Nondest. Test. & Ultrason.*, **7**(2), 2002.

Hafz N., Hur M.S., Kim G.H., Kim C., Ko I.S., and Suk H. Quasimonoenergetic electron beam generation by using a pinholelike collimator in a self-modulated laser wakeeld acceleration. *Phys. rev. E*, **73** p016405, 2006.

Hidding B., Amthor K.U., Liesfeld B., Schwoerer H., Karsch S., Geissler M., Veisz L., Schmid K., Gallacher J.G., Jamison S.P., Jaroszynski D., Pretzler G., and Sauerbrey R. Generation of quasimonoenergetic electron bunches with 80-fs laser pulses. *Phys. Rev. Lett.*, **96** p105004, 2006.

Hogan M.J., Barnes C.D., Clayton C.E., F.J. Decker, Deng S., Emma P., Huang C., Iverson R.H., Johnson D.K., Joshi C., Katsouleas T., Krejcik P., Lu W., Marsh K.A., Mori W.B., Muggli P., O'Connell C.L., Oz E., Siemann R.H., and Walz D. Multi-gev energy gain in a plasma-wakefield accelerator. *Phys. Rev. Lett.*, **95** p054802, 2005.

Hosokai T., Kinoshita K., Zhidkov A., Nakamura K., Watanabe T., Ueda T., Kotaki H., Kando M., Nakajima K., and Ueseka M. Effect of a laser prepulse on a narrow-cone ejection of mev electrons from a gas jet irradiated by an ultrashort laser pulse. *Phys. Rev. E*, **67** p036407, 2003.

Hosokai *et al.* T. Observation of strong correlation between quasimonoenergetic electron beam generation by wakeeld and laser guiding inside a preplasma cavity. *Phys. Rev. E*, **73** p036407, 2006.

Hsieh C.T., Huang C.M., Chang C.L., Ho Y.C., Chen Y.S., Lin J.Y., Wang J., and Chen S.Y. Tomography of injection and acceleration of monoenergetic electrons in a laser-wakefield accelerator. *Phys. Rev. Lett.*, **96** p095001, 2006.

Humphries S. *Principles of charged particle acceleration*. Wiley-Interscience, New-York, 1986. Sec. 6.8, 6.9 and 6.10.

Hyödynmaa S., Gustafsson A., and Brahme A. Optimization of conformal electron beam therapy using energy- and fluence-modulated beams. *Med. Phys.*, **23** p659, 1996.

ICRU. Stopping powers for electrons and positrons. Technical Report 37, International Commission on Radiation Units and Measurements, 1984.

Jackson J.D. *Classical Electrodynamics*. J. Wiley & Sons, New-York, 2nd edition, 1925. p662.

Joshi C., Tajima T., Dawson J.M., Baldis H.A., and Ebrahim N.A. Forward raman instability and electron acceleration. *Phys. Rev. Lett.*, **60** p1298, 1981.

Kainz K. K., Hogstrom K. R., Antolak J. A., Almond P. R., Bloch C. D., Chiu C, Fomytskyi M., Raischel F., Downer M., and Tajima T. Dose properties of a laser accelerated electron beam and prospects for clinical application. *Med. Phys.*, **31** p2053, 2004.

Kaluza M., Mangles S.P.D., Thomas A.G.R., Murphy C.D., Najmudin Z., Dangor A.E., and Krushelnick K. Observation of a long-wavelength hosing instability in a self-injected laser-wakefield accelerator. 2006. in preparation.

Katsouleas T. and Mori W.B. Wave-breaking amplitude of relativistic oscillations ina thermal plasma. *Phys. Rev. Lett.*, **61** p90–93, 1988.

Khachatryan A.G., Goorvan F. A., Boller K.J., Reitsma A.J.W., and Jarozynski D.A. Extremely short relativistic-electron-bunch generation in the laser wakefield via novel bunch injection scheme. *Phys. Rev. Lett. ST*, **7** p121301, 2004.

Kiselev S., Pukhov A., and Kostyukov I. X-ray generation in strongly nonlinear plasma waves. *Phys. Rev. Lett.*, **93** p135004, 2004.

Kitagawa Y., Matsumoto T., Minamihata T., Sawai K., Matsuo K., Mima K., Nishihara K., Azechi H., Tanaka K. A., H. Takabe, and Nakai S. Beat-wave excitation of plasma wave and observation of accelerated electrons. *Phys. Rev. Lett.*, **68** p48, 1992.

Kozawa T., Saeki A., Mizutani Y., Miki M., Yammoto T., Yoshida Y., and Tagawa S. Isir subpicosecond pulse radiolysis system. In *Proceedings of the 1999 Particle Accelerator Conference*, page 596, 1999.

Krall J. and Joyce G. Transverse equilibrium and stability of the primary beam in the plasma wake-field accelerator. *Phys. Plasma*, **2** p1326–1331, 1994.

Kruer W.L. *The physics of laser plasma interactions*. Addison-Wesley, New-York, 1988.

Kung P., Lihn H.C., Wiedemann H., and Bocek D. Generation and measurement of 50-fs (rms) electron pulses. *Phys. Rev. Lett.*, **73** p967–970, 1994.

Leemans W.P., Tilborgvan J., Faure J., Geddes C.G.R., Toth Cs., Schroeder C.B., Esarey E., Fubiani G., and Dugan G. Terahertz radiation from laser accelerated electron bunches. *Phys. of Plasmas*, **11** p2899–2906, 2004.

Lifschitz A.F., Faure J., Malka V., and Mora P. Gev wakefield acceleration of low energy electron bunches using petawatt lasers. *Phys. of Plasmas*, **12** p0931404, 2005.

Lifschitz A.F., Faure J., Glinec Y., Mora P., and Malka V. Proposed scheme for compact gev laser plasma accelerator. *Laser and Particle Beams*, 2006. to be published.

Lin Y.Z. Low energy electron linacs and their applications in china. In *Proceeding of the Asian Particle Accelerator Conference*, 1998.

Lomax T. Intensity modulation methods for proton radiotherapy. *Phys. Med. Biol.*, **44** p185, 1999.

Lu W., Huang C., Zhou M., Mori W.B., and Katsouleas T. A nonlinear theory for relativistic plasma wakefields in the blowout regime. *Phys. Rev. Lett.*, **96** p165002, 2006a.

Lu W., Tzoufras M., Joshi C., Tsung F.S., Mori W.B., Viera J., Fonseca R.A., and Silva L.O. Generating multi-gev electron bunches using laser wakefield acceleration in the blowout regime. *Nature Physics*, 2006b. submitted.

Ma C.M., Pawlicki T., Lee M.C., Jiang S.B., Li J.S., Deng J., Yi B., Mok E., and Boyer A.L. Energy- and intensity-modulated electron beams for radiotherapy. *Phys. Med. Biol.*, **45** p2293, 2000.

Malka V., Faure J., Marquès J. R., Amiranoff F., Rousseau J. P., Ranc S., Chambaret J. P., Najmudin Z., Walton B., Mora P., and Solodov A. Characterization of electron beams produced by ultrashort (30 fs) laser pulses. *Physics of Plasmas*, **8** p2605–2608, 2001.

Malka V., Fritzler S, Lefebvre E., Aleonard M.-M., Burgy F., CHambaret J.-P., Chemin J.-F., Krushelnick K., Malka G., Mangles S. P. D., Najmudin Z., Pittman M., J.-P. Rousseau, Scheurer J.-N., Walton B., and Dangor A. E. Electron acceleration by a wake field forced by an intense ultrashort laser pulse. *Science*, **298** p1596–1600, 2002.

Malka V., Fritzler S., Lefebvre E., d'Humieres E., Ferrand R., Grillon G., Albaret C., Meyroneinc S., Chambaret J.P., Antonetti A., and Hulin D. Practicability of proton-therapy using compact laser systems. *Med. Phys.*, **31** p1587, 2004.

Malka V., Faure J., Glinec Y., and Lifschitz A.F. Laser-plasma accelerators: a new tool for science and for society. *Plasma Phys. and Contr. Fus.*, **47** pB481–B490, 2005a.

Malka V., Faure J., Glinec Y., Pukhov A., and Rousseau J.P. Monoenergetic electron beam optimization in the bubble regime. *Phys. Plasmas*, **12** p056702, 2005b.

Malka V., Lifschitz A.F., Faure J., and Glinec Y. Design of a compact gev laser plasma accelerator. *Nucl. Instr. and Meth. in Phys. Res. A*, 2005c. to be published.

Mangles S., Murphy C. D., Najmudin Z., Thomas A. G. R., Collier J. L., Dangor A. E., Divall A. J., Foster P. S., Gallacher J. G., Hooker C. J., Jaroszynski D. A., Langley A. J., Mori W. B., Nooreys P. A., Viskup R., Walton B. R., and Krushelnick K. Monoenergetic beams of relativistic electrons from intense laser plasma interactions. *Nature*, **431** p535, 2004.

Mangles *et al.* S.P.D. Laser-wakefield acceleration of monoenergetic electron beams in the first plasma-wave period. *Phys. Rev. Lett.*, **96** p215001, 2006.

McKinstrie C.J. and Bingham R. Stimulated raman forward scattering and the relativistic modulational instability of light waves in rarefied plasma. *Phys. Fluid. B*, **4** p2626, 1992.

Miura E., Koyama K., Kato S., Saito S., Adachi M., Kawada Y., Nakamura T., and Tanimoto M. Demonstration of quasi-monoenergetic electron-beam generation in laser-driven plasma acceleration. *Appl. Phys. Lett.*, **86** p251501, 2005.

Modena A., Najmudin Z., Dangor A. E., Clayton C. E., Marsh K; A., Joshi C., Malka V., Darrow C. B., Danson C., Neely D., and Walsh F. N. Electron acceleration from the breaking of relativistic plasma waves. *Nature*, **377** p606, 1995.

Moore C.I., Ting A., Krushelnick K., Esarey E., Hubbard R.F., Hafizi B., Burris H.R., Manka C., and Sprangle P. Electron trapping in self-modulated laser wakefields by raman backscatter. *Phys. Rev. Lett.*, **79** p3909, 2004.

Mora P. Three-dimensionnal effects in the acceleration of test electrons in a relativistic electron plasma wave. *J. Appl. Phys.*, **71** p2087–2091, 1992.

Mora P. and Amiranoff F. Electron acceleration in a relativistic electron plasma wave. *J. Appl. Phys.*, **66** p3476–3481, 1989.

Mora P. and Antonsen T.M. Electron cavitation and acceleration in the wake of an ultraintense, self-focused laser pulse. *Phys. Rev. E*, **53** pR2068–R2071, 1996.

Mora P. and Antonsen T.M. Kinetic modeling of intense short laser pulses propagating in tenuous plasmas. *Phys. Plasmas*, **4** p217–229, 1997.

Mori W.B., Joshi C., Dawson J.M., Forslund D.W., and Kindel J.M. Evolution of self-focusing of intense electromagnetic waves in plasma. *Phys. Rev. Lett.*, **60** p1298, 1988.

Muroya Y., Meesungnoen J., Jay-Gerin J.P., Filati-Mouhim A., Goulet T, Katsumura Y., and Mankhetkorn S. Radiolysis of liquid water : an attempt to reconcile monte-carlo calculations with new experimental hydrated electron yield data at early times. *Can. J. Chem.*, **80** p1367–1374, 2002.

Oelfke U. and Bortfeld T. Optimization of physical dose distributions with hadron beams: comparing photon imrt with impt. *Technol. Cancer. Res. Treat.*, **2** p401, 2003.

Olofsson L., Mu X., Nill S., Oelfke U., Zackrisson B., and Karlsson M. Intensity modulated radiation therapy with electrons using algorithm based energy/range selection methods. *Radiother. Oncol.*, **73** p223, 2004.

Pimblott S.M. and La Verne J.A. On the radiation chemical kinetics of the precursor to the hydrated electron. *J. Phys. Chem. A*, **102** p2967–2975, 1998.

Pittman M., Ferré S., Rousseau J.-P., Notebaert L., Chambaret J. P., and Chériaux G. Design and characterization of a near-diffraction-limited femtosecond 100-tw 10-hz high-intensity laser system. *Appl. Phys. B*, **74** p529, 2002.

Pukhov A. Three-dimensionnal electromagnetic relativistic particle-in-cell code vlpl (virtual laser plasma lab). *J. Plasma Phys.*, **61** p425–433, 1999.

Pukhov A and Gordienko S. Bubble regime of wake field acceleration: similarity theory and optimal scalings. *Phil. Trans. R. Soc. A*, **364** p623–633, 2006.

Pukhov A. and VehnMeyer-ter J. Laser wake field acceleration: the highly non-linear broken-wave regime. *Appl. Phys. B*, **74** p355, 2002.

Pukhov A, Gordienko S, Kiselev S, and Kostyukov I. The bubble regime of laser-plasma acceleration: monoenergetic electrons and the scalability. *Plasma Phys. & Contr. Fus. B*, **46** p179–186, 2004.

Qiu P. and Bhandarkar S. An edge detection technique using local smoothing and statistical hypothesis testing. *Pattern Recognition Letters*, **17** p849–872, 1996.

Quesnel B. and Mora P. Theory and simulation of the interaction of ultra-intense laser pulse with electrons in vacuum. *Phys. Rev. E*, **58** p3718, 1998.

Radcliffe T., Barnea G., Wowk B., Rajapakshe R., and Shalev S. Monte carlo optimization of metal/phosphor screens at megavoltage energies. *Med. Phys.*, **20** p1161, 1993.

Raischel F. *A laser electron accelerator system for radiation therapy*. PhD thesis, University of Texas at Austin, 2001.

Rebibo S.. *Interférométrie à haute résolution temporelle d'un plasma créé par l'intraction d'une impulsion ultra brêve et intense (35fs,* 10^{17} *W/cm*^{2}*) avec une cible solide*. PhD thesis, Ecole Polytechnique, 2000.

Rosenzweig J.B. Trapping, thermal effects, and wave breaking in the nonlinear plasma wake-field accelerator. *Phys. Rev. A*, **38** p3634, 1988.

Rosenzweig J.B., Cook A.M., Scott A., Thompson M.C., and Yoder R.B. Effects of ion motion in intense beam-driven plasma wakefield accelerators. *Phys. Rev. Lett.*, **95** p195002, 2005.

Rousse A., Ta Phuoc K., Shah R., Pukhov A., Lefebvre E., Malka V., Kiselev S., Burgy F., Rousseau J.P., and ,D. ans HulinUmstadter D. Production of a kev x-ray beam from synchrotron radiation in relativistic laser-plasma interaction. *Phys. Rev. Lett.*, **93** p135005, 2004.

Schach von Wittenau A. E., Logan C. M., Aufderheide M. B., and Slone D. M. Blurring artifacts in megavoltage radiography with a flat-panel imaging system: comparison of monte carlo simulations with measurements. *Med. Phys.*, **29** p2559–2570, 2002.

Schroeder C.B., Esarey E., Tilborgvan J., and P. Leemans W. Theory of coherent transition radiation generated at a plasma-vacuum interface. *Phys. Rev. E,* **69** p016501, 2004.

Semushin S. and Malka V. High density gas jet nozzle design for laser target production. *Rev. Sci. Instr.*, **72** p2961–2965, 2001.

Sheng Z.M., Mima K., Zhang J., and VehnMeyer-ter J. Efficient acceleration of electrons with counterpropagating intense laser pulses in vacuum and underdense plasma. *Phys. Rev. E,* **69** p016407, 2004.

Shibata *et al.* Y. Observation of coherent transition radiation at millimeter and submillimeter wavelengths. *Phys. Rev. A*, **45**(12) pR8340–R8343, Jun 1992. doi: 10.1103/PhysRevA.45.R8340.

Shvets G. and Wurtele J. Instability of short-pulse lasers propagating through plasma channels. *Phys. Rev. Lett.*, **73** p3540, 1994.

Sprangle P., Tang C.H., and Esarey E. Relativistic self-focusing of short-pulse radiation beams in plasmas. *IEEE Trans. Plasma Sci.*, **PS-15** p145–153, 1987.

Sprangle P., Esarey E., and Ting A. Nonlinear theory of intense laser-plasma interaction. *Phys. Rev. Lett.*, **64** p2011, 1990.

Sprangle P., Esarey E., Krall J., and Joyce G. Propagation and guiding of intense laser pulses in plasmas. *Phys. Rev. Lett.*, **69** p2200, 1992.

Sprangle P., Krall J., and Esarey E. Hose-modulation instability of intense laser pulses in plasmas. *Phys. Rev. Lett.*, **73** p3544, 1994.

Strickland D. and Mourou G. Compression of amplified chirped optical pulses. *Opt. Comm.*, **56** p219–221, 1985.

Ta Phuoc K., Burgy F., Rousseau J.P., Malka V., Rousse A., Shah R., Umstadter D., Pukhov A., and Kiselev S. Laser based synchrotron radiation. *Phys. Plasmas,* **12** p023101, 2005.

Tajima T. and Dawson J. Laser electron accelerator. *Phys. Rev. Lett.*, **43** p267, 1979.

Tanaka K.A., Yabuuchi T., Sato T., Kodama R., Kitagawa Y., Takahashi T., Ikeda T., Honda Y., and Okuda S. Calibration of imaging plate for high energy electron spectrometer. *Rev. Sci. Instr.*, **76** p013507, 2005.

Ter-Mikaelian M.L. *High Energy Electromagnetic Processes in Condensed Mmedia.* Wiley-Interscience, New York, 1972.

Thomson Sir J.J. *Conduction of Electricity Through Gases*. Cambridge University Press, New York, 1928.

Ting A., Esarey E., and Sprangle P. Nonlinear wake-field generation and relativistic focusing of intense laser pulses in plasmas. *Phys. Fluids B*, **2** p1390, 1990.

Trebino R. *Frequency-Resolved Optical Gating: The Measurement of Ultrashort Laser Pulses.* Kluwer Academic Publishers, Boston, 2002.

Tremaine *et al.* A. Observation of self-amplified spontaneous-emission-induced electron-beam microbunching using coherent transition radiation. *Phys. Rev. Lett.*, **81** p5816–5819, 1998.

Tsung F.S., Narang R., Mori W.B., Joshi C., Fonseca R.A., and Silva L.O. Near-gev-energy laser-wakefield acceleration of self-injected electrons in a centimeter-scale plasma channel. *Phys. Rev. Lett.*, **93** p185002, 2004.

Umstadter D., Chen S.Y., Maksimchuk A., Mourou G., and Wagner R. Nonlinear optics in relativistic plasmas and laser wake field acceleration of electrons. *Science*, **273** p472–475, 1996.

Wartski L., Roland S., Lasalle J., Bolore M., and Filippi G. Interference phenomenon i optical transition radiation and its application to particle beam diagnostics and multiple scattering measurements. *J Appl. Phys.*, **46** p3644–3653, 1975.

Whittum D.H., Sessler A.M., and Dawson J.M. Ion-channel laser. *Phys. Rev. Lett.*, **64** p2511, 1990.

Whittum D.H., William M.S., Simon S.Y., Martin L., and Glenn J. Electron-hose instability in the ion-focused regime. *Phys. Rev. Lett.*, **67** p991–994, 1991.

Wilke I, MacLeod A.M., Gillespie W.A., Berden G, Knippels G.M.H, and MeerVan der A.F.G. Single-shot electron-beam bunch length measurements. *Phys. Rev. Lett.*, **88** p124801, 2002.

Wishart J.F. *Accelerators for ultrafast phenomena*, volume 87 of *Radiation Chemistry*. Elsevier, Amsterdam, 2001.

Yan X, MacLeod A.M., Gillespie W.A., Knippels G.M.H., Oepts D., MeerVan der A.F.G., and Seidel W. Subpicosecond electro-optic measurement of relativistic electron pulses. *Phys. Rev. Lett.*, **85** p3404–3407, 2000.

Yeboah C. and Sandison G. A. Optimized treatment planning for prostate cancer comparing impt, vheet and 15 mv imxt. *Phys. Med. Biol.*, **47** p2247, 2002.

Yeboah C., Sandison G. A., and Moskvin V. Optimization of intensity-modulated very high energy (50 - 250 mev) electron therapy. *Phys. Med. Biol.*, **47** p1285, 2002.